

Nh 97T 2830



KS002043061

R: FI

DE008860170

ELECTRON THERMAL TRANSPORT IN TOKAMAK PLASMAS

11/5-11-15214

ELEKTRON WARMTE TRANSPORT IN TOKAMAKPLASMA'S

met een samenvatting in het Nederlands

Proefschrift



DE008860170

TER VERKRIJGING VAN DE GRAAD VAN DOCTOR AAN DE UNI-
VERSITEIT UTRECHT OP GEZAG VAN DE RECTOR MAGNIFICUS,
PROF.DR. J.A. VAN GINKEL, INGEVOLGE HET BESLUIT VAN HET
COLLEGE VAN DEKANEN IN HET OPENBAAR TE VERDEDIGEN OP

WOENSDAG 30 NOVEMBER 1994
DES OCHTENDS TE 10.30 UUR

door

Johan Adriaan Konings

geboren op 7 oktober 1960 te Hilversum.

VOL 28 No 0

R

Promotoren: Prof. dr. F.C. Schüller Universiteit Utrecht
 Prof. dr. N.J. Lopes Cardozo Technische Universiteit Eindhoven
co-promotor: Dr. G.M.D. Hogeweij



CIP-DATA KONINKLIJKE BIBLIOTHEEK, DEN HAAG

Konings, Johan Adriaan

Electron thermal transport in tokamak plasmas / Johan Adriaan Konings
Proefschrift Universiteit Utrecht - Met samenvatting in het Nederlands.
ISBN 90-393-0675-3

Omslag: Parigi, Amsterdam.

The work described in this thesis was performed as part of a research programme of the 'Stichting voor Fundamenteel Onderzoek der Materie' (FOM) with financial support from the 'Nederlandse Organisatie voor Wetenschappelijk Onderzoek' (NWO) en EURATOM, and was carried out at the FOM-instituut voor plasmafysica in Nieuwegein, the Netherlands.

“ ... op de planeet Aarde had de mens altijd verondersteld dat hij intelligenter was dan de dolfijnen, omdat hij zoveel tot stand had gebracht – het wiel, New York, oorlogen en zo – terwijl dolfijnen alleen maar fijn dolden en nooit een spat uitvoerden. Maar omgekeerd waren de dolfijnen ervan overtuigd dat ze intelligenter waren dan de mens — om precies dezelfde redenen.”

“Het transgalactisch liftershandboek”
Douglas Adams.

Aan mijn ouders.

Contents

1	General Introduction	1
1.1	Nuclear Fusion	2
1.2	The Tokamak	3
1.3	This Thesis	6
1.4	Publications related to this thesis	8
2	Transport in Tokamak plasmas	11
2.1	Magnetic equilibrium	12
2.2	Collisional transport in toroidal geometry	13
2.3	Anomalous transport	15
2.4	Experimental transport studies	16
2.5	Transport codes	18
2.5.1	SNAP	18
2.5.2	Icarus	20
2.5.3	Toray	21
3	The Tools	23
3.1	The RTP tokamak	24
3.2	Diagnostics	25
4	Transport models	33
4.1	Introduction	34
4.1.1	Transport models and experimental observations	34
4.1.2	Z_{eff} as a guideline	37
4.1.3	Application to RTP	37
4.2	Electrostatic fluctuations	38

4.2.1	Trapped/Circulating, Collisional/Collisionless modes	38
4.2.2	Rogister and Hasselberg: Short wavelength modes	39
4.2.3	Drift waves including toroidal magnetic curvature	40
4.2.4	η_i -mode driven electron transport	40
4.2.5	Coupling of trapped ion to trapped electron modes	41
4.2.6	Weiland <i>et al.</i> : drift wave model	41
4.3	Magnetic fluctuations	42
4.3.1	Kadomtsev and Pogutse: Fluid approach	42
4.3.2	Ohkawa: Current filamentation	43
4.3.3	Rebut-Lallia-Watkins: Critical gradient	43
4.4	Electromagnetic fluctuations	44
4.4.1	Zhang and Mahajan	44
4.4.2	Guzdar <i>et al.</i> : High-frequency drift-like mode	45
4.5	Profile consistency	45
4.5.1	Coppi Mazzucato Gruber	45
4.5.2	Dnestrovskij	46
4.6	Summary	46
5	Ohmic target plasmas	51
5.1	Introduction	52
5.2	The RTP parameter regime	53
5.3	Experimental observations	53
5.4	Physical parameters	56
5.4.1	Current density profile and bootstrap current	56
5.4.2	Internal inductance	58
5.4.3	Collisionality	58
5.5	Transport	60
5.5.1	Energy confinement	60
5.5.2	Local thermal transport	61
5.5.3	Particle transport	63
5.6	Summary	65
5.7	Appendix A	66
6	Transport analysis in RTP	69
6.1	Introduction	70
6.2	Experimental	70
6.2.1	RTP	70

6.2.2	ECRH	70
6.2.3	Diagnostics	71
6.3	Local Power Balance analysis	71
6.4	Results	72
6.4.1	ECR deposition profile	72
6.4.2	T_e - and n_e -profiles	74
6.4.3	Global confinement	76
6.4.4	LPB analysis	78
6.5	Comparison with model predictions	80
6.5.1	Profile consistency	80
6.5.2	Rebut - Lallia - Watkins model	81
6.6	Discussion and Conclusions	83
7	Improved confinement during ECRH	87
7.1	Introduction	88
7.2	ECRH Power scan	88
7.3	ECRH Frequency scan	91
7.4	Discussion and Conclusion	93
8	The Z_{eff} scan	97
8.1	Introduction	98
8.2	Experimental observations	99
8.3	Transport analysis	106
8.3.1	Global confinement	106
8.3.2	Local transport	109
8.3.3	Scaling with collisionality	111
8.4	Comparison with transport models	112
8.4.1	Cross-correlation analysis	113
8.4.2	Correlation between Legendre coefficients	114
8.5	Discussion and Conclusion	115
8.6	Appendix A. Expansion in Legendre polynomials	117
8.7	Appendix B. Comparison with models: cross-correlation	119
8.8	Appendix C. Comparison with models: Legendre coefficients	120
9	Poloidal asymmetries	123
9.1	Introduction	124
9.2	ECRH Position scan	125

9.3 A model	130
9.4 Results and Discussion	134
10 Evaluation and Discussion	137
10.1 Summary of experimental findings	138
10.2 Impact of ECRH on transport	139
10.3 Plasma filamentation and the relation to this thesis	142
10.4 Recommendations for future research	145
Summary	147
Samenvatting	149
Dankwoord	151
Curriculum Vitae	152

Chapter 1

General Introduction

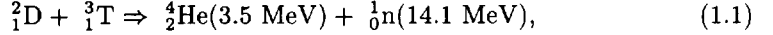
The daily life of a tokamak physicist working at the 'Rijnhuizen Tokamak Project' (RTP), is barely concerned with nuclear fusion, but directed towards the fundamental question why the energy losses in tokamak plasmas are so anomalously high. Anomalous transport, exceeding theoretical predictions by an order of magnitude, forces a commercial fusion reactor to be large and expensive. To reduce the size and costs, it is important to first understand and, subsequently, control anomalous transport. These studies can be well done in a device like RTP, even when no thermonuclear conditions are reached.

In this thesis, fundamental aspects of thermal transport in the RTP tokamak are discussed, and experiments are reported that provide better insight in the processes that enhance transport in tokamak plasmas.

1.1 Nuclear Fusion

Nuclear fusion research provides both interesting fundamental plasma physics as well as might provide the long term solution to the energy problem of the world. In the fusion process two light nuclei react to form a heavier one. In the reaction, mass is converted into energy, which can be calculated with Einstein's equation $E = mc^2$. Here c is the speed of light and m the mass deficit between the two light nuclei and the heavier nucleus.

There are many fusion reaction schemes in which energy is released. The one with the highest cross-section, and therefore most easily reached in experimental conditions, involves deuterium and tritium:



where helium and a neutron is formed. The kinetic energy of these particles can, in principle, be converted into electricity in a commercial fusion reactor.

Several conditions have to be fulfilled before fusion reactions can take place. Firstly, since the light nuclei are positively charged, they must have sufficiently high kinetic energy to overcome the repelling Coulomb force. This requires that the fuel (D and T) be heated to a temperature in excess of 10^8 K ($\simeq 10 \text{ keV}$). At this temperature the fuel is fully ionized and therefore in the plasma state. Secondly, to reach a 'burning' plasma places a condition on the triple product density (n_i) \times energy confinement (τ_E) \times ion temperature (T_i). The condition is that the energy produced by the fusion process ($P_{\text{fusion}} \sim n^2 T^2$) makes up for the energy loss ($P_{\text{loss}} \sim nT\tau_E^{-1}$), which leads to

$$n_i \cdot \tau_E \cdot T_i \geq 5 \times 10^{21} \text{ keV s m}^{-3} \quad (1.2)$$

with the density in units [m^{-3}], the temperature in [keV] and the energy confinement time in [s]. The latter one is the characteristic time with which the plasma would cool down by heat conduction, convection and radiation losses in the absence of any heating mechanism.

In present day devices the criterion (1.2) means that plasma pressures of several atmospheres at temperatures of hundreds of millions degrees Kelvin must be reached. Under these conditions, the plasma should not be in contact with any material object. To do so, the plasma can be confined in a tube closed on itself (a torus) by means of an externally imposed toroidal magnetic field. In the presence of such a

field, the charged particles are forced to move along field lines and, in principle, good confinement is obtained. The curvature of the field lines is, however, responsible for a drift of the particles, leading to a quick loss in confinement. This can be corrected by introducing an extra rotation in the magnetic field which cancels this drift on average. This rotation can be externally imposed (the stellarator concept), or obtained by inducing a current through the plasma that induces a magnetic field in the plane perpendicular to the torus, i.e. in poloidal direction. The latter concept is the tokamak configuration, which is currently believed to be the most promising candidate for a fusion reactor.

1.2 The Tokamak

The name *tokamak* is derived from the Russian words for 'toroidal magnetic chamber' (**T**oroidalnaya **K**amera **M**agnitnaya). A vacuum vessel in the shape of a torus is surrounded by a set of magnetic coils (see Fig. 1.1). These coils generate a magnetic field B_ϕ in toroidal direction, which, due to curvature of the field, has a $1/R$ dependence, with R the distance from the centre of the torus. A gas, which is injected into the vessel, is ionized, and a current is induced (I_P) in toroidal direction. Due to ohmic dissipation, the plasma temperature rises. The plasma current induces a poloidal magnetic field B_θ . The total field from both B_ϕ and B_θ has a helical field line structure, and in the ideal case forms an infinite set of nested, toroidal magnetic surfaces. On a magnetic surface, the field lines follow a helical path as they wind round the torus, with the normalized pitch given by

$$q = \frac{rB_\phi}{RB_\theta}, \quad (1.3)$$

where r is the distance to the plasma centre in the poloidal plane. When q reaches a rational value near the plasma edge, instabilities can occur that can lead to a sudden destruction of the plasma, called a disruption. For this reason q is called the 'safety factor'. The radial rate of change of q determines the shear of the magnetic field, which has important implications for the stability of the plasma.

The heating of ions to temperatures up to 10^7 K ($\simeq 1$ keV) can be achieved by ohmic dissipation resulting from I_P . Since at increasing electron temperature T_e , the electrical resistivity of the plasma decreases rapidly ($\sim T_e^{-3/2}$), ohmic dissipation diminishes. Therefore, additional heating methods are necessary to reach the required $T_i > 10^8$ K. This can be achieved by injecting high energy ($\simeq 100$ keV) neutral

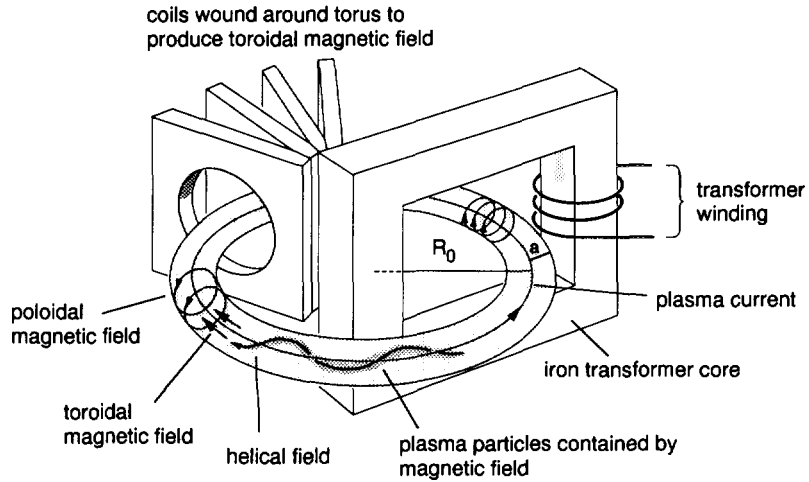


Figure 1.1: *Schematic presentation of the tokamak device. External coils generate a magnetic field in toroidal direction. The plasma acts as the secondary winding of a transformer, due to which a plasma current is induced. This current generates a poloidal magnetic field. As a result, a helical field line structure is obtained.*

hydrogen atoms into the plasma, which get trapped upon ionization and transfer their energy to the target plasma through collisions. Alternatively, RF waves can be launched in the plasma in such way that they are resonantly absorbed by the ions (Ion Cyclotron Resonance Heating, ICRH, with typical frequency tens of MHz) or electrons (Electron Resonance Cyclotron Heating, ECRH, typical frequency tens of GHz).

If Coulomb collisions were the only way plasma particles could interact, the transport of particles and energy could have been calculated on basis of collision induced diffusion. In a cylinder geometry, this is called classical transport, whereas in toroidal geometry it is called “neoclassical” transport. The basic picture is that ions and electrons, which gyrate around magnetic field lines, collide and exchange energy. Due to the mass difference between ions and electrons ($\sqrt{m_i/m_e} \simeq 40$), the energy transfer via the ion channel is expected to be the dominant one. Experimental

observations, however, show that the electron energy losses are anomalous, and exceed neoclassical predictions by one to two orders of magnitude, while the ion losses are somewhat larger than predicted, but not more than one order of magnitude. The anomalous heat loss means that the energy confinement time τ_E is much shorter than originally expected on the basis of neoclassical transport. It is further found that the energy confinement time increases with the particle density, n , the minor radius, a , and the major radius, R_0 , of the plasma. The consequence of anomalous heat losses is therefore that in order to meet the reactor criterium (1.2) one has to build much larger and therefore more expensive devices, as can be noted from the ITER parameters in Table 1.1. ITER is the first experiment meant to reach the reactor criterium fully. The large dimensions may put the economic feasibility of fusion power in jeopardy. For this reason it is of great importance to understand the mechanisms underlying anomalous heat losses.

Table 1.1: *Summary of parameters of larger tokamak devices. The current design values for the next-step device ITER (International Thermonuclear Experimental Reactor) are also indicated. For comparison, the Rijnhuizen Tokamak Project (RTP) is included.*

Device	R_0 [m]	a [m]	I_P [MA]	P_{inp} [MW]	$n \cdot \tau_E \cdot T_i$ [keV s m ⁻³]
JET	3.0	1.25	7.0	50	9×10^{20}
TFTR	2.4	0.8	2.2	30	4×10^{20}
JT-60U	3.4	1.0	6.0	30	6×10^{20}
DIID-D	1.67	0.67	3.5	20	4×10^{20}
ITER	7.75	2.8	25		$> 5 \times 10^{21}$
RTP	0.72	0.16	0.15	0.6	2.5×10^{17}

Anomalous transport, which is observed with the same characteristics in small and large devices, is believed to be caused by turbulence driven by small scale instabilities. The Rijnhuizen Tokamak Project (RTP) is dedicated to the study of anomalous electron thermal transport. Although the device is too small to achieve reactor conditions, the tokamak is useful to study anomalous transport since:

1. Enhanced transport is observed both in large and smaller machines and its

character is independent of the size of the device.

2. RTP is equipped with an extensive number of diagnostics that allow transport studies both with high spatial and temporal resolution.
3. RTP is useful for experiments that are difficult to perform in larger tokamaks, like controlled contamination, since a small machine can easily recover from that, while larger tokamaks would put their performance at risk.
4. The availability of Electron Resonance Cyclotron Heating (ECRH) at RTP allows direct local modification of $T_e(r)$ and the local electron energy balance.

RTP became operational in 1990 and soon after proved to be a serious partner in international fundamental transport research. Not because of its performance in fusion parameters but because of the effort made to measure as accurately as present technology permits.

1.3 This Thesis

In this thesis the process underlying enhanced transport is studied by means of dedicated experiments performed in the RTP tokamak. As a framework, the basic predictions given by neoclassical transport theory and the experimental observations in tokamak plasmas are discussed in Chapter 2 of this thesis. The experimental tools that are used in this study to quantify thermal transport are mentioned in Chapter 3.

In an ideal transport study experiment, one plasma parameter is varied and the effect on transport is measured. Usually this is a difficult task, since the external parameter that is varied as an external ‘knob’ can be coupled to other quantities which change simultaneously. The effective ion charge, Z_{eff} , is such a knob that can be varied by modifying the plasma constituents. In RTP it is possible, by carefully designing the experiments, to change Z_{eff} by almost an order of magnitude while the variation in other primary plasma parameters, such as density and temperature, is kept very small. In plasma physical terms this means that, since the effective electron-ion Coulomb collision cross-section is proportional to Z_{eff} , the collision frequency can be varied independently of other parameters that might influence the transport processes. At RTP, Z_{eff} is not directly measured as function of plasma radius, but obtained from the average plasma resistivity. The assumption is made that $Z_{\text{eff}}(r)$ is constant over the plasma cross-section. This assumption is empirically

justified in other devices by comparing the experimental electric resistivity, i.e. a quantity that is directly proportional to Z_{eff} , with theoretical predictions.

The collisionality is an important parameter in virtually any transport model. In classical transport, collisions are the basic process giving rise to diffusion. In turbulent transport, the collisionality plays an additional role because it can drive or damp the turbulence (especially important for electrostatic turbulence) and it determines the mean free path of particles that follow field lines (important for transport in a stochastic magnetic field). As a result, depending on the specific type of turbulence, transport models show a markedly different dependence on Z_{eff} . A survey of such models is presented in Chapter 4.

The experimental implementation of this research line was performed by deliberately contaminating plasmas in RTP, such that Z_{eff} was varied from 1.4 to 9.5. As obvious as this experimental approach may seem, in practice it needs considerable tuning to perform a single parameter scan with Z_{eff} . This may be the reason why it has not been attempted yet in the literature. The results of the Z_{eff} scan are reported in Chapter 8.

As another ‘knob’, the additional heating power is scanned by using ECRH (Chapter 6). Conditions are reported when ECRH leads to a reduction of transport in the so called ‘high electron temperature’ (HET) regime. This improvement of confinement is an intriguing effect. Detailed transport analysis showed that it is the result of a decrease of the transport coefficient throughout the plasma (Chapter 7). The question rises whether the improved confinement is a specific effect of ECRH, or that it is a mode of confinement that could also be reached by other means. In an attempt to gain insight into the mechanism of improved confinement, the ECRH power is modulated with a modulation frequency well in excess of the inverse confinement time, so that a quasi steady state is reached. This gives two additional degrees of freedom for the experiment: the duty cycle and the frequency of the modulation. Chapter 7 describes these experiments, in which it was possible to associate a characteristic time to the process that causes the reduction of transport.

Chapter 9 reports on experiments where the radial position of the ECR heating source to the plasma was varied. A remarkable observation was made: the apparent steady state temperature profiles showed an asymmetry in the midplane, with a different character for different ECRH resonance positions. A simple model was developed to explain the observation, based on transport of electrons along field lines, which are heated by the EC microwave radiation and are detected by the electron cyclotron radiation emission (ECE). The enhancement of $T_e(r)$ derived from ECE

depends on the pitch of the field lines, and on the relative toroidal angle between the launcher and the ECE antenna. Interestingly, the ECE diagnostic was positioned at another toroidal angle after the upgrade of RTP in 1993. New measurements again showed asymmetries, but the character was slightly different. Although the analysis is tentative, the model can explain the measurements done before and after the shut-down.

In the final, summarizing chapter the results of this thesis are evaluated.

1.4 Publications related to this thesis

SCHÜLLER F.C. *et al.*, among them KONINGS J.A., “Experimental observations of ohmic and ECR heated tokamak plasmas in RTP”, Proc. 18th Eur. Conf. on Contr. Fusion and Plasma Phys., Berlin (1991) Part I, 121.

SCHÜLLER F.C. *et al.*, among them KONINGS J.A., “Profile consistency as a result of coupling between the radial profile functions of pressure and current density”, Proc. 18th Eur. Conf. on Contr. Fusion and Plasma Phys., Berlin (1991) Part IV, 185.

KONINGS J.A., *et al.*, “Local power balance analysis in ohmic and ECR heated plasmas in RTP”, Proc. 19th Eur. Conf. on Contr. Fusion and Plasma Phys., Innsbruck (1992) Part I, 71.

LOPES CARDOZO N.J. *et al.*, among them KONINGS J.A., “Transport studies in the RTP tokamak”, Proc. 14th Int. Conf. on Plasma Phys. and Contr. Nucl. Fusion Res., Würzburg (1992) Vol.1, 271.

LOPES CARDOZO N.J., KONINGS J.A. and PETERS M., “Summary of the workshop on perturbative transport studies and relation to confinement”, *Nuclear Fusion* **32** (1992) 1671.

HOGWEIJ G.M.D., GORINI G., JACCHIA A., KONINGS J.A., LOPES CARDOZO N.J., DE LUCA F., MANTICA P., PETERS M. and the RTP team, “Perturbative transport studies in RTP”, APS (Division of Plasma Physics) Conference, Seattle, USA, 16-20 november 1992.

KONINGS J.A., SEGERS R.A., HOGWEIJ G.M.D., LOPES CARDOZO N.J. and the RTP team, “Local transport analysis in RTP: CW, modulated and off-axis ECRH”, Proceedings of Varenna Workshop on Local Transport studies in

Fusion Plasmas, 30 august - 3 september 1993. Vol.ISPP-14, Soc. Italiana di Fisica, Bologna (1993), p.45.

GORINI G., MANTICA P., HOGWEIJ G.M.D., DE LUCA F., JACCHIA A., KONINGS J.A., LOPES CARDOZO N.J. and PETERS M., "Simultaneous propagation of heat waves induced by sawteeth and electron cyclotron heating power modulation in the RTP tokamak", *Physical Review Letters* **71** 13 (1993) 2038.

GORINI G., DE LUCA F., HOGWEIJ G.M.D., JACCHIA A., KONINGS J.A., LOPES CARDOZO N.J., MANTICA P. and PETERS M., "ECH modulation experiments on RTP an overview.", Proceedings of Varenna Workshop on Local Transport studies in Fusion Plasmas, 30 august - 3 september 1993. Vol.ISPP-14, Soc. Italiana di Fisica, Bologna (1993), p.131.

KONINGS J.A., HOGWEIJ G.M.D., LOPES CARDOZO N.J., OOMENS A.A.M., SCHÜLLER F.C. and THE RTP TEAM, "Transport analysis in ohmic and ECR heated plasmas in the RTP tokamak", *Plasma Physics and Controlled Fusion* **36** (1994) 45.

HOGWEIJ G.M.D., DE LUCA F., GORINI G., JACCHIA A., KONINGS J.A., LOPES CARDOZO N.J., MANTICA P., PETERS M. and the RTP team, "Latest Results of Transport studies at the RTP tokamak.", Workshop on Transport in Fusion Plasmas, Aspenäs, Göteborg, june 1994.

MANTICA P., DE LUCA F., GORINI G., HOGWEIJ G.M.D., JACCHIA A., KONINGS J.A., LOPES CARDOZO N.J., PETERS M. and the RTP team, "Investigation of plasma current dependence of q -profile using on- and off-axis ECH modulation experiments on RTP.", Workshop on Transport in Fusion Plasmas, Aspenäs, Göteborg, june 1994.

HOGWEIJ G.M.D., KONINGS J.A., LOPES CARDOZO N.J., PETERS M., DE LUCA F., GORINI G., JACCHIA A., MANTICA P. and the RTP team, "Scaling of incremental heat diffusivity with T_e and ∇T_e ", 21th EPS Conf. on Contr. Fusion and Plasma Phys., Montpellier (1994).

PETERS M., H.J.HARTFUSS, DE LUCA F., ERCKMANN V., GIANNONE L., GORINI G., HOGWEIJ G.M.D., JACCHIA A., LOPES CARDOZO N.J., MAASSBERG H., MANTICA P., STROTH U. and KONINGS J.A., "A comparative heat wave study on RTP and W7-AS, ", 21th EPS Conf. on Contr. Fusion and Plasma Phys., Montpellier (1994).

DE LUCA F., GORINI G., HOGWEIJ G.M.D., JACCHIA A., KONINGS J.A., LOPES CARDOZO N.J., MANTICA P. and PETERS M., "Off-axis ECH modulation experiments on RTP, ", 21th EPS Conf. on Contr. Fusion and Plasma Phys., Montpellier (1994).

KONINGS J.A., HOGWEIJ G.M.D., LOPES CARDOZO N.J., OOMENS A.A.M. and the RTP team, "Transport analysis in helium-neon plasmas in RTP and comparison with transport models", 21th EPS Conf. on Contr. Fusion and Plasma Phys., Montpellier (1994).

OOMENS A.A.M. *et al.*, among them KONINGS J.A., "Plasma filamentation and first results of 110 GHz ECH in the RTP tokamak", 15th Int. Conf. on Plasma Phys. and Contrl. Nucl. Fusion Res., Sevilla, Spain, 26 September - 1 October 1994.

JACCHIA A., DE LUCA F., HOGWEIJ G.M.D., GORINI G., KONINGS J.A., LOPES CARDOZO N.J., MANTICA P. and PETERS M., "Transport analysis of ECH modulation and sawtooth activity in the plasma core of the RTP tokamak", accepted for publication in *Nuclear Fusion*.

Chapter 2

Transport in Tokamak plasmas

This chapter gives a more detailed introduction to transport in tokamak plasmas. The following topics are discussed: the magnetic equilibrium, collisional transport, anomalous transport and the way transport is measured. Since computer codes can be of help in the analysis, they are described at the end of this chapter.

2.1 Magnetic equilibrium

In a tokamak, the magnetic configuration is formed by an externally applied strong toroidal magnetic field, and a weaker poloidal magnetic field induced by the plasma current. The proper equations are provided by ideal magnetohydrodynamics (MHD), which treat the plasma as an ideally conducting fluid. The basic condition for equilibrium is that at all positions the magnetic force balances the force due to the plasma pressure gradient,

$$\mathbf{j} \times \mathbf{B} = \nabla p, \quad (2.1)$$

where \mathbf{j} is the local current density and p the pressure. Taking the innerproduct of eqn. (2.1) with \mathbf{B} gives $\mathbf{B} \cdot \nabla p = 0$, i.e. there is no pressure gradient along magnetic field lines and therefore on a magnetic flux surface the pressure has to be constant. Similarly, from eqn. (2.1) it follows that $\mathbf{j} \cdot \nabla p = 0$, consequently current flow lines also lie in the magnetic surfaces.

The local poloidal magnetic field is obtained by taking the toroidal component of Ampère's law

$$\mu_0 \mathbf{j} = \nabla \times \mathbf{B}, \quad (2.2)$$

which leads to the equation for B_θ in cylindrical geometry

$$\frac{1}{r} \frac{\partial}{\partial r} (r B_\theta) = \mu_0 j(r) \quad (2.3)$$

with $j(r)$ the toroidal current density averaged over the flux surface with radius r . Finally, the constraint

$$\nabla \cdot \mathbf{B} = 0 \quad (2.4)$$

implies that on a given magnetic surface field lines can not cross each other.

Due to the high thermal conductivity along the field lines, the temperature is equilibrated along a magnetic surface. Consequently, these surfaces are considered to be isothermal and isobaric surfaces.

The efficiency of confinement by the magnetic field with respect to the plasma pressure is often expressed as

$$\beta = \frac{\langle p \rangle}{B_0^2 / 2\mu_0}, \quad (2.5)$$

where $\langle p \rangle$ is the volume averaged pressure, $\int p dV / \int dV$, and B_0 the value of the toroidal magnetic field. The poloidal β is defined as

$$\beta_p = \frac{\langle p \rangle}{B_\theta(a)^2 / 2\mu_0}, \quad (2.6)$$

where $B_\theta(a)$ the poloidal field at the edge.

Note that the concept of nested flux surfaces is an ideal one. There are evidences that, due to instabilities, flux surfaces can break up and lead to a locally stochastic magnetic field.

2.2 Collisional transport in toroidal geometry

In a tokamak plasma there is an irreducible transport of particles and energy resulting from Coulomb collisions. The aim of transport analysis is to relate the fluxes (particle flux Γ , heat flux $q_{e,i}$, current density j) to the corresponding thermodynamic forces (∇n , $\nabla T_{e,i}$, E) [1]. In matrix notation,

$$\begin{pmatrix} \Gamma \\ q_e/n_e \\ q_i/n_i \\ j \end{pmatrix} = \begin{pmatrix} D & a_{12} & a_{13} & W \\ a_{21} & \chi_e & a_{23} & a_{24} \\ a_{31} & a_{32} & \chi_i & a_{34} \\ B & a_{42} & a_{43} & \sigma \end{pmatrix} \begin{pmatrix} \nabla n \\ \nabla T_e \\ \nabla T_i \\ E_t \end{pmatrix}, \quad (2.7)$$

where D is the particle diffusion coefficient, $\chi_{e,i}$ the thermal diffusivity and σ the electrical conductivity. With neoclassical theory not only the diagonal elements of the transport matrix (2.7) can be calculated, but also the off-diagonal elements. So becomes W the well known Ware-pinch coefficient which causes a particle flux driven by the toroidal electric field, and B gives the banana orbit induced bootstrap current. In this classical case, Onsager symmetry between off-diagonal matrix elements holds.

In an heuristic estimate, electron diffusion can be regarded as a random walk process of particles with a step length equal to the Larmor radius ρ_e , and a step time given by the collision time τ_e , to obtain the classical diffusion coefficient

$$D_c \sim \frac{\rho_e^2}{\tau_e}. \quad (2.8)$$

The particle diffusion coefficient D and the electron thermal diffusivity χ_e are of the same order. Collisional transport predicts that the ion heat diffusivity exceeds the electron one by $\chi_i = \sqrt{m_i/m_e} \chi_e$, since the ion step size is characterized by an orbit $(m_i/m_e)^{1/2}$ larger, and a step time $(m_i/m_e)^{1/2}$ longer.

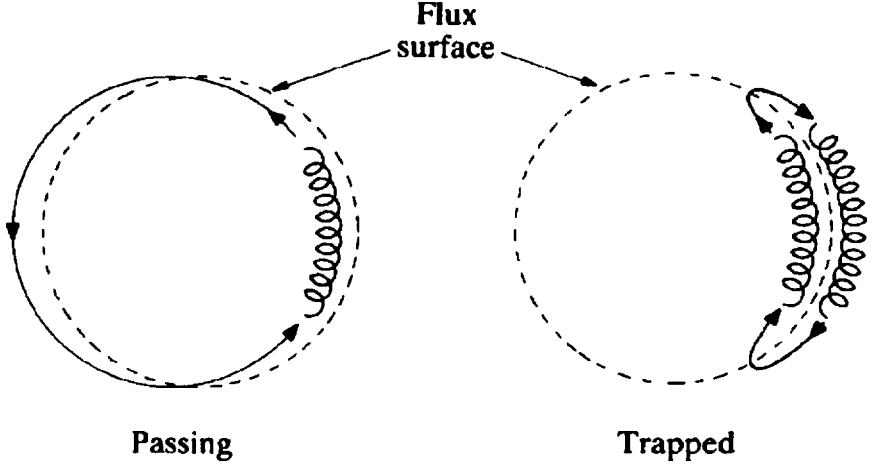


Figure 2.1: *The curvature of the magnetic field induces particle drifts and causes particles with a low collision frequency to become trapped in so called banana orbits. The figure shows the projection of a typical banana orbit on the poloidal plane.*

Collisional transport is substantially larger in a torus than in cylindrical geometry. The theory that takes this into account is called neoclassical. The curvature of the magnetic field induces particle drifts and causes particles with a low collision frequency to become trapped in so called banana orbits. Particles following a field line with sufficiently large perpendicular velocity compared to the parallel velocity are in fact bouncing between the points of high magnetic field, since the field strength is proportional to $1/R$. Figure 2.1 shows a typical banana orbit projected on the poloidal plane. Transport is enhanced because of an increased step length in equation (2.8), corresponding to the width of a banana orbit, being approximately the Larmor radius of the particle in the poloidal field only.

Three regimes can be identified depending on the electron collision time. In the *Pfirsch-Schlüter* regime a collision occurs before a particle traverses the distance along a field line from the inside to the outside of torus. In the *banana-regime* the collision frequency is so low that a trapped particle can complete at least one banana orbit within a collision time. The *plateau* regime is intermediate between the banana and Pfirsch-Schlüter. To first order in inverse aspect ratio $\epsilon = r/R$, the diffusion

coefficients in the banana and Pfirsch-Schlüter regime are

$$D_B = D_c q^2 \left(\frac{R}{r} \right)^{3/2} \quad \text{banana regime} \quad (2.9)$$

$$D_{PS} = D_c (1 + q^2) \quad \text{Pfirsch-Schlüter} \quad (2.10)$$

where D_c is given by equation (2.8) and q is the safety factor. The transition between the different regimes is given by the electron collisionality, which is defined as the ratio of the electron-ion collision frequency, ν_{ei} , and the banana bounce frequency¹, ν_{bounce} , given by:

$$\nu_e^* = \frac{1}{\epsilon} \frac{\nu_{ei}}{\nu_{bounce}} = \frac{\nu_{ei} q R_0}{\epsilon^{3/2} v_{th,e}}, \quad (2.11)$$

where q the local safety factor, R_0 the major radius, and $v_{th,e}$ the electron thermal velocity. At the transition banana-plateau, $\nu_e^* = 1$.

2.3 Anomalous transport

The predictions of neoclassical transport are not confirmed by experimental observations, at least in the direction perpendicular to the magnetic field. The electron energy losses are anomalous, and exceed neoclassical predictions by one to two orders of magnitude, while the ion losses are up to one order of magnitude larger than predicted. In contrast to this, transport along the magnetic field and the fourth row in the transport matrix (2.7) appear to be consistent with collisional theory.

It is believed that collisional transport is enhanced by electrostatic and/or magnetic fluctuations. Fluctuating electric fields, driven by a saturated level of turbulent microinstabilities, can cause particle drifts and convection of plasma across magnetic surfaces. Turbulent magnetic field fluctuations can destroy the magnetic topology and cause enhanced transport of particles moving along perturbed magnetic field lines. The question to be answered is what determines the fundamental stepsize and timestep replacing the collisional ones in eqn. (2.8). In case that anomalous transport is caused by electrostatic fluctuations, nearly all modes predict that the stepsize is still related to the ion Larmor radius, but that the timestep becomes the typical fluctuation time, i.e. microseconds. If the collision frequency becomes as high as the fluctuation frequency, the electrostatic turbulence will be damped. In

¹Or, equivalently, the ratio between one banana orbit length and the collision mean free path.

case of magnetic turbulence the stepsize becomes the typical radial random walk distance a stochastic magnetic field line will wander following it in toroidal direction during one collision mean free path. The timestep can either remain the collision time or the typical time during which the topology changes.

So far, however, there is no consistent picture to explain the enhancement of transport. Therefore, more theoretical and experimental efforts are needed to understand the anomaly.

2.4 Experimental transport studies

The most straightforward parameter to quantify tokamak plasma transport is the energy confinement time, which is defined as:

$$\tau_E = \frac{W_e + W_i}{P_{\text{inp}} - dW/dt} \quad (2.12)$$

where $W_{e,i}$ is the thermal energy and P_{inp} the total input power. Much attention has been given to the empirical scaling of τ_E as a function of parameters which determine a tokamak reactor, like I_P , B_ϕ , $\langle n \rangle$, R/a , ellipticity and additional power P_{add} . An example of the use of empirical scaling laws is the ITER-P89 scaling [2], which combines confinement data of different machines, as a prediction for the next step device.

Scaling laws can be used in a more profound manner by expressing τ_E in dimensionless, physical quantities like β , ν_e^* , q_a , s , magnetic Reynolds number, etc. Dimensionless scaling laws are useful for finding physics mechanisms, e.g. the question whether transport is dominated by microscopic or macroscopic instabilities², can be obtained from dimensionless scaling laws [3]. Nevertheless, global quantities like τ_E are built up from the summation of transport properties in different parts of the plasma column, where completely different transport mechanisms may rule with different scalings. Therefore, physics mechanisms may be difficult to derive from global quantities.

More refined transport studies aim at the estimation of the matrix elements in eqn. (2.7) as function of radius. There are two basic techniques: steady state analysis and perturbative transport studies. In steady state analysis, the balance between

²This corresponds to the fashionable dispute if tokamak scaling can be called "Bohm" (macroscopic turbulence) or "gyro-Bohm" (microturbulence).

sources and sinks is evaluated to estimate the fluxes. Unfortunately, this method is subject to large uncertainties, due to uncertainties in the local source and sink terms. In the dynamic analysis, the plasma response to a small perturbation is evaluated, which gives the incremental transport coefficients.

The basic continuity equation describing particle transport is given by:

$$\frac{\partial n_e}{\partial t} + \nabla \cdot \Gamma_e = S_{e,\text{source}} - S_{e,\text{sink}} \quad (2.13)$$

where Γ_e is the electron particle flux and S_e the particle source and sink term. The source of particles comes from ionization of neutrals, while the sink term represents recombination to neutral particles. Within a certain radius both sinks and sources are zero because the temperature is so high that ionization is complete. In such situation steady state implies $\Gamma_e = 0$. At RTP, $\partial n_e / \partial t$ is the only term in eqn. (2.13) that can be measured, therefore steady state particle transport is beyond the scope of this work.

The electron energy balance equation is given by

$$p_{e,\text{source}} - p_{e,\text{sink}} - \langle \nabla \cdot (q_{e,\text{cond}} + \frac{5}{2} \bar{\Gamma}_e T_e) \rangle + \frac{1}{n_e} \langle \Gamma_e \cdot \nabla (n_e T_e) \rangle = \frac{\partial}{\partial t} (\frac{3}{2} n_e T_e) \quad (2.14)$$

where, in steady state, the time derivative is set to zero. The brackets denote averaging over a flux surface. Relevant source terms on RTP are

$$p_{e,\text{source}} = p_{\text{ohmic}} + p_{\text{ECRH}}, \quad (2.15)$$

where p_{ohmic} the ohmic power density and p_{ECRH} the ECRH power deposition, in units $[\text{W}/\text{m}^3]$. To determine the shape of the p_{ECRH} profile and the amount of single pass absorbed power, ray-tracing calculations are done, using the code TORAY (see Section 2.5.3).

Losses are

$$p_{e,\text{sink}} = p_{ei} + p_{\text{rad}} \quad (2.16)$$

the electron-ion energy transfer p_{ei} and the radiation losses p_{rad} like line radiation and Bremsstrahlung. The radiation losses are estimated using the predictive transport code ICARUS (section 2.5.2). With these quantities all known, and $\Gamma_e = 0$, one can calculate q_e from eqn. (2.14). The electron heat diffusivity from power balance analysis is defined as

$$\chi_e^{\text{pb}}(r) = -\frac{q_e(r)}{n_e(r)\nabla T_e(r)}. \quad (2.17)$$

This quantity can be interpreted as a diffusion coefficient if the following conditions are met:

1. The generic transport model (2.7) holds, locally and everywhere.
2. The off-diagonal terms in the transport matrix are small.
3. The transport coefficients are smooth functions of radius and time. The typical stepsizes and timescales related to the transport mechanism must be much smaller than the experimental spatial dimensions and frequencies one is interested in.

These assumptions are normally made tacitly, also in this thesis. There are, however, indications that under certain conditions these assumptions are not valid. This will be discussed in more detail in Chapter 10. Note that $\chi_e^{\text{pb}}(r)$ can be subject to large uncertainties, since both q_e and $\nabla T_e(r)$ can have large error bars.

The plasma can also be described as a one-fluid medium, with one effective diffusion coefficient χ^{eff} , instead of χ_e and χ_i separately. This has the advantage that the electron-ion equilibration term in the power balance is ruled out. Care must be taken in such a treatment, e.g. it has been shown that the electron and ion species scale differently with the Larmor radius [4], which blurs the scaling of χ^{eff} when, depending on plasma conditions, one of the two species is dominant in χ^{eff} .

The transport analysis in this thesis is focussed on steady state transport. This means that for a plasma parameter A

$$\frac{\partial A}{\partial t} \ll \frac{A}{\tau_{\text{char}}} \quad (2.18)$$

where τ_{char} is the characteristic time over which the measurement is taken. In case of steady state transport analysis, the characteristic time is τ_E .

2.5 Transport codes

2.5.1 SNAP

From the measurements of the many RTP diagnostics, physical quantities like Z_{eff} , the current density and transport coefficients can be calculated. As a tool the time-

independent code SNAP is used. The code, which has been developed at Princeton [5], was modified for RTP.

Assuming toroidal symmetry and circular flux surfaces, local transport coefficients are calculated in steady-state plasmas. For this purpose, the input data of $T_e(R)$ and $n_e(R)$ is transformed to the flux-coordinate r . This can be done by a 'slice and stack' method, based on the hypothesis that for any slice of $T_e(r)$ and $n_e(r)$ equivalent values must lie on the same flux surface. As a consequence, hollow $T_e(r)$ and $n_e(r)$ are not allowed when the slice and stack method is used.

SNAP calculates a.o. the effective ion charge Z_{eff} assuming neo-classical resistivity, the ohmic power deposition $p_{\text{OH}}(r)$, the total thermal energy W , the energy confinement time τ_E , and the electron-ion energy exchange. Several models for ion transport are incorporated to calculate $T_i(r)$. Also, $T_i(r)$ can be parametrized.

The electron heat flux q_e is obtained from the power balance equation for electrons eqn. (2.14), and the electron heat diffusivity χ_e^{pb} from eqn. (2.17).

As an extension of the SNAP code, the error on $\chi_e^{\text{pb}}(r)$ is estimated using the error analysis method described by LOPES CARDOZO *et al.* [6] and HOGEWIJ *et al.* [7]. In this method, $T_e(r)$ and $q_e(r)$ are written as the sum of zero order profiles and first order perturbations. The perturbation profiles are expanded in Fourier series, of which higher frequencies are truncated, minimizing the sum of the truncation and the statistical error. The error in the heat conductivity is expressed analytically in terms of the errors on q_e and T_e . Typically, the error on χ_e^{pb} is 20 % at $r/a = 0.5$ in ohmically heated discharges. In extreme heating conditions during ECRH, with very steep $\nabla T_e(r)$ and a localized heat source, the expansion in zero order (Gaussian) profiles of $T_e(r)$ and $q_e(r)$ breaks down. In that case the error is estimated by adding noise to $T_e(r)$ and taking the response of $\chi_e^{\text{pb}}(r)$.

The plasma resistivity, $\eta(r)$, and Z_{eff} are calculated from the loop voltage and plasma current using Ohm's law, given $T_e(r)$ and $n_e(r)$. In the calculation of Z_{eff} , the Spitzer-Härm correction for non-hydrogenic plasmas [8] is included. Finally, given Z_{eff} , $\eta(r)$ and V_L , the current density profile is calculated.

Explicitly, the resistivity is calculated according to Spitzers formula derived from collisional theory

$$\eta_{\text{SP}} = 7.8 \times 10^{-8} \ln \Lambda Z_{\text{eff}} T_e(r)^{-3/2}, \quad (2.19)$$

where $\ln \Lambda$ is the Coulomb logarithm and T_e in [keV]. As noted before in section 2.3, transport coefficients parallel to the magnetic field appear to be predicted very well by collisional transport theory. Therefore one can use the neoclassical correction for

η due to the presence of trapped particles. This correction is calculated in SNAP according to

$$\eta_{\text{neo}}(r) = \eta_{\text{sp}}(r) * C_{nc} \quad (2.20)$$

where

$$C_{nc}^{-1} = (1 - \alpha) \left[1 - \alpha \left(0.56 \cdot \frac{3 - Z_{\text{eff}}}{(3 + Z_{\text{eff}}) Z_{\text{eff}}} \right) \right] \quad (2.21)$$

with

$$\alpha = \left[1 - \frac{(1 - \epsilon)^2}{\sqrt{1 - (\epsilon)^2} (1 + 1.46\sqrt{\epsilon})} \right] / [1 + (0.58 + 0.2 \cdot Z_{\text{eff}}) \cdot \beta] \quad (2.22)$$

and

$$\beta = \frac{6.92 \times 10^{-12} n_e(r) \ln \Lambda q_{\text{neo}}(r) R}{T_e(r)^2 (\epsilon)^{3/2}}. \quad (2.23)$$

where T_e in units [keV], ϵ is the inverse aspect ratio, a/R and $q_{\text{neo}}(r)$ is the q -profile that has been calculated from the current distribution. Note that β is proportional to the collisionality ν^* . In the calculation of q neoclassical resistivity has been assumed. This means that an iteration step is needed to calculate η_{neo} .

2.5.2 Icarus

The 1-D transport code ICARUS [9] calculates transport in a predictive manner by solving a set of coupled diffusion equations for particles and energy. The code has been used to estimate radiation losses and their radial distribution. For this purpose ohmically heated plasmas were studied with conditions similar to those observed experimentally in RTP.

Using ICARUS, transport can be evaluated given a number of models or by explicitly specifying χ_e as function of minor radius. The basic model employed is that given by neoclassical theory applicable to low and intermediate values of the collision frequency. Other models implemented are based on scalings from PLT and TFR.

The electron density is obtained from the solution of the particle transport equation, including sources coming from ionization of neutral particles, recombination and changes in the degree of ionization of impurity ions. An anomalous particle diffusion coefficient is used, as well as an inward pinch velocity which consists of the Ware-pinch component and a possible present anomalous pinch velocity.

The electron temperature profile is obtained from the solution of the energy balance equation, given an anomalous χ_e , the input power due to ohmic heating (Spitzer

resistivity is used, no neoclassical correction can be applied), electron-ion energy exchange and radiation³. The calculation of radiation losses includes Bremsstrahlung, electron cyclotron radiation and line radiation of impurity ions. The latter contribution, which is the dominant term for plasma conditions in RTP in the presence of impurities, is approximated by a coronal equilibrium model in which transport of ions in various ionization states is neglected. The dominant processes are excitation by collisions with electrons, and radiation by recombination. A fixed $Z_{\text{eff}}(r)$ can be specified.

Additional ECR heating can be applied using the (sub)program Toray. This ray-tracing code can be used either stand alone or as a part of ICARUS.

2.5.3 Toray

The code TORAY [10] allows the study of wave propagation during Electron Cyclotron Resonance Heating in toroidal geometry. Assuming a time independent plasma equilibrium, ray-tracing is performed and the ECR power absorption is calculated. Ray-trajectories are calculated in the cold-plasma approximation. For each integration step the new direction of the ray and the amount of absorbed power is calculated. The electron cyclotron damping routines applied use the weakly relativistic approximation of the dielectric tensor. This approximation is correct as long as the energy of the resonant electrons is below 50 keV.

The input of TORAY allows selection of parameters for the toroidal geometry (D-shaped, circular), various ECRH beams: O- or X-mode polarization, low field side (LFS) or high field side (HFS) launch, poloidal position, toroidal and poloidal angle of the beams and the power in each beam. For the calculation itself the knobs and switches comprise the resolution of the grid (poloidal and toroidal), the number of zones of the radial flux coordinate and the number of rays to be taken into account. When TORAY is used as a stand alone code, temperature and density profiles are parametrized⁴. As output the code gives the deflected rays, the absorbed ECR power

³In simulations for RTP's ohmic target plasmas the following scaling provided good approximations of the experimentally observed $T_e(r)$ and $n_e(r)$ ($q_a = 6.8$): $\chi_e(r) = 0.6 \times 10^{19} [T_e(r)^{1/2} / n_e(r)] e^{2((r/a)^2 - 1)} \text{ m}^2/\text{s}$, and for the particle diffusion $D = 0.25\chi_e$.

⁴The density profile can be modelled as:

$$n_e(\rho) = (n_{\text{max}} - n_{\text{min}}) (1 - (\rho)^{p_1})^{p_2} + n_{\text{min}} \quad (2.24)$$

where ρ is the normalized flux coordinate (in circular geometry $\rho = r/a$). The parameters p_1 and p_2 determine the shape of $n_e(r)$. For the temperature profile, the same expression is preprogrammed, also with free choice of parameters.

and $p_{\text{ECR}}(r)$.

Acknowledgements

The author is indebted to Dr. M.C. Zarnstorff (Princeton) for making the SNAP code available, and to Dr. E. Westerhof for the help and assistance for using the TORAY and ICARUS codes.

References

- [1] BALESCU R. (1988) Transport processes in plasmas, Elsevier Science Publishers B.V., The Netherlands Vol. 2.
- [2] YUSHMANOV P.N. *et al.* (1990) *Nucl. Fusion* **30**, 1999.
- [3] CHRISTIANSEN J.P. *et al.* (1993) *Nucl. Fusion* **33**, 863.
PERKINS F.W. *et al.* (1993) *Phys. Fluids B* **5**, 477.
- [4] LUCE T.C. *et al.* (1994) Workshop on Transport in Fusion Plasmas, Aspenäs, Göteborg.
- [5] TOWNER H.H. and GOLDSTON R.J. (1984) *Bull. Am. Phys. Soc.* **29**, 1305.
- [6] LOPES CARDOZO N.J., HOGWEIJ G.M.D. and HORDÓSY G. (1989) *Plasma Physics and Controlled Fusion* **31**, 471.
- [7] HOGWEIJ G.M.D., HORDÓSY G. and LOPES CARDOZO N.J. (1990) *Comput. Phys. Commun.* **59**, 245.
- [8] SPITZER L. and HÄRM R. (1953) *Phys. Rev. Letters* **89**, 977.
- [9] WATKINS M.L., HUGHES M.H., ROBERTS K.V., KEEPING P.M. and KILLEEN J. (1976) *Methods Comput. Phys.* **16**, 165.
- [10] KRITZ A.H. *et al.* (1982) Proc. 3rd Int. Symp. on Heating in Toroidal Plasmas, Grenoble (France), 22-26 March Vol. II p.707.
WESTERHOF E. (1989) Rijnhuizen Report 89-183, The Netherlands.

Chapter 3

The Tools

This chapter describes the experimental tools that were used in the transport analysis presented in this thesis. First the RTP tokamak and the ECRH system are described. Then the diagnostics relevant for this study are introduced.

3.1 The RTP tokamak

RTP: The RTP tokamak consists of a stainless steel vessel with a major radius of $R_0 = 0.72$ m and an inner minor radius of 0.235 m. Top and bottom carbon limiters can be placed at $z = \pm(0.16 - 0.185)$ m. The maximum toroidal field $B_T = 2.4$ T, plasma current $I_P \leq 150$ kA and the discharge duration ≤ 500 ms. Usually, hydrogen, deuterium, or helium are used as filling gas.

The plasma formation (breakdown) can be achieved by a short ECRH pulse for pre-ionization. Then, a changing magnetic flux of the transformer induces a toroidal electric field which accelerates the electrons. Collisions between charged and neutral particles lead to a chain reaction in which more neutrals are ionized. Eventually, a steady-state is reached in which the acceleration of charged particles due to the electric field is balanced by the friction between electrons and ions.

The total duration of the plasma discharge depends on the flux swing of the primary transformer, which is 1 Vs at RTP. If no ECRH is used for plasma start up, about 0.1 Vs is needed to reach sustained breakdown.

The ionization process is slowed down due to radiation losses, which are proportional to Z_{eff} . Thus a low Z_{eff} is advantageous for breakdown. To achieve a low Z_{eff} , several methods are commonly used: baking of the vessel and glow discharge cleaning are techniques to free absorbed gas from the vacuum vessel. Boronization provides a thin film on the vessel wall in such way that bonded atoms are never released again.

A large number of diagnostics is attached to RTP [1], most of them are described in Section 3.2. The control of plasma position, plasma current and plasma density will also be discussed in this section.

ECRH: At the start of operations in 1991 one gyrotron was available for Electron Cyclotron Resonance Heating from the low field side (Varian pulse-type gyrotron, 60 GHz, 100 ms). The TE_{11} O-mode (mode purity 90%) [2] is launched in the mid-plane, perpendicular to the toroidal field. The gyrotron can be operated at nominal power levels of 60 - 180 kW. The actual power which is deposited into the plasma is measured by a K-spectrometer measuring the microwave power in the transmission line. From time to time this measurement is calibrated against a caloric waterload. The position of the electron cyclotron resonance depends on where the critical magnetic field $B_T = 2.14$ T is located. Since the toroidal field falls with $1/R$, one can vary the position by varying B_T .

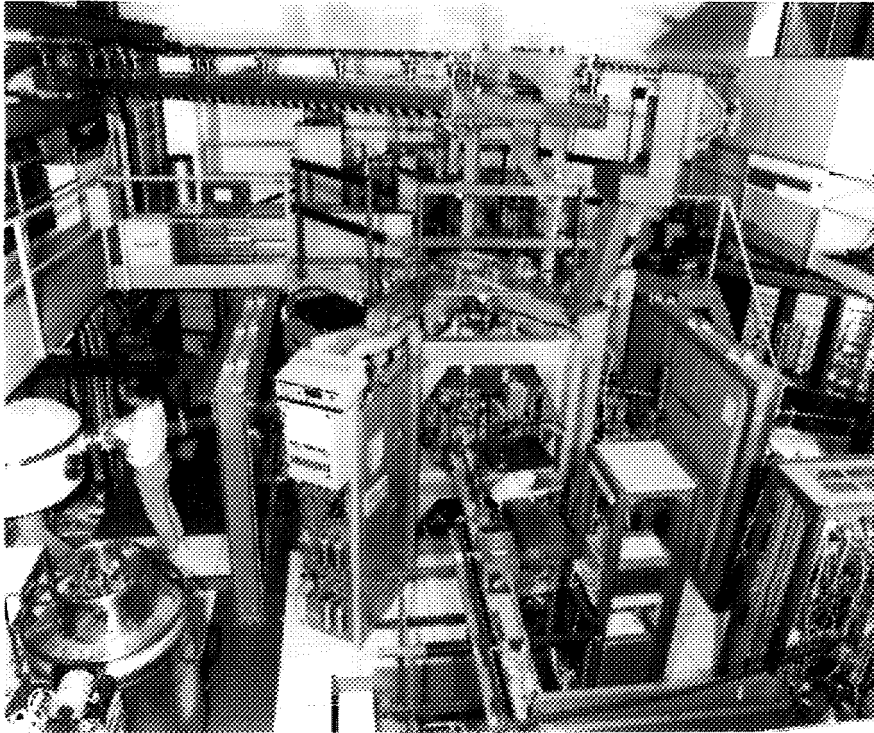


Figure 3.1: *The RTP tokamak.*

Later extensions to the gyrotron park became recently available and are not used for this thesis. They comprise a 60 GHz (200 kW) gyrotron applied from the high field side using a moveable mirror, and 110 GHz (500 kW) gyrotron at fixed position on the LFS.

3.2 Diagnostics

The RTP tokamak is equipped with a large number of instruments to diagnose the electron population. The diagnostics are based on (i) magnetic measurements, (ii) passive detection of radiation emitted by the plasma from the RF-frequency range to hard X-ray (a.o. heterodyne ECE, soft X-ray pulse height analysis, bolometry) and (iii) active probing (a.o. interferometry, Thomson scattering, pulsed radar). In

this section the interpretation and limitations of the diagnostics used in this study are discussed.

Magnetics: The standard set of magnetics on RTP consists of a number of small pick-up coils: a set of 12 for the poloidal and 12 for the radial field component, encased in a stainless steel tube, inside the vacuum vessel at $r = 0.213 \text{ m}$ ¹.

The plasma position is controlled and diagnosed by feedback on the poloidal dependence of the radial flux by means of a set of 12 saddle loops, located at the outer surface of the vessel (at $r = 0.24 \text{ m}$). The position can be controlled with a precision of 2-3 mm in steady state conditions. By this method the outermost flux surface of the plasma is kept at the same position (instead of centre of current density). The plasma current is kept close to its preprogrammed value by feedback on a Rogowski coil around the vessel, which measures the sum of the vessel current and plasma current.

The vertical magnetic field necessary to maintain the plasma in equilibrium, is given by:

$$B_v = -\frac{\mu_0 I_P}{4\pi R_0} \left(\ln \frac{8R_0}{a} + \beta_p + \frac{l_i}{2} - \frac{3}{2} \right) \quad (3.1)$$

where I_P is the plasma current, R_0 and a are the major and minor plasma radius, respectively, β_p is the poloidal beta and l_i the internal inductance. The value of the current generating the vertical magnetic field can be used to monitor changes in $\beta_p + l_i/2$. The absolute value of $\beta_p + l_i/2$ is not easy to evaluate, since part of the vertical field is provided by the current in the liner and by the current in the primary windings of the plasma current.

The power needed to generate the vertical, horizontal and poloidal fields is supplied by capacitor banks, switched on and off by a thyristor circuit (switching frequency $\simeq 1 \text{ kHz}$). The voltage spikes of the switching appear on the loop voltage and unfortunately also on some diagnostic signals. The loop voltage is measured by two flux loops, located in the midplane on the inner and outer circumference of the vessel. The raw signal shows a spiky behaviour, as shown in figure 3.2. A good smoothing of the measured loop voltage is obtained by an algorithm that detects each spike and computes the underlying surface (fat curve in fig. 3.2).

2 mm interferometer: The plasma density is controlled by a feedback system consisting of a single-chord 2-mm interferometer and a gasfeed system with

¹They can be used to reconstruct the magnetic equilibrium [3] and for the measurement of magnetic fluctuations (up to 10 kHz).

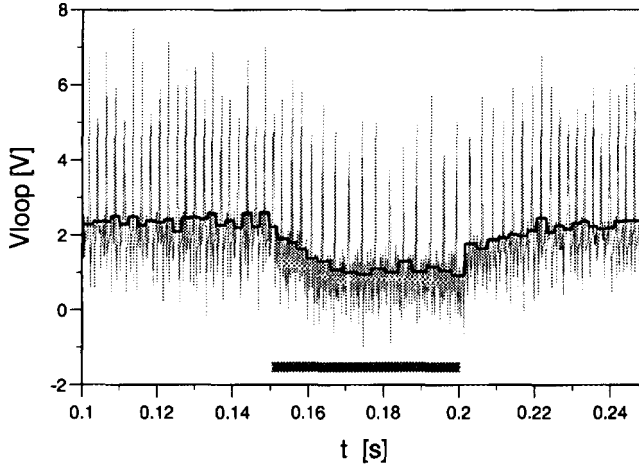


Figure 3.2: *The measured loop voltage (grey curve) and the signal obtained after the detection of each spike and computing the underlying surface. ECRH is applied from 0.15 – 0.2 s (shaded area).*

piezoelectric valves. Beside the feedback system, pre-programmed gaspuffing can be used.

19 channel Interferometer: A far-infrared slab beam ($\lambda = 432\mu\text{m}$) [4] is passed through the plasma and mixed with a local oscillator beam with a frequency difference of 1 MHz. A phase change is determined at 19 positions by comparison with the reference branch. The phase change is caused by the (anisotropic) refractive index of the plasma, which depends on the electron density. The line integrated density information can be converted to a radial $n_e(r)$ using Abel inversion techniques. In this study the method of YASUTOMO was used [5], which allows an in-out poloidal asymmetry but cannot reproduce hollow profiles very well. After Abel inversion, the error on n_e is typically 5%.

In the interpretation, no correction has yet been taken into account for refraction of the FIR-beam by the plasma causing slight deviations between the true and the apparent position of the detectors. The correction is however expected to be small at low to medium n_e , which is corroborated by the agreement in profile shapes between the interferometer and the multi-position Thomson scattering measurement.

Thomson scattering: The Thomson scattering system uses a Q-switched ruby

laser (initially 5 J, later extended to 25 J; $\lambda = 694.3$ nm) with a 15 ns pulse duration. The laser beam is passed vertically through the centre of the plasma. Detection of scattered light was initially done by a single point Thomson scattering set up in which the scattering volume could be scanned along the laser beam on a shot-to-shot basis. In later experiments, a multiposition diagnostic became available.

For the single-point radial Thomson scattering measurement [6], light from a 15 mm high volume (width $\phi \leq 2$ mm) is guided to a 20-channel polychromator, which covers the spectral range from 600 to 800 nm measuring both the blue and the red wing of the spectrum². Background light is measured just before and after the laser pulse. The accuracy in T_e is 2% at $n_e = 5 \times 10^{19} \text{ m}^{-3}$.

For the multiposition Thomson scattering measurement [7] radially scattered light from a 170 mm long chord along the laser beam (from $z = -55$ to $+115$ mm) is collected by means of a triplet lens and guided to a Littrow polychromator by means of several mirrors and two achromatic doublets. The spectrum is imaged on a 25 mm diameter microchannel plate based image intensifier, which is optically coupled to a CCD camera. The spatial resolution of the system depends on the number of pixels used for average, which determines the error on the estimated T_e and n_e . Typically, the spatial resolution is 1.7 mm. The accuracy, which depends on T_e and n_e , is typically 10% at 2 keV for $n_e(0) = 2 \times 10^{19} \text{ m}^{-3}$.

Heterodyne ECE: The frequency of Electron Cyclotron Emission (ECE) is linearly proportional to B , which in a tokamak has a $1/R$ -dependence. If the radiation intensity is proportional to T_e , this allows the measurement of $T_e(R)$. Figure 3.3 shows schematically the position of the ECE and the Thomson scattering diagnostic at RTP.

The ECE radiation is collected with a high-gain antenna and fed into a broadband mixer where it is down-converted in two steps to obtain a convenient frequency (0–1.5 GHz) [8]. In this way the frequency range from 86 to 146 GHz (2nd harmonic X-mode) is covered with a total of 20 channels with a frequency spacing of 3 GHz (spatial resolution $\simeq 1.5$ cm).

The deduction of T_e from the emitted radiation is not straightforward. The basic problem is that the plasma cannot be considered as a radiating black body, but has a finite optical thickness. For a non-optically thick plasma, the ECE radiation is given by:

²This allows detection of $0.2 \text{ keV} < T_e < 2 \text{ keV}$; for the high temperature range 2 - 10 keV two channels were added at 557 and 578 nm.

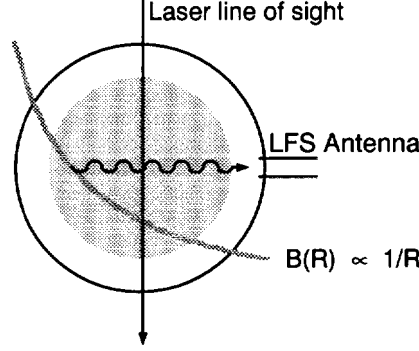


Figure 3.3: A scheme of the Thomson scattering and heterodyne ECE diagnostic at the RTP tokamak. Thomson scattering yields a vertical measurement of $T_e(r)$, while ECE views the plasma from the horizontal midplane on the low field side. Since for the emitted radiation $\omega \sim B \sim 1/R$, $T_e(R)$ is measured.

$$I_{\text{rad}}(\omega(R)) = \frac{eB_0}{m_e} \frac{R_0}{R} \frac{1 - e^{-\tau}}{1 - \alpha e^{-\tau}} \cdot c \cdot T_e(R) \quad (3.2)$$

where α is the reflection coefficient, c a fixed calibration coefficient and τ the optical thickness, which for 2nd harmonic X-mode is given by [9]

$$\tau_2^X = 6.526 \times 10^{-15} (R + r) \omega_{pe}^2 \frac{N}{4} T_e \left(\frac{6 - W^2}{3 - W^2} \right)^2 \quad (3.3)$$

with

$$N^2 = \left(\frac{1 - W^2}{4} \right) \left(\frac{4 - W^2}{3 - W^2} \right) \quad (3.4)$$

where $W = \omega_{pe}/\omega_{ce}$ with ω_{pe} the plasma frequency and ω_{ce} the first harmonic cyclotron frequency (see the Appendix in chapter 5 for the expressions). Note that for $n_e \leq 5 \times 10^{19} \text{ m}^{-3}$, $\tau_2^X \sim n_e T_e$.

For the reflection coefficient 0.0 and 0.8 was used, for measurements with and without an absorber mounted on the high field side, respectively. For the exact value of I_{rad} the nonlinearity of each detector is taken into account.

Soft X-ray diagnostic: an 80-channel, 5 camera soft X-ray tomography system [10] measures the SXR radiation (energy range 1 - 10 keV) in one poloidal plane. Using these cameras, a tomographic reconstruction can be done. For the present study,

only individual camera channels were used to obtain radial information. Each line of sight gives a line integrated measurement of the local emissivity. The continuum part of the spectrum gives rise to an intensity which is proportional to [10]:

$$g \simeq n_e^2 \int \frac{e^{-\epsilon/T_e}}{\sqrt{T_e}} D(\epsilon) \Gamma(T_e, Z_i, n_i, \epsilon) d\epsilon \quad (3.5)$$

where ϵ is the photon energy, $D(\epsilon)$ the detection efficiency and Γ the enhancement factor which is a complicated function of temperature and various ionization states of impurity species. On top of the continuum, there may be emission lines which can contribute significantly to the total SXR intensity. The strongest contribution to the line integrated measurement is expected from the region with highest density ($\sim n_e^2$, dominantly) and temperature ($T_e^{0.5}$ in clean discharges). Interpretation of the absolute value is, however, difficult.

Most suitable for this study were the top camera (camera 'C' at 90° with respect to the equatorial plane) and the side camera (camera 'A' at 10°). The effective chord width of each channel is 1 – 2 cm (excluding vignetting).

Neutral particle analyzer: The ion temperature was measured in RTP by means of passive neutral particle analysis. Hot neutrals from the (centre of) the plasma are stripped by a carbon foil and detected in an electrostatic analyser on eight channel electron multipliers.

Bolometer: The total radiation losses are measured by a radiative bolometer which consists of a $7 \mu\text{m}$ platinum absorbing foil that responds to the total radiative energy flux, particularly in the SXR and UV regions. The measuring surface is 1.8 cm^2 , which is 0.002% of the full toroidal surface.

Finally, the following diagnostics were indirectly of importance to this study: a SXR pulse height analyser, an ECE polychromator, and an ECR transmitted power diagnostic. The reader is referred to ref. [1] for more detailed information.

References

- [1] DONNÉ A.J.H. and the RTP team (1994) *Fizika Plazmy* **20**, 206.
- [2] POLMAN R.W., SMITS F.M.A., MANINTVELD P., OOMENS A.A.M., SCHÜLLER F.C. and VERHOEVEN A.G.A. (1989) Proc. 16th Eur. Conf. on Contr. Fusion and Plasma Phys., Venice.
- [3] VAN MILLIGEN B. (1991) Thesis Rijksuniversiteit Utrecht.
- [4] VAN LAMMEREN A.C.A.P., KIM K.S. and DONNÉ A.J.H. (1990) *Rev. Sci. Instrum.* **61**, 2882.
- [5] YASUTOMO Y. (1981) IEEE Trans. Plasma Sc. **ps-9**, 18.
- [6] BARTH C.J. (1988) *Appl. Opt.* **27**, 2981.
- [7] LOPES CARDOZO N.J., SCHÜLLER F.C., BARTH C.J., CHU C.C., PIJPER F.J., LOK J. and OOMENS A.A.M. (1994) *Phys. Rev. Lett.* **73**, 256.
- [8] VAN GELDER J.F.M., HUSMANN K.C.E., MIEDEMA H.S. and DONNÉ A.J.H. (1994) accepted for publication in *Rev. Sci. Instrum.*
- [9] BORNATICI M., CANO R., DE BARBIERI O. and ENGELMANN F. (1983) *Nucl. Fusion* **23**, 1153.
- [10] FERREIRA DA CRUZ D. (1993) Thesis Rijksuniversiteit Utrecht.

**NEXT PAGE(S)
left BLANK**

Chapter 4

Transport models

In this chapter various transport models are briefly discussed which give an expression for the electron thermal diffusivity. For the selection of models, the applicability to the parameter space of RTP (low β , $\nu^ \simeq 1$) is used as a criterium. The models included are based on electron drift wave turbulence, η_i -mode driven electron thermal transport, magnetic turbulence, electromagnetic turbulence and models based on 'profile resilience'. In experiments in RTP a scan of Z_{eff} was performed. Therefore, in this chapter the dependence on Z_{eff} is taken as a guideline.*

4.1 Introduction

Experimental observations in small and large tokamaks show that the electron thermal transport coefficient χ_e exceeds the value predicted by neoclassical theory by one to two orders of magnitude; ion thermal transport is enhanced by a factor 1-10 over neoclassical theory. It is currently believed that electrostatic and/or magnetic fluctuations are the driving mechanism of enhanced transport.

The observation of anomalous transport has given rise to a large number of transport models, based on various mechanisms. The experimental observations in many devices could be explained with varying success. So far, none of the models is consistent with the observed losses in the variety of all regimes *simultaneously*. These regimes include the hot plasma core and the plasma periphery, during linear ohmic confinement (LOC), saturated ohmic confinement (SOC), L-mode and H-mode under different additional heating conditions.

The field of viable models for anomalous transport could be reduced by comparison with an experimental dataset in which a single parameter is scanned. For this purpose, an experiment has been performed in RTP in which the effective ion charge Z_{eff} is scanned, while other conditions (like n_e , q_a etc.) are kept fixed as much as possible. This type of experiment can easily be done in small machines like RTP: machine contamination is often problematic in larger tokamaks. The experiment is relevant to larger devices, since anomalous transport is observed in both large and smaller devices, with the same empirical scaling.

In this chapter a selected number of transport models will be discussed which in later chapters will be compared to experimental observations in RTP. In particular, the role of Z_{eff} and the application to RTP's parameter space will be discussed.

4.1.1 Transport models and experimental observations

Electrostatic fluctuations can cause enhanced transport by $\tilde{\mathbf{E}} \times \mathbf{B}$ drifts. Transport models based on electrostatic driftwaves typically give $\chi_e \sim \gamma/k_{\perp}^2$, where k_{\perp} the poloidal wavenumber and γ the growth rate of the mode. The typical wavelengths are of the order of the ion Larmor radius ($k_{\perp}\rho_i \simeq 1$). The growth rate γ is somewhat lower than the typical fluctuation frequency and can be calculated once the turbulence spectrum is known [1]. In the calculation of the spectrum, both stabilizing and destabilizing terms must be taken into account to calculate the saturation level of the electrostatic instability (e.g. Landau resonance on the electrons, or a Landau damping on the ions [2]). Also, mode coupling can be included as well as a possible

energy cascade from long to short wavelengths.

Transport models have been tested against the experimental observations in many devices with varying success. We give a very brief review to sketch the situation. The dissipative trapped electron modes appear to provide a satisfactory description of the low density Ohmic regime where the energy confinement time τ_E scales favourably with n (linear ohmic confinement with Alcator scaling) [3], but fails to explain the saturation of τ_E at high density. The ion temperature gradient modes (η_i modes, with $\eta_i \equiv n \nabla T_i / (T_i \nabla n)$) have a threshold for instability [4], which could explain the saturation of τ_E at high values of n . When the plasma density is large enough so that the electron-ion thermal equilibration time ($\tau_{ei} \sim 1/n$) approaches the electron thermal energy confinement time (neo-Alcator $\tau_{E_e} \sim n$), significant energy losses can occur through the ion conduction channel. Although not treated here, the application of the ion temperature gradient mode model of ROMANELLI *et al.* [5] to the high density ohmic discharges of Alcator C and PDX shows that the saturation of τ_E at high n is predicted well.

A common failure of the trapped electron drift wave models and the ion temperature gradient mode is that χ_e has no I_P dependence, and generally shows a $1/B_0$ dependence. From experimental observations, a q_a dependence would be expected and no B_0 scaling. A second failure of both types of models is the prediction of small transport near the plasma edge, due to the unfavourable dependence on temperature, while experimentally transport coefficients increase towards the edge. Remedies against these failures have been (without theoretical justification): (i) a locally enhanced thermal diffusivity towards the edge, e.g. a "short circuit" at rational q surfaces to mimic low- m tearing modes [6, 7] and (ii) a built in q_a dependence in both trapped electron and η_i -mode [8, 9].

The driftwave model of WEILAND *et al.* [10] which is based on the toroidal η_i -mode and a coupling with the trapped electron mode, is of interest since it allows stationary inward flows of electron energy, as has been observed during off-axis ECR heating in DIII-D [11]. The peaked $T_e(r)$ found in these conditions has been successfully simulated with this drift wave model. Also, observations in TFTR have been successfully simulated by the model [12].

In the case of magnetic fluctuations, field lines make radial excursions, leading to enhanced radial transport. The radial motion of ions following a perturbed field line is much slower than the electron diffusion, because of the lower ion velocity. Am-

bipolar electric fields restrain electron particle diffusion and enhances ion particle diffusion such that no net radial current density occurs. However, thermal electron transport is not restricted by ambipolar diffusion and can exceed the particle transport by an order of magnitude.

The basic work on transport in a stochastic magnetic field is the one of RECHTER and ROSENBLUTH [13] who calculated the electron test particle diffusion coefficient resulting from radial excursions of stochastic magnetic field lines. Assumptions are that the magnetic field is externally imposed, is static and is fully stochastic, and that the decorrelation length of the field lines is much shorter than the mean free path length. However, the field line topology is not static, as seen from the broad band turbulent spectrum of experimentally measured magnetic fluctuations. The diffusion coefficient is an upper estimate of the thermal diffusion, since the condition that the field is fully stochastic is very difficult to meet [14]. In the intermediate case that the field is not fully stochastic with a finite number of intact flux surfaces, the problem of transport is yet unresolved [15].

Recently, experimental evidence for filamentation of the plasma has been observed in RTP [16]. Already in 1978, OHKAWA [17] developed a theoretical model based on filamentation of the plasma current on rational q -surfaces. Comparison with experimentally observed electron confinement times in various devices shows a surprisingly good agreement, which is especially remarkable since no numerical scaling was necessary.

The experimental observation of the ‘universal’ shape of the pressure profile $p_e(r, q_a)$ is called “profile consistency”. This is observed in ohmically heated plasmas, and during additional heating (neutral beams, ICRH). The dependence of the profile shape $T_e(r)/T_e(0)$ and $n_e(r)/n_e(0)$ to the edge safety factor q_a has led to possible q -dependent edge mechanisms [18]. Generally, models based on the principle of profile consistency show a good fit to experimental observations, e.g. the model of ZHANG and MAHAJAN applied to experimental observations in TFTR [19], and the model of COPPI, MAZZUCATO and GRUBER [20] to experimental data of Alcator C.

Note that for certain plasma conditions the models provide a good fit to experimental data. Application to other regimes (or devices) shows that yet no model is capable to fully explain anomalous transport. In the understanding, a single handle

that modifies transport is useful to accept or reject a model as a viable candidate to explain enhanced transport. That parameter could be Z_{eff} .

4.1.2 Z_{eff} as a guideline

The reason to choose Z_{eff} as scaling parameter is that Z_{eff} acts quite differently in the various transport models based on different mechanisms. In models based on electrostatic fluctuations, Z_{eff} appears through the collisionality. Also, the growth rate of both ion and electron drift wave instabilities can be strongly enhanced by the presence of impurity ions, as was shown by TANG [21] and DOMINGUEZ [22], assuming a simple model for the electron drift waves.

In models based on magnetic fluctuations, the role of Z_{eff} is not so clear. In the literature the emphasis lies with the calculation of the (perturbed) magnetic field configuration itself, without inclusion of collisional transport. It is known, however, that for particle transport, a mean $\mathbf{j} \times \mathbf{B}$ force contributes to the momentum balance in toroidal and poloidal direction, causing flows which could affect the ambipolar particle flux in the presence of magnetic fluctuations. Any non-ambipolarity in the anomalous transport affects the ambipolar electric field. Because of their high Z , neoclassical impurity transport can be most strongly affected. Experimental evidence of impurity pump-out by MHD activity strongly supports this mechanism [23].

4.1.3 Application to RTP

The selection of transport models was based on the parameter space of RTP. Only low β models were included (typically, $\beta_p = 0.1 - 0.3$ on RTP); no models based on (resistive) ballooning modes, and high pressure driven turbulence were therefore tested. The transport analysis on RTP concentrates on electron thermal transport. Therefore ion transport and particle transport is beyond the scope of this work, in as far as they do not have strong influence on electron thermal transport. The selection of models does not pretend to be complete. It is, however, attempted to cover a large area of different regimes relevant to the parameter space of RTP.

In the following sections, models are discussed based on electrostatic fluctuations (electron modes and electron transport driven by η_i -mode turbulence). Both the limit of long and short wavelength will be discussed, for which $k_{\perp} \rho_i$ fulfills $k_{\perp} \gg a^{-1}$. Then, models based on magnetic and electromagnetic turbulence are presented. Finally, models are given based on profile consistency. The main interest is the

application of the resulting expression for χ_e to the experimental data. Therefore, little attention is paid to the details of the often complex mechanisms that lay behind the derivation of the expression for χ_e .

The symbols used in this chapter are summarized in Table 4.2.

4.2 Electrostatic fluctuations

4.2.1 Trapped/Circulating, Collisional/Collisionless modes

Depending on the collision frequency, different type of electrostatic driftwave modes occur, as described by DOMINGUEZ and WALTZ [6, 24]. In the bulk plasma trapped electron modes are dominant, which can be dissipative ($\omega_e^* < \nu_{\text{eff}}$) or collisionless ($\omega_e^* > \nu_{\text{eff}}$) where ω_e^* is the diamagnetic frequency and $\nu_{\text{eff}} = \nu_e/\epsilon$ the effective electron collision frequency. Near the plasma edge, circulating electron modes occur, which can be collisional ($\nu_e > \omega_{te}$) or “universal” ($\nu_e < \omega_{te}$), where ω_{te} denotes the electron transit frequency.

The modes contributing to diffusion are expressed by :

$$\hat{\chi}_{te} = \epsilon^{1/2} \frac{\omega_e^*}{k_{\perp}^2} \cdot \left\{ 1, \frac{\omega_e^*}{\nu_{\text{eff}}} \right\}_{\min} \quad \text{trapped electron mode} \quad (4.1)$$

$$\hat{\chi}_{ce} = \frac{\omega_e^*}{k_{\perp}^2} \cdot \frac{\omega_e^*}{\omega_{te}} \cdot \left\{ 1, \frac{\nu_e}{\omega_{te}} \right\}_{\max} \quad \text{circulating electron mode} \quad (4.2)$$

where $\omega_{te} = v_{th,e}/(qR)$ and $\omega_e^* = k_{\perp}(T_e/eB)L_n^{-1}$. It is proposed by the authors to take $(k_{\perp}\rho_s) = 0.3$ with $\rho_s = c_s/\omega_{ci}$ the ratio of the sound speed to the ion cyclotron frequency, i.e. a value close to the ion Larmor radius.

As a connection for the different regimes a linear combination is proposed to obtain the total thermal diffusivity:

$$\chi_e = \alpha \cdot \frac{5}{2} (\hat{\chi}_{te} + \hat{\chi}_{ce}) \left(1 + c_{ei} f_{ith} \frac{L_n}{R} \frac{L_n}{L_T} \right) \quad (4.3)$$

where the collisional energy exchange from electrons to ions is neglected. The step-function f_{ith} represents the onset of the ion temperature gradient mode (η_i -mode). The constant $c_{ei} = 3$, and the coefficient α is used to fit experimental data (i.e. $\alpha = 1$ for DIII, Alcator and JET, and $\alpha = 0.3$ for ISX-A).

Table 4.1 explicitly shows the Z_{eff} dependence of the different modes, which is

hidden in the collision frequency.

4.2.2 Register and Hasselberg: Short wavelength modes

REGISTER and HASSELBERG *et al.* [25] consider the non-linear evolution of the dissipative trapped electron instability with nonlinear ion Landau damping ($k_{\perp} \rho_s \approx 0.6$). The following (numerically adjusted to TEXTOR data) expressions were obtained (units are [m²/s], [keV], [T], [m], [10¹⁹ m⁻³]):

$$\chi_e = 4.25 \times 10^3 \frac{\epsilon^{3/2} T_e^{7/2} (1 + 0.4 \eta_e^{-1})}{q R L_s B^2 n_e (1 + Z_{\text{eff}})} \times \mathcal{F}(\nu^*) [\gamma^* - 1]^{4.63} \quad (4.4)$$

where γ^* is the normalized growth rate, given by

$$\gamma^* = 23 \mu \frac{\epsilon^{3/2} T_e^2 L_s b_n(\sqrt{\nu^*})}{\sqrt{A_i L_n L_T n_e (1 + Z_{\text{eff}})}}. \quad (4.5)$$

The function $\mathcal{F}(\nu^*) = (b_p(\sqrt{\nu^*}) \bar{g}(x))$ depends on the collisionality factor¹:

$$\nu^* = 1.12 \times 10^{-3} q R n_e (1 + Z_{\text{eff}}) / \epsilon^{3/2} T_e^2. \quad (4.6)$$

The shear length $L_s = q R (d \ln q / d \ln r)^{-1}$ and μ is a parameter close to unity adjusted once and for all to a reference discharge. The expression for χ_e can only be applied to the ‘confinement region’ where the temperature and density gradients are largest. Note that χ_e is a strongly nonlinear function of T_e , n , L_n , L_T , L_s and Z_{eff} . As a consequence, small perturbations of the local parameters can lead to large changes in the transport.

¹The following functions have been used for abbreviation ($t = \sqrt{\nu^*}$):

$$\begin{aligned} x &= (|L_n| L_s / q^2 R^2) - 0.004 \\ b_n(t) &= (1 + t + t^2/2 + t^3/3) \exp(-t) \\ b_p(t) &= (1 + t + t^2/2 + t^3/6 + t^4/15) \exp(-t) \\ \bar{g}(x) &= [1 - \exp(-a_2 x)] (1 + a_3 x) / (1 + a_4 x + a_5 x^2) \end{aligned}$$

where $a_2 = 7.87$, $a_3 = 1.54$, $a_4 = 3.685$, $a_5 = 0.0707$.

4.2.3 Drift waves including toroidal magnetic curvature

The previously mentioned models treated drift waves in slab-like geometry, without toroidal magnetic drifts taken into account. SIMILON and DIAMOND [2] suggest that in toroidal geometry there exist two branches of the basic electron drift mode: the slab-like branch and the toroidicity-induced one which results from the inclusion of ion magnetic drifts. The following diffusion coefficients are obtained:

$$\chi_e = 0.2 \frac{v_*^2}{\omega_{te}} \frac{(2\epsilon)^{1/6}}{\hat{s}^{7/3}} \left(\frac{v_* \rho_s^{-1}}{\nu_{\text{eff}}} \right)^{1/3} \quad \text{for untrapped electrons (4.7)}$$

$$\chi_e = 0.2 \frac{v_*^2}{\omega_{te}} \frac{(2\epsilon)^{1/6}}{\hat{s}^{7/3}} \left(\frac{v_* \rho_s^{-1}}{\nu_{\text{eff}}} \right)^{1/3} (2\epsilon)^{1/2} \frac{\omega_{te}}{\nu_{\text{eff}}} \quad \text{trapped dissipative (4.8)}$$

($\nu_{\text{eff}} > 2\epsilon_n \omega_e^*$)

$$\chi_e = (2\epsilon)^{1/2} \frac{v_*^2}{\pi^2 \hat{s}^2 \omega_{de}} \quad \text{trapped collisionless (4.9)}$$

($\nu_{\text{eff}} < \omega_{de}$)

where $v_* = \omega_e^*/k_\theta = T_e/eBL_n$ and ω_{de} the electron magnetic drift frequency which scales as $\omega_{de} \sim \epsilon T_e^{1/2}/sa$ when $k_\perp \rho_i \sim 1$. Note that in the three regimes χ_e scales as $Z_{\text{eff}}^{-1/3}$, $Z_{\text{eff}}^{-4/3}$, and Z_{eff}^0 , respectively.

4.2.4 η_i -mode driven electron transport

Although η_i -mode turbulence drives primarily ion thermal transport, coupling with electron drift modes (e.g. dissipative trapped electron response) can lead to a driving mechanism for electron thermal transport as well. Using quasilinear theory, the following expression is obtained by WALTZ and LEE [1, 6]:

$$\chi_e = 3.2\sqrt{\epsilon} |C(\text{Re})|^4 (c_s^2 \rho_s^2 / \nu_e L_s^2) [(1 + \eta_i)/\tau]^3 (k_\perp \rho_s)^2, \quad (4.10)$$

where $C(\text{Re}) = (\pi/2) \ln(\text{Re})$ with $\text{Re} \simeq (1 + \eta_i)$ a ‘Reynolds number’ and $\tau = T_e/T_i$. For the spectrum averaged wavenumber, $k_\perp = 0.4 \rho_s^{-1}$ is obtained from the solution of the calculated spectrum. There is a Z_{eff} dependence via ν_e .

4.2.5 Coupling of trapped ion to trapped electron modes

Mode coupling between long-wavelength trapped-ion fluctuations to shear-damped moderate-wavelength trapped electron modes is treated by DIAMOND and BIGLARI [26]. In slab geometry, the nonlinear evolution of the trapped ion instability is described by a 2-D fluid equation. The transport level associated with the mode coupling is given by:

$$\chi_e = \frac{3}{8} \frac{\epsilon \rho_i^2 v_{Ti}^2}{\nu_{\text{eff},e} L_n^2 \hat{s}^2} \quad (4.11)$$

where \hat{s} is the magnetic shear. As with previous drift wave models, the Z_{eff} dependence is given by the collision frequency.

4.2.6 Weiland et al.: drift wave model

A model presented by WEILAND *et al.* [10] is based on the interaction of the η_i -mode enhanced by electron trapping, and a collisionless trapped electron mode. An inward directed electron heat flow can occur for $\eta_e \ll 1$, where the η_i -mode and trapped electron mode are individually stable, but a coupling between the two yields an instability.

In the model, the electron heat flux is given by

$$q_e = -f_t \left(n \frac{dT_e}{dr} - \frac{2}{3} T_e (1 + \Delta_e) \frac{dn}{dr} \right) \times \frac{\gamma^3 / k_\perp^2}{(\omega_r - [5/3] \omega_{De})^2 + \gamma^2}, \quad (4.12)$$

where $f_t = (2\epsilon/(1+\epsilon))^{1/2}$ is the fraction of trapped particles, ω_{De} is the magnetic drift frequency given by the sum of the field-curvature drift and ∇B drift frequencies. The frequency of the instability is $\omega = \omega_r + i\gamma$. The average wave vector k_\perp is taken to be the fastest growing mode, $(k_\perp \rho_i)^2 = 0.1$.

The term Δ_e is due to the trapped electron response:

$$\begin{aligned} \Delta_e = \frac{1}{N} \left\{ |\hat{\omega}|^2 \left[|\hat{\omega}|^2 (\epsilon_n - 1) + \hat{\omega}_r \epsilon_n \left(\frac{14}{3} - 2\eta_e - \frac{10}{3} \epsilon_n \right) + \right. \right. \\ \left. \left. \frac{5}{3} \epsilon_n^2 \left(-\frac{8}{3} + 3\eta_e + \frac{2}{3} \epsilon_n \right) \right] + \frac{50}{9} \hat{\omega}_r \epsilon_n^3 (\epsilon_n - 1) + \frac{25}{9} \epsilon_n^4 \left(\frac{7}{3} - \eta_e - \frac{5}{3} \epsilon_n \right) \right\} \end{aligned} \quad (4.13)$$

with

$$N = \left(\hat{\omega}_r^2 - \hat{\gamma}^2 - \frac{10}{3} \hat{\omega}_r \epsilon_n + \frac{5}{3} \epsilon_n^2 \right)^2 + 4 \hat{\gamma}^2 \left(\hat{\omega}_r - \frac{5}{3} \epsilon_n \right)^2, \quad (4.14)$$

where $\epsilon_n = 2L_n/L_B$ and $\hat{\omega} = \omega/\omega_e^*$ is the normalized eigenfrequency. The real part is given by

$$\hat{\omega}_r \simeq -\frac{5\epsilon_n}{3\tau} - \frac{\epsilon_n}{2(1-f_t)} - \frac{\epsilon_n(k_\perp \rho_s)^2}{2\tau(1-f_t)} \left(\frac{1}{2\epsilon_{T_i}} - \frac{5}{3} - \frac{\tau}{1-f_t} \right), \quad (4.15)$$

where $\tau = T_e/T_i$. The imaginary part is the growth rate, given by

$$\hat{\gamma} = \sqrt{\frac{1+f_t}{1-f_t} \left\{ \epsilon_n(1+\eta) - \frac{7}{4}\epsilon_n^2 \right\} - \frac{(1-\epsilon_n)^2}{4}}. \quad (4.16)$$

For comparison with experimental data, an *effective* diffusivity can be defined by:

$$\chi^{\text{eff}} = f_t \left(1 - \frac{2}{3} \frac{T_e}{n_e \nabla T_e} (1 + \Delta_e) \frac{dn}{dr} \right) \times \gamma' \quad (4.17)$$

where γ' is an abbreviation for the term which depends on the growth rate. Note that with this definition, in principle χ^{eff} could become negative, corresponding to a net electron heat flux up the temperature gradient.

4.3 Magnetic fluctuations

4.3.1 Kadomtsev and Pogutse: Fluid approach

A fluid approach is used by KADOMTSEV and POGUTSE [27] to calculate transport in a specified set of static magnetic field fluctuations. Their calculation holds for different regimes, including regimes of low and high fluctuation levels and regimes with low and high classical perpendicular transport ($\chi_\perp/\chi_\parallel$).

The following diffusion coefficients are obtained:

$$\begin{array}{llll} \chi \sim \sqrt{\chi_\parallel \chi_\perp} b_0^2 L_0 / \delta & \text{for} & b_0 L_0 / \delta \ll 1 & \text{and} & \sqrt{\chi_\parallel / \chi_\perp} \gg 1 \\ \chi \sim \chi_\parallel b_0^4 L_0^2 / \delta^2 & \text{for} & b_0 L_0 / \delta \ll 1 & \text{and} & \sqrt{\chi_\parallel / \chi_\perp} \gg \delta / b_0^2 L_0 \\ \chi \sim \chi_\parallel b_0 \delta / L_0 & \text{for} & b_0 L_0 / \delta > 1 & \text{and} & \sqrt{\chi_\parallel / \chi_\perp} > L_0 / \delta \\ \chi \sim \sqrt{\chi_\parallel \chi_\perp} b_0 & \text{for} & b_0 L_0 / \delta \gg 1 & \text{and} & b_0 \sqrt{\chi_\parallel / \chi_\perp} \gg 1 \end{array}$$

where $b \sim \tilde{B}/B_0$ ($b_0^2 = \langle b^2 \rangle$) the magnitude of magnetic fluctuations, δ is the transverse correlation length of the magnetic field and L_0 the correlation length along the field. The classical diffusion coefficients are given by $\chi_{\parallel} = \lambda^2/\tau_c$ and $\chi_{\perp} = \rho^2/\tau_c$ with τ_c the collision time. In the limit $b_0 L_0/\delta \sim 1$, $L_0 = qR$ and $\delta = c/\omega_{pe}$ with ω_{pe} the plasma frequency, the expression in the plateau and banana regime becomes:

$$\chi_e = v_{th,e} \delta^2 / qR. \quad (4.18)$$

Note that in this limit χ_e becomes independent of the collision time (thus independent of Z_{eff}), but it is the correlation length that determines the thermal diffusivity.

4.3.2 Ohkawa: Current filamentation

The theoretical model of OHKAWA [17] is based on small-scale filamentation of the plasma current on rational q -surfaces. The transport rate is associated with the time scale for electron heat flow along the field lines and the typical skin time of the magnetic perturbations. No adjustable numerical coefficients are needed, and the following expression is obtained:

$$\chi_e = \frac{c^2}{\pi \omega_{pe}^2} \sqrt{(v_{th,e}/Rq)^2 + \nu_e^2} = \frac{c^2 \nu_e}{\pi \omega_{pe}^2} \sqrt{1 + (\nu_e^*)^{-2} \epsilon^{-3}}. \quad (4.19)$$

The expression is valid assuming that the collision frequency is not too large compared to the transit frequency. In the higher collisional regime collisions will damp the perturbation and it may take a stronger magnetic turbulence level to drive the mode. Note that for low collisionality the dependence on ν_e is negligible and that there is, then, no Z_{eff} dependence.

4.3.3 Rebut-Lallia-Watkins: Critical gradient

REBUT, LALLIA and WATKINS [28] developed a semi-empirical model based on stochastisation of the magnetic field, in which magnetic islands are embedded in a chaotic sea. A mechanism based on a critical electron temperature gradient is used to explain the onset of the magnetic fluctuations.

The effective electron thermal diffusivity is given by:

$$\chi_{e,RL}^{\text{eff}} = \chi_{e,neo} + \chi_{e,RL}^{\text{inc}} \left(1 - \frac{(\nabla T_e)_c}{\nabla T_e} \right) H[\nabla T_e - (\nabla T_e)_c] H[\nabla q], \quad (4.20)$$

where $\chi_{e,neo}$ is the neoclassical thermal diffusivity, and the incremental diffusivity is given by:

$$\chi_{e,RL}^{\text{inc}} = \alpha \left[\frac{\nabla T_e}{T_e} + \frac{2\nabla n_e}{n_e} \right] \sqrt{\frac{T_e}{T_i}} \left(1 - \sqrt{\frac{r}{R}} \right) \sqrt{1 + Z_{\text{eff}}} \left(\frac{q^2}{\nabla q B_T R^{1/2}} \right). \quad (4.21)$$

In this equation q is the safety factor, r and R are the major and minor radius, respectively, and H is the Heaviside step function. The critical temperature gradient is given by:

$$k_b(\nabla T_e)_c = \frac{\beta}{q} \left(\frac{\eta j B_T^3}{n_e (k_b T_e)^{1/2}} \right)^{1/2}, \quad (4.22)$$

where k_b is Boltzmann's constant, η is the plasma resistivity, j the current density, B_T the toroidal magnetic field and q is the local safety factor. The parameters α and β have been tuned to fit the confinement database of JET ($\alpha = 2$ and $\beta = 6$). The Z_{eff} scaling is included on semi-empirical basis.

4.4 Electromagnetic fluctuations

4.4.1 Zhang and Mahajan

A transport model based on electromagnetic turbulence is presented by ZHANG and MAHAJAN [29]. Given the existence of an electromagnetic mode, of which no origin is specified, an energy diffusion coefficient is obtained by solving the equation for turbulent transport of energy. The result is:

$$\chi_e = \gamma \frac{c^2}{\omega_{pe}^2} \frac{1}{eB} |\nabla T_e| \left\{ 1 + \frac{\alpha}{\eta_e} \right\} \quad (4.23)$$

where α is of order unity and γ is a constant which might be determined by nonlinear theory, or fixed by comparison with experiments. The expected fluctuation level is $\tilde{B}/B_0 = \gamma \frac{\rho_e}{L_T} (1 + \frac{\alpha}{\eta_e})$.

4.4.2 Guzdar et al.: High-frequency drift-like mode

GUZDAR et al. [30] present a model in which high frequency drift waves are driven by the electron temperature gradients which could be driven by magnetic fluctuations. The wavelength of the modes is between the electron and ion gyroradius, driven unstable by the electron temperature gradient. In the low collisional regime, and for $1 < \eta_e < 6$, the following expression is obtained:

$$\chi_e = 0.1 \left(\frac{c}{\omega_{pe}} \right)^2 \frac{v_{th,e}}{qR_0} (1 + \eta_e) \eta_e \hat{s} \quad (4.24)$$

$$= 5 \times 10^{19} \frac{T_e^{1/2}}{n_e R_0 q} (1 + \eta_e) \eta_e \hat{s} \quad (4.25)$$

where $v_{th,e}$ is the electron thermal velocity and ω_{pe} the plasma frequency and \hat{s} the magnetic shear.

4.5 Profile consistency

It is an experimental observation that the relative pressure profile $p_e(r)/p_e(0)$ in tokamak plasmas is related to the shape of the toroidal current density profile $j(r)/j(0)$. Theoretically such a coupling was discussed by BISKAMP [31] and MONTGOMERY *et al.* [32]. KADOMTSEV [33] came to an explanation based on the principle of minimal free energy of the magnetohydrodynamic configuration under virtual displacements of the magnetic flux. TAYLOR [34] came to the same expression based on the hypothesis that the current is filamented. If tokamak transport is considered as a phenomenon of self-organization, nonlinear relations between fluxes and gradients may provide a ‘profile resilience’ [35].

Coupling between $p(r)$ and $j(r)$ is important since it allows the electron heat flux obtained from experiment to be separated in a diffusive and convective component. The following models are derived from a more experimental point of view.

4.5.1 Coppi Mazzucato Gruber

COPPI and MAZZUCATO [36, 37] have, except for one scaling parameter, explicitly solved the coupled set of equations relating $T_e(r)$ to $j(r)$ in ohmically heated plasmas. The following expression is obtained:

$$\chi_e = 3.64 \times 10^{14} \left(\frac{B_T}{q T_e} \right) [\ln \Lambda Z_{\text{eff}}/n_e^2]^{2/5}, \quad (4.26)$$

in units $[\text{m}^2/\text{s}]$, $[\text{T}]$, $[\text{keV}]$ and $[\text{m}^{-3}]$.

4.5.2 Dnestrovskij

DNESTROVSKIJ *et al.* [38] developed a transport model based on the deviation of $T_i(r)$ and $T_e(r)$ from canonical, ‘profile consistent’ profiles. The expressions for electron and ion heat flux are obtained without leaving free parameters by comparison of the calculation with experiment. This leads to:

$$\chi_e = 160 \epsilon^{1.75} \sqrt{T_e}/(qR). \quad (4.27)$$

The numerical constant has been adjusted to T-11 data.

4.6 Summary

Electrostatic and/or magnetic fluctuations are generally believed to be the driving mechanism of anomalous transport. Models based on electrostatic turbulence are applicable to different regimes that are connected smoothly: the collisional, collisionless, circulating and trapped electron regime. They can be superimposed simply as a linear combination. The models involve short wavelength turbulence (ROGISTER and HASSELBERG), long wavelength (WEILAND) and intermediate (DOMINGUEZ and WALTZ). Ion drift waves can drive electron transport (WALTZ and LEE; DIAMOND and BIGLARI).

The fundamentals for models based on magnetic fluctuations were laid down by RECHESTER and ROSENBLUTH in 1978 in their test-particle approach of a fully ergodic magnetic field. More regimes were treated, e.g. KADOMTSEV and POGUTSE in a fluid approach. Numerical simulations, including self-consistent solutions of the magnetic field topology are currently being undertaken. The model of OHKAWA, which has its origin in filamentation of the plasma current, gives a good prediction of the experimentally obtained energy confinement time.

The observation of ‘profile resilience’ both in ohmic and (ICRH, NBI) heated plasmas gave rise to models based on experimental observations (COPPI, MAZZUCATO, GRUBER) and DNESTROVSKIJ.

Table 4.1 gives a summary of the explicit Z_{eff} dependence of the transport models

treated in this chapter. The majority of the models that were discussed have a Z_{eff} dependence through the collision frequency. Z_{eff} occurs more explicitly in the models based on experimental observations. Note that the electrostatic models have no, or a negative Z_{eff} dependence, while models based on magnetic turbulence show a positive dependence. Given the large differences in scaling of χ_e with Z_{eff} , it seems appropriate to compare the predictions of the models with an experimental dataset in which Z_{eff} is scanned. This is done in Chapter 8 of this thesis.

Table 4.1: *The explicit dependence of χ_e of the transport models discussed in this chapter on Z_{eff} . The symbol '-' means that Z_{eff} is not included in the derivation of the model.*

	<i>Author(s)</i>	<i>Model</i>	Z_{eff}
(4.2.1)	WALTZ, DOMINGUEZ	Dissipative trapped	Z_{eff}^{-1}
		Collisionless circulating	Z_{eff}^0
(4.2.2)	ROGISTER, HASSELBERG	Short wavelength	see eqn.(4.4)
(4.2.3)	SIMILON, DIAMOND	Circulating; Toroidal curvature	$Z_{\text{eff}}^{-1/3}$
		Trapped dissipative	$Z_{\text{eff}}^{-4/3}$
		Trapped collisionless	Z_{eff}^0
(4.2.4)	WALTZ, LEE	η_i -mode driven	Z_{eff}^{-1}
(4.2.5)	DIAMOND, BIGLARI	Trapped ion driven	Z_{eff}^{-1}
(4.2.6)	WEILAND	η_i and trapped electron	-
(4.3.1)	KADOMTSEV, POGUTSE	Magnetic turbulence	-
(4.3.2)	OHKAWA	Current filamentation	$\approx Z_{\text{eff}}^0$
(4.3.3)	REBUT, LALLIA, WATKINS	Critical gradient	$(1 + Z_{\text{eff}})^{1/2}$
(4.4.1)	ZHANG, MAHAJAN	Electromagnetic turbulence	-
(4.4.2)	GUZDAR	High frequency electromagnetic	-
(4.5.1)	COPPI, MAZZUCATO	Profile consistency	$Z_{\text{eff}}^{2/5}$
(4.5.2)	DNESTROVSKIJ	Canonical profiles	-

Table 4.2: *Summary of symbols used in this chapter.*

<i>Quantity</i>	<i>Symbol</i>	<i>Expression</i>
Inverse aspect ratio	ϵ	r/R_0
Safety factor	q	
Scale length	L_α	$\alpha/\nabla\alpha$ with $\alpha = n_e, n_i, T_e, T_i$
	$\eta_{i,e}$	$L_n/L_{T_{i,e}}$
Shear	\hat{s}	$(r/q)dq/dr$
Shear length	L_s	R_0q/\hat{s}
	ϵ_n	$2L_n/L_B$
	τ	T_e/T_i
Electron thermal velocity	$v_{th,e}$	$(2kT_e/m_e)^{1/2}$
Ion thermal velocity	$v_{th,i}$	$(2kT_i/m_i)^{1/2}$
Ion-acoustic velocity	c_s	$(2kT_e/m_i)^{1/2}$
Electron cyclotron freq.	ω_{ce}	$[eB_\phi]/[m_e]$
Ion cyclotron freq.	ω_{ci}	$[eB_\phi]/[m_i]$
Electron plasma freq.	ω_{pe}	$([n_e e^2]/[m_e \epsilon_0])^{1/2}$
Ion plasma freq.	ω_{pi}	$([n_i Z^2 e^2]/[m_i \epsilon_0])^{1/2}$
Trapped bounce freq.	ω_{be}	$\epsilon^{1/2} v_{th,e}/(qR_0)$
Transit freq.	ω_{te}	$v_{th,e}/(qR_0)$
Electron gyroradius	ρ_e	$v_{th,e}/\omega_{ce}$
Ion gyroradius	ρ_i	$v_{th,i}/\omega_{ci}$
	ρ_s	c_s/ω_{ci}
Wavenumber	k_\perp	
Diamagnetic frequency	ω_e^*	$k_\perp \rho_s c_s / L_n$
Electron collision freq.	ν_e, ν_{ei}	
Effective electron freq.	ν_{eff}	ν_{ei}/ϵ
Electron collisionality	ν_e^*	$\nu_{ei}/\epsilon \omega_{be}$

References

- [1] LEE G.S. and DIAMOND P.H. (1986) *Phys. Fluids* **29**, 3291.
- [2] SIMILON P.L. and DIAMOND P.H. (1984) *Phys. Fluids* **27**, 916.
- [3] SCHRAM D.C. and SCHÜLLER F.C. (1980) *Physica* **100C**, 371.
- [4] GARBET X. *et al.* (1992) *Phys. Fluids* **B4**, 136.
- [5] ROMANELLI F., TANG W.M. and WHITE R.B. (1986) *Nucl. Fusion* **26**, 1515.
- [6] WALTZ R.E., DOMINGUEZ R.R., WONG S.K., DIAMOND P.H., LEE G.S., HAHM T.S. and MATTOR N. (1986) *Plasma Phys. Contr. Nucl. Fus. Res.* (Proc. 11th Int. Conf. Kyoto 1986) Vol.1 IAEA Vienna CN-47/A-VI-1-3 (1987) 345.
- [7] PERKINS F.W. (1984) Proc. 4th Int. Symp. on Heating in Toroidal Plasmas, Rome, **2**, 977.
- [8] REDI M., TANG W.M., EFTHIMION P.C., MIKELSEN D.R. and SCHMIDT G.L. (1987) Report PPPL-2368.
- [9] TANG W.M. (1986) *Nucl. Fusion* **26**, 1605.
TANG W.M., BISSHOP C.M., COPPI B. *et al.* (1986) Plasma Physics and Controlled Nuclear Fusion Research (Proc. 11th Int. Conf. Kyoto 1986) Vol.1 IAEA Vienna 1987 337.
- [10] WEILAND J. and NORDMAN H. (1993) *Phys. Fluids B* **5**, 1669.
NORDMAN H., WEILAND J. and JARMÉN A. (1990) *Nucl. Fusion* **30**, 983.
WEILAND J., JARMÉN A. and NORDMAN H. (1989) *Nucl. Fusion* **29**, 1810.
HEIKKILÄ A. and WEILAND J. (1993) *Phys. Fluids B* **5**, 1.
- [11] LUCE T.C., PETTY C.C. and DE HAAS J.C.M. (1992) *Phys. Rev. Lett.* **68**, 52.
- [12] BATEMAN G. (1992) *Phys. Fluids B* **4**, 634.
- [13] RECHESER A.B. and ROSENBLUTH M.N. (1978) *Phys. Rev. Lett.* **40**, 38.
- [14] LOPES CARDOZO N.J. (1994) *Trans. of Fusion Techn.* **25**, 146.
- [15] DUBOIS M. (1994) Invited lecture EPS 1994; to be published in special issue of *Plasma Phys. Contr. Nucl. Fusion*.
- [16] LOPES CARDOZO N.J., SCHÜLLER F.C., BARTH C.J., PIJPER F.J., LOK J. and OOMENS A.A.M. (1994) *Phys. Rev. Lett.* **73**, 256.
- [17] OHKAWA T. (1978) *Phys. Letters* **67A**, 35.
- [18] CHENG C.Z., FURTH H.P. and BOOZER A.H. (1985) Report PPPL-2372.
- [19] HIROE S. *et al.* (1987) *Bull. Am. Phys. Soc.*, **32**, 1806.
- [20] GRUBER O. (1982) *Nucl. Fusion* **22**, 1349.
- [21] TANG W.M., WHITE R.B. and GUZDAR P.N. (1980) *Phys. Fluids* **23**.
- [22] DOMINGUEZ R.R. (1991) *Nucl. Fusion* **31**.
- [23] STRINGER T.E. (1991) submitted to *Nucl. Fusion*.

- [24] DOMINGUEZ R.R. and WALTZ R.E. (1987) *Nucl. Fusion* **27**, 65.
- [25] HASSELBERG G. and ROGISTER A. (1983) *Nucl. Fusion* **23**, 1351.
ROGISTER A., HASSELBERG G. and WAELBROECK F. (1983) KFA Jülich Report Jül-1892.
ROGISTER A., HASSELBERG G., WAELBROECK F.G. and WEILAND J. (1988) *Nucl. Fusion* **28**, 1053.
ROGISTER A., HASSELBERG G., KALECK A., BOILEAU A., VAN ANDEL H.W.H. and VON HELLERMAN (1986) *Nucl. Fusion* **26**, 797.
- [26] DIAMOND P.H. and BIGLARI H. (1990) *Phys. Rev. Lett.* **65**, 2865.
- [27] KADOMTSEV B.B. and POGUTSE O.P. (1978) Plasma Physics and Controlled Nuclear Fusion Research (Proc. 7th Int. Conf. Vienna) Vol. 1, IAEA, Vienna (1979) 649.
- [28] REBUT P.H., BRUSATI M., HUGON M. and LALLIA P. (1986) Plasma Physics and Controlled Fusion Research (Proc. 11th Conf. Kyoto) Vol. 2 IAEA Vienna (1987)
REBUT P.-H. *et al.* (1987) Proc. 14th Eur. Conf. on Contr. Fusion and Plasma Phys., Madrid Part I, 172.
REBUT P.H., LALLIA P.P. and WATKINS M.L. (1988) Plasma Physics and Controlled Nuclear Fusion Research (Proc. 12th Int. Conf. Nice, 1988) **2** IAEA Vienna (1989) 191.
REBUT P.H. and HUGON M. (1991) *Plasma Physics and Controlled Fusion* **33**, 1085.
- [29] ZHANG Y.Z. and MAHAJAN S.M. (1988) *Comments on Plasma Phys. Contr. Fusion* **11**, 243.
- [30] GUZDAR P.N., LIU C.S., DONG J.Q. and LEE Y.C. (1986) *Phys. Rev. Lett.* **57**, 2818.
LEE Y.C., DONG J.Q., GUZDAR P.N. and LIU C.S. (1987) *Phys. Fluids* **30**, 1331.
SINGER S.E. (1988) *Comments Plasma Phys. and Contr. Fusion* **11**, 165.
- [31] BISKAMP D. (1986) IAEA Kyoto, paper CN-47/I-1-5.
- [32] MONTGOMERY D., TURNER L. and VAHALA G. (1979) *Journal of Plasma Physics* **21**, 239.
- [33] KADOMTSEV B.B. (1987) *Phil. Trans. R. Soc. Lond.* **A322**, 125.
- [34] TAYLOR J.B. (1993) *Phys. Fluids B* **5**, 4378.
- [35] KADOMTSEV B.B. (1992) *Plasma Physics and Controlled Fusion* **34**, 1931.
- [36] COPPI B. (1985) *Fizika Plazmy* **11**, 83; *Sov. J. Plasma Phys.* **11**, (1985) 49.
- [37] COPPI B. (1988) *Phys. Lett. A* **128**, 193.
- [38] DNESTROVSKIY YU.N., BEREZOVSKIY E.L., LYSENKO S.E., PIVINSKIY A.A. and TARASYAN K.N. (1991) *Nucl. Fusion* **31**, 1877.

Chapter 5

Ohmic target plasmas

In this chapter ohmic target plasmas in RTP are characterized. Typical observations are reported and the order of magnitude of a number of plasma parameters is given. Special attention is paid to $T_e(r)$ and $n_e(r)$ in low and high q_a plasmas, the current density, the electron collisionality and the electron-ion energy exchange term. Transport is characterized by the global energy confinement time and by the local thermal diffusivity. Some remarks are made concerning electron particle transport in RTP.

5.1 Introduction

In a tokamak the plasma current is usually driven by a toroidal electric field induced by a changing magnetic flux in the central transformer yoke. Electrons and ions are accelerated until the friction between these species eventually compensates the electric force. This friction results in ohmic heating and an increase in the electron temperature T_e . However, since the collision cross-section decreases as T_e increases, the efficiency of the heating process drops. As a consequence, additional heating methods are necessary to achieve the temperatures required for ignition in a fusion reactor.

This chapter is dedicated to the characterization of plasmas in the RTP experiment that are heated solely by the inductively induced plasma current. Although thermonuclear conditions cannot be reached in ohmically heated plasmas, they are important for the understanding of transport for two reasons. Firstly, thermal transport is anomalously high in ohmic plasmas and the dependence of χ_e on plasma parameters might give more insight in the process of anomalous transport (for example: the observation that the energy confinement increases with n_e , but saturates at higher n_e could be caused by an increase of the electron-ion exchange). Secondly, the ohmic plasma is the target plasma, to which additional heating methods can be applied.

A difficulty with transport studies in ohmic plasmas is that the toroidal current density (j) is at the same time the source of heating as well as of the poloidal magnetic field. A change in $j(r)$ can therefore cause a change in transport either because the heat flux changes or because the magnetic field configuration changes, i.e. the field line pitch angle distribution $q(r)$. In additionally heated plasmas this ambiguity is less severe.

Ohmically heated plasmas are characterized by a number of physical quantities which can be measured fairly straightforwardly (like T_e and n_e), and quantities that are indirectly derived from the measured observables (like the thermal diffusivity and the collisionality between plasma species). To get a handle on local transport, fluxes (of particles and energy) as well as the gradients (of density and temperature) must be evaluated locally. The fluxes can be derived from the sources and sinks, which can partly be measured and in part must be derived from modelling. The gradients are determined directly from the measurements of $n_e(r)$ and $T_e(r)$. They are, however, subject to large systematic and statistical errors.

In the following sections, the ohmic parameter space of RTP is explored. Typ-

ical observations are reported and the order of magnitude of a number of plasma parameters is given. Special attention is paid to $T_e(r)$ and $n_e(r)$ in low and high q_a plasmas, the current density distribution and the electron collisionality. Transport is characterized by the global energy confinement time and locally by the thermal diffusion coefficient. A few remarks are made concerning electron particle transport in RTP.

5.2 The RTP parameter regime

The operating regime for a tokamak plasma is limited by the occurrence of disruptions at too high n_e and too low safety factor near the edge, q_a . From an analysis of experimental operating conditions in various tokamaks, the limits of density and plasma current have been plotted in a so called Hugill diagram. In ohmically heated plasmas, it is found that disruptions generally restrict operation to a region where

- the safety factor at the edge $q_a \geq 2$
- and $\frac{\langle n_e \rangle R_0}{B_\phi} \cdot q_a \cdot Z_{\text{eff}} \leq 2 \times 10^{20}$

where $\langle n_e \rangle$ is the volume averaged density ¹, R_0 the major radius, B_ϕ the toroidal magnetic field and Z_{eff} the effective ion charge. For the typical values at RTP ($B_\phi = 2.2$ T, $R_0 = 0.72$ m), the maximum plasma current is restricted to $I_P \leq 190$ kA ($q_a = 2$) and $\langle n_e \rangle \cdot Z_{\text{eff}} \leq 9 \times 10^{19} \text{ m}^{-3}$ at $q_a = 6.8$. Table 5.1 shows typical plasma conditions for standard ohmic discharges in RTP.

5.3 Experimental observations

In this section, observations are reported in ohmic plasmas in RTP. For this purpose, discharges are selected with low and high q_a . Specifically, three typical cases are included in the dataset: $q_a = 6.8$ ($I_P = 60$ kA) with $n_e(0) = 2.6$ and $5.5 \times 10^{19} \text{ m}^{-3}$, and $q_a = 3.3$ ($I_P = 125$ kA) with $n_e(0) = 2.6 \times 10^{19} \text{ m}^{-3}$.

For the low density cases $T_e(r)$ profiles, as measured by the multi-position Thomson scattering system, are shown in Fig. 5.1. Before this diagnostic became available, $T_e(r)$ was measured by single-point Thomson scattering on a shot-to-shot basis. In these experiments it was shown that the reproducibility of ohmic target plasmas was

¹if a parabolic density profile is assumed then $\langle n_e \rangle = \frac{1}{2} \cdot n_e(0)$.

Table 5.1: *Ohmic plasma conditions in the RTP tokamak. The values of T_e , T_i and n_e are given for the plasma centre.*

Quantity	Symbol	Expression	Value	Unit
Major radius	R_0		0.72	m
Minor radius	a		0.164	m
Plasma volume	V	$\pi a^2 2\pi R_0$	0.4	m ³
Inverse aspect ratio	ϵ	r/R_0	$a/R_0 = 0.22$	
Toroidal field at R_0	B_ϕ		1.9 - 2.4	T
Plasma current	I_P		40 - 145	kA
Safety factor	q		$q_a = 3 - 7$	
Effective ion charge	Z_{eff}	$(\sum_i n_i Z_i^2)/n_e$	1 - 8	
Ion mass	A		1 - 20	amu
Loop voltage	V_L		1.5 - 3.0	V
Electron temperature	T_e		0.6 - 1.1	keV
Ion temperature	T_i		0.5 - 0.7	keV
Electron density	n_e		$(0.5 - 10) \times 10^{19}$	m ⁻³
Pulse duration			500	ms

good; the shot to shot variation of T_e is $\sim 5\%$. The observation that $T_e(r)$ is more peaked at lower currents, is consistent with observations in other tokamaks.

Electron density profiles $n_e(r)$ are measured by the 19-chord interferometer. Figure 5.2 shows typical profiles for low and higher n_e plasmas ($n_e(0) = 2.6 \times 10^{19}$ and $5.5 \times 10^{19} \text{ m}^{-3}$), q_a is 3.3 and 6.8, respectively. The shape of $n_e(r)$ is independent of \bar{n}_e for constant plasma current. At low q_a , $n_e(r)$ becomes broader. The broadening of $T_e(r)$ and $n_e(r)$ at higher plasma current is consistent with the concept of profile consistency [1].

For constant q_a , there is no dependence of $T_e(0)$ on $n_e(0)$ [2] as long as $n_e(0) < 5 \times 10^{19} \text{ m}^{-3}$. For higher densities $T_e(0)$ slightly decreases (τ_E saturates at high n_e).

Measurements of the ion temperature T_i are scarce. For a limited number of plasma conditions $T_i(0)$ has been measured by the neutral particle analyzer. Typically, $T_i(0) = 0.7 T_e(0)$.

Radiation losses in ohmically heated plasmas are dominated by line radiation of impurities in the plasma. For low Z impurities (like C and O) the radiation level is low in the centre and high in the edge. High Z impurities (like Fe) will radiate dramatically in the centre, but normally the densities of these impurities can be kept low.

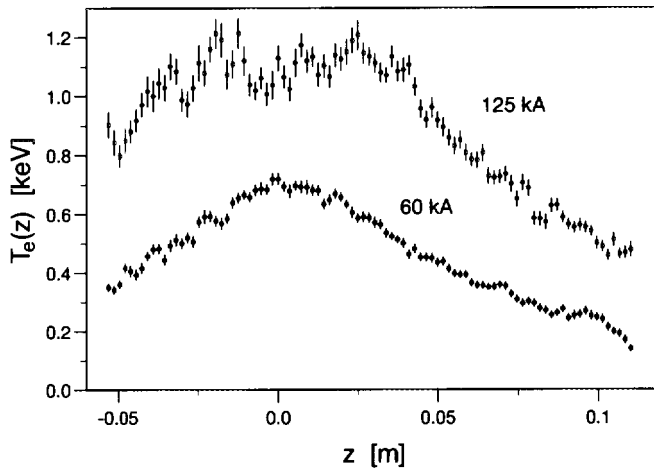


Figure 5.1: *The electron temperature profile as measured by the multiposition Thomsons scattering diagnostic, for $q_a = 6.8$ and $q_a = 3.3$ ($n_e(0) = 2.6 \times 10^{19} \text{ m}^{-3}$; $Z_{\text{eff}} = 1.5$).*

From bolometer measurements, the total radiated power in RTP is typically 20 kW (20% of the ohmic input power) in a hydrogen plasma with $q_a = 6.8$, $n_e(0) = 2.6 \times 10^{19} \text{ m}^{-3}$ and $Z_{\text{eff}} = 1.8$. Bremsstrahlung losses can be neglected ($\leq 1\%$ of P_Ω).

In ohmic plasmas with higher currents sawteeth occur. Although the mechanism is not fully understood, the sawtooth crash is generally believed to be induced by an $m = 1$ MHD instability. In high current plasmas, the safety factor on axis can be smaller than 1 (in RTP typically when $I_P \geq 90 \text{ kA}$). Within the $q = 1$ volume, a redistribution of energy and particles occurs, leading to a flattening of $T_e(r)$ and $n_e(r)$. A heat and density pulse is then propagating radially towards the edge. In RTP, the sawteeth occur at a frequency of 0.5 - 1.5 kHz (lowest frequency corresponds to highest n_e). The perturbations in T_e and n_e can be observed time resolved by the ECE radiometer and the interferometer, respectively. Sawtooth induced heat and density pulse propagation have been studied extensively in RTP [3].

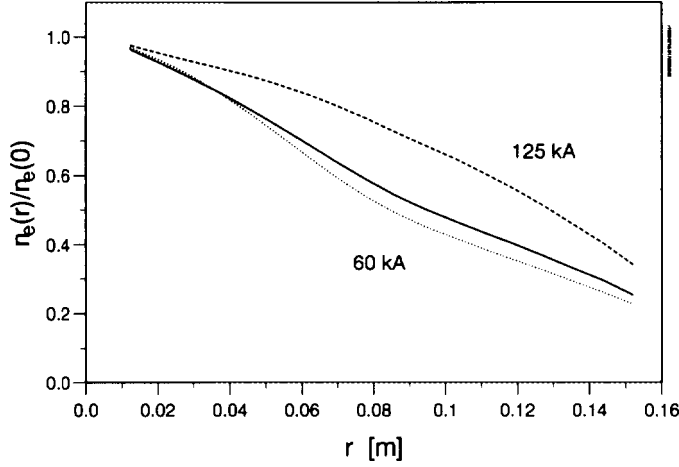


Figure 5.2: *Normalized electron density profile as measured by the interferometer for $q_a = 6.8$ with $n_e(0) = 2.6$ and $5.5 \times 10^{19} \text{ m}^{-3}$, and $q_a = 3.3$ with $n_e(0) = 2.6 \times 10^{19} \text{ m}^{-3}$. A broadening of $n_e(r)$ is observed for the higher current.*

5.4 Physical parameters

In this section typical values and radial dependencies of some plasma parameters are given. Appendix A gives the expression for a number of relevant physical quantities and their values for ohmically heated target plasmas at RTP. In this section, the radial dependencies of some quantities are presented.

5.4.1 Current density profile and bootstrap current

The current density profile, $j(r)$, is determined from the temperature dependent electrical conductivity. Figure 5.3 shows a typical current density profile for a total plasma current of $I_P = 60$ and 125 kA. The shape of $j(r)$ is obtained assuming neoclassical resistivity as calculated by the SNAP transport code. The absolute value of $j(r)$ is given by the total plasma current. Note that on-axis

$$q_0 = \frac{2B_\phi}{\mu_0 j_0 R_0}. \quad (5.1)$$

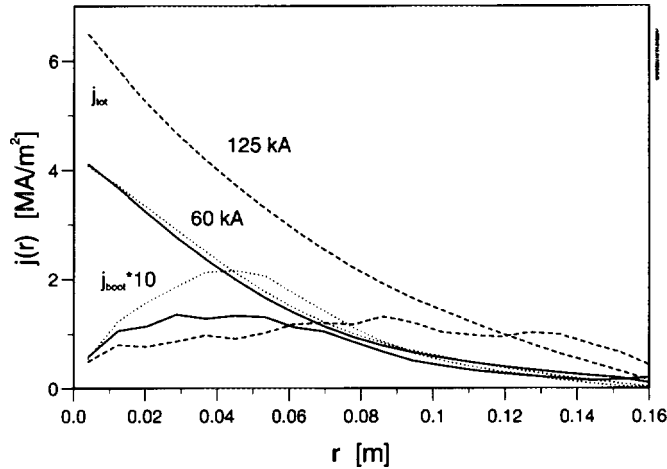


Figure 5.3: Total current density profile for $I_P = 60$ and 125 kA for the 3 cases of Fig. 5.2, as calculated by SNAP. Also shown is the bootstrap current (multiplied by 10).

Inserting j_0 (see Fig. 5.3) shows that $q_0 < 1$ for the 125 kA discharge, and $q_0 > 1$ for 60 kA ($B_\phi = 2.2$ T).

In a plasma with low collisionality, a fraction of particles is trapped by the magnetic field gradient. In the presence of density and temperature gradients, a net current is generated in toroidal direction, which is called the bootstrap current² [4]. In the regime of low collisionality and large aspect ratio limit with circular magnetic surfaces, the bootstrap current is given by (to first order $\epsilon^{1/2}$) [5]:

$$j_{BS} = -\epsilon^{1/2} \frac{en_e T_e}{B_\theta} \left\{ -2.44 \left(1 + \frac{T_i}{T_e} \right) \frac{\nabla n_e}{n_e} - 0.69 \frac{\nabla T_e}{T_e} + 0.42 \frac{\nabla T_i}{T_e} \right\} \quad (5.2)$$

where ϵ is the local aspect ratio, B_θ the local poloidal magnetic field, and the prime denotes spatial derivative with respect to r . The bootstrap current is zero at the centre and goes to zero at the edge. It tends to broaden the total $j(r)$.

²It was originally hoped for that this current could sustain the plasma current, without need for an inductively driven one; similar to Baron von Munchhausen who wanted to lift himself from the pool by pulling his bootstraps. Experimentally, situations with 80% bootstrap current have been achieved.

The total bootstrap current is given by integrating Eq.(5.2) over the poloidal cross section. A rough estimate for the total bootstrap current is: ³

$$I_{BS} = 0.38\epsilon^{1/2}\beta_p I_P \quad (5.3)$$

which reduces for the RTP parameters to $I_{BS} = 0.18 \beta_p I_P$. For $\beta_p = 0.3$ the bootstrap current is about 5% of the plasma current. The radial distribution of the bootstrap current as calculated by the SNAP transport code is also shown in Fig. 5.3.

5.4.2 Internal inductance

The peaking of $j(r)$ is often expressed in terms of the normalized internal inductance of the plasma column, given by

$$l_i = \frac{\int_0^a (B_\theta^2(r)/2\mu_0) 2\pi r dr}{(B_\theta^2(a)/2\mu_0) \pi a^2} \quad (5.4)$$

where B_θ is the poloidal magnetic field. To estimate l_i [7], one can assume the current density profile of Kadomtsev [8] and Taylor [9]:

$$j^{KT}(r) = j(0) \cdot \left\{ 1 + \left(\frac{r}{a}\right)^2 \left(\frac{q_a}{q_0} - 1\right) \right\}^{-2}, \quad (5.5)$$

which then gives

$$l_i = \left(\frac{q_a}{q_a - q_0} \right)^2 \log \frac{q_a}{q_0} - \frac{q_a}{q_a - q_0}. \quad (5.6)$$

For $q_a = 6.8$ and $q_0 = 1.2$ this gives $l_i = 1.3$.

5.4.3 Collisionality

The electron collisionality is given in terms of measurable plasma parameters by

³Reference [6] gives an expression for the total bootstrap current in terms of profile shape parameters. The total bootstrap current is calculated for profile shapes $j(r) = j_0(1 - r^2/a^2)^{\alpha_J}$, etc. with $\alpha_T = 3/2$, $\alpha_n = 1/2$ and $\alpha_J = 2$.

$$\nu_e^*(r) = 4.9 \times 10^{-24} \frac{n_e(r)q(r)}{T_e^2(r) r^{3/2}} \ln \Lambda Z_{\text{eff}} R_0^{5/2}, \quad (5.7)$$

where $\ln \Lambda$ is the Coulomb logarithm and T_e is expressed in [keV]. The transition of the banana regime to the plateau regime occurs where $\nu_e^* = 1$, while the transition to the Pfirsch-Schlüter regime takes place when $\nu_e^* = (\frac{R_0}{r})^{3/2}$ (for RTP, $(\frac{R_0}{a})^{3/2} = 9.5$).

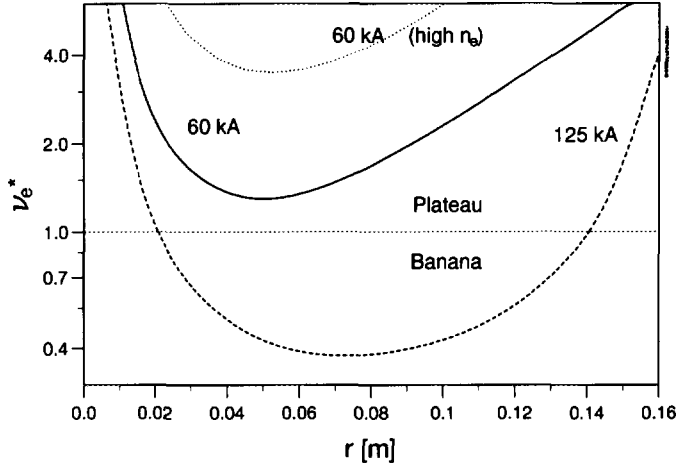


Figure 5.4: *Radial dependence of the electron collisionality ν_e^* for $I_P = 60$ kA ($n_e(0) = 2.6$ and $5.5 \times 10^{19} \text{ m}^{-3}$) and $I_P = 125$ kA ($n_e(0) = 2.6 \times 10^{19} \text{ m}^{-3}$).*

Figure 5.4 shows profiles of ν_e^* for the dataset selected in this chapter. It is observed that $\nu_e^* \leq 1$ for $I_P = 125$ kA, which implies that a considerable fraction of electrons is trapped in banana orbits. For lower plasma current the fraction diminishes due to the higher q value and the lower T_e .

The transition from banana to plateau regime is numerically treated by SNAP as a smooth one. This explains why, even for $\nu_e^* > 1$, there is a neoclassical correction to the plasma conductivity.

From Fig. 5.4 one can conclude that ohmic plasmas in RTP at low current have the electrons in the plateau regime, while at high currents the electrons are in the banana regime for most of the cross-section.

5.5 Transport

5.5.1 Energy confinement

An important tool in the search for the dependence of transport on plasma parameters are scaling laws. There are two types of confinement scaling which should not be mixed: (i) τ_E as function of engineering parameters, i.e. knobs and switches one can turn independently: I_P , B_T , $\langle n \rangle$, R/a , triangularity, P_{add} , Z_{eff} , and (ii) τ_E as function of dimensionless parameters: β , ν_e^* , q_a , shear s , magnetic Reynolds number, etc. The first type of scaling is useful for finding an optimum for machine operation or predicting future machines, while dimensionless scaling laws are useful for identifying physics mechanisms. In the present characterization of ohmic target plasmas engineering scaling laws will be used.

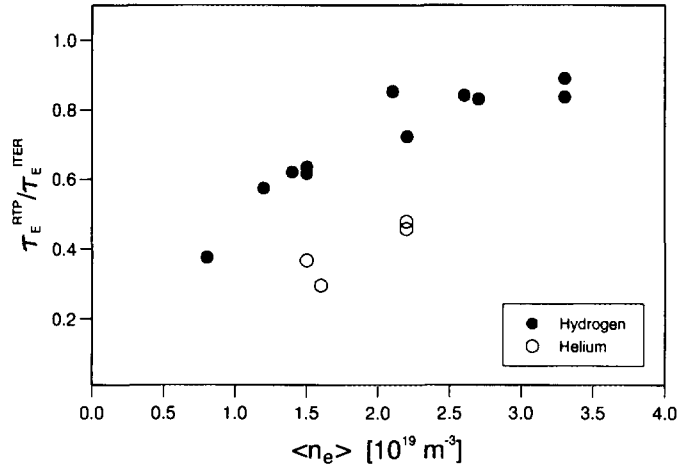


Figure 5.5: The ratio $\tau_E^{\text{RTP}} / \tau_E^{\text{ITER89-P}}$ as function of the line averaged density. At higher n_e , i.e. in the SOC regime, $\tau_E^{\text{ITER89-P}}$ is a good estimator for τ_E^{RTP} . Shown are hydrogen (closed symbols) and helium discharges (open symbols).

For RTP, the energy confinement time has been calculated over a wide range of parameters ($q_a = 3.3 - 6.8$, $n_e(0) = (1.1 - 7.5) \times 10^{19} \text{ m}^{-3}$). The energy confinement

is observed to increase linearly with n_e for $n_e(0) \leq 5 \times 10^{19} \text{ m}^{-3}$ [2]. This is called the linear ohmic confinement (LOC) regime. At higher densities, τ_E saturates. This is called the saturated ohmic confinement (SOC) regime and is a common observation in tokamaks.

A comparison is made with the ITER89-P L-mode scaling [10] which is based on confinement data of larger tokamaks, which are in the L-mode regime:

$$\tau_E^{\text{ITER89-P}} = 48 I_p^{0.85} R^{1.2} a^{0.3} \kappa^{0.5} \bar{n}^{0.1} B_T^{0.2} A_i^{0.5} P_{\text{TOT}}^{-0.5}, \quad (5.8)$$

where κ is the elongation, B_T the toroidal magnetic field, A_i the atomic mass and P_{TOT} the total input power. Units are [ms], [MA], [m], [10^{20} m^{-3}], [T] and [MW]. Figure 5.5 shows the ratio $\tau_E^{\text{RTP}}/\tau_E^{\text{ITER89-P}}$ as function of the line averaged density. At higher n_e , i.e. in the SOC regime, $\tau_E^{\text{ITER89-P}}$ is a good estimator for τ_E^{RTP} . The separated data points are helium discharges, and demonstrate that scaling with ion mass (ITER89-P) is not observed in RTP. However, it should be noted that ITER89-P is established for hydrogenic ion plasmas. Maybe the scaling should be extended with a Z_i dependence.

5.5.2 Local thermal transport

By solving the balance equation of thermal sources and sinks, the thermal flux can be computed as function of radius. The ohmic power deposition typically has a central power density of 2 MW/m^3 for $I_p = 60 \text{ kA}$. In ohmically heated plasmas with low radiation level ($p_{\text{RAD}} \ll p_\Omega$), the electron-ion exchange is the largest sink term in the power balance. The exchange is given by

$$p_{ei} = \frac{n_e(T_e - T_i)}{\tau_{ei}} \sim \ln \Lambda Z_{\text{eff}} n_e^2 \frac{(T_e - T_i)}{T_e^{3/2}}. \quad (5.9)$$

The dependence of p_{ei} on density ⁴ is illustrated in Fig. 5.6, where $T_i(r) = 0.7 * T_e(r)$ has been assumed, thus $p_{ei} \sim n_e^2 T_e^{-1/2}$. Comparison of the low and high q_a cases shows that the exchange is not too different, since the higher T_e (at $q_a = 3.3$) is compensated by a broader $n_e(r)$. Even at high n_e the heat exchange is small compared to the ohmic input power density ($p_{ei} \ll p_\Omega \simeq 2 \text{ MW/m}^3$). Therefore, the ions are not important in the local power balance at RTP.

⁴It is well possible that in the Saturated Ohmic Confinement regime $p_{ei} \simeq 0.5 p_\Omega$.

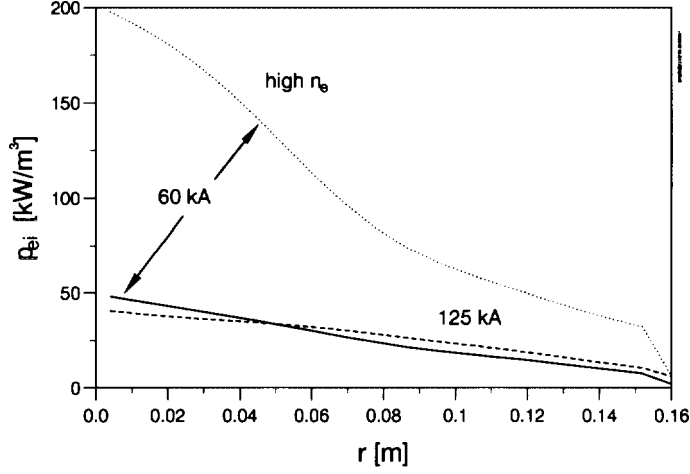


Figure 5.6: *Electron-ion exchange power density for the ohmic dataset. In the analysis we have taken $T_i(r) = 0.7 * T_e(r)$.*

The electron heat diffusivity obtained from power balance analysis, is given by

$$\chi_e^{\text{pb}}(r) = -\frac{q_e(r)}{n_e(r)\nabla T_e(r)} \quad (5.10)$$

where q_e is the electron heat flux. Typically, χ_e^{pb} has a value between 0.1 and 10 m^2/s . Figure 5.7 shows χ_e^{pb} for plasma currents of 60 and 125 kA. The lowest $\chi_e^{\text{pb}}(r)$ in Fig. 5.7 corresponds to the highest density ($n_e(0) = 5.5 \times 10^{19} \text{ m}^{-3}$, $I_P = 60 \text{ kA}$), and clearly demonstrates the scaling $\chi_e \sim n_e^{-1}$.

From the phase velocity and the amplitude of the heat pulses, induced by e.g. sawtooth crashes, an incremental diffusion coefficient can be obtained which is defined as:

$$\chi_e^{\text{inc}} = -\frac{\partial q_e}{\partial(n_e \nabla T_e)}. \quad (5.11)$$

It is generally observed in tokamaks that χ_e^{inc} exceeds χ_e^{pb} by a factor 2-4. This means that q_e is not a purely linear function of $n_e \nabla T_e$, but given by either an offset-linear (critical gradient, heat pinch) or a non-linear relation.

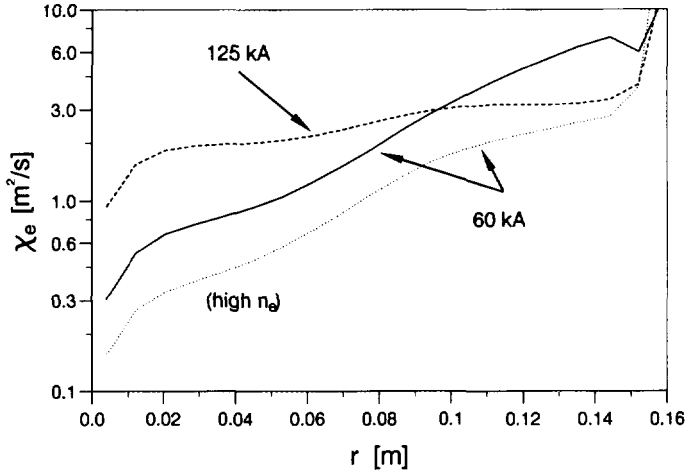


Figure 5.7: *The electron thermal diffusivity from the power balance analysis, as calculated by SNAP. Conditions are $I_P = 60$ kA ($n_e(0) = 2.6$ and $5.5 \times 10^{19} \text{ m}^{-3}$) and $I_P = 125$ kA ($n_e(0) = 2.6 \times 10^{19} \text{ m}^{-3}$).*

5.5.3 Particle transport

In steady state plasmas, particle transport is difficult to quantify since the net particle flux Γ_e is zero. The outward diffusion of particles is balanced by inward convection, the ‘particle pinch’. There are no diagnostics at RTP that measure the particle sources and sinks (e.g. radiative recombination). However, analysis of propagation of density pulses gives information on the (perturbed) particle flux. For example, in ASDEX an incremental particle diffusion coefficient is obtained by gas feed modulation [12]. In JET, the incremental particle diffusion coefficient is obtained from the density pulse following the sawtooth collapse [13]. Typically, $D^{\text{inc}}/\chi_e^{\text{inc}} \simeq 0.1$.

It is possible to calculate the particle pinch inside the sawtooth inversion radius from the relaxation of the density profile after the collapse. From the rate of change ($\partial n_e / \partial t$) the inward particle flux can be estimated from the conservation equation for particles:

$$\frac{\partial n_e}{\partial t} + \nabla \Gamma_e = S_e \quad (5.12)$$

where Γ_e is the electron particle flux. The particle source term S_e is small in the plasma centre. The only likely source of particles is the ionization of neutrals, which

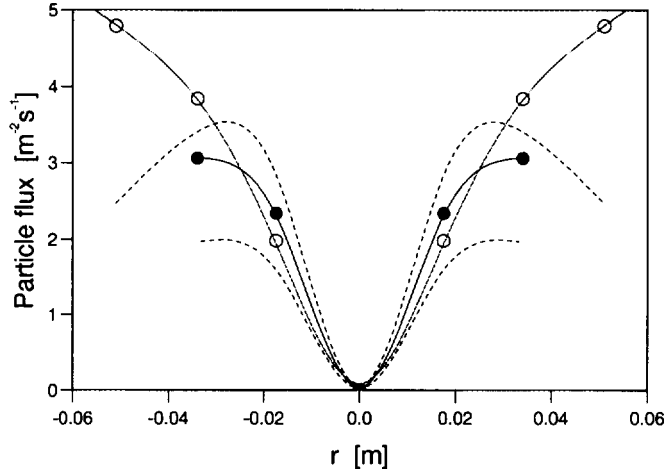


Figure 5.8: *The inward particle flux measured just after a sawtooth collapse. Plasma conditions are: $I_P = 125$ kA with $n_e(0) = 2.6 \times 10^{19} \text{ m}^{-3}$ (solid symbols) and $I_P = 145$ kA with $n_e(0) = 7.0 \times 10^{19} \text{ m}^{-3}$ (open symbols). A comparison is made with the neoclassical Ware pinch (dashed lines). For the poloidal field, needed to calculate the Ware pinch, the current distribution as calculated by the SNAP code has been used.*

is usually balanced by a sink term due to recombination. For the particle flux,

$$\int_V \vec{\nabla} \cdot \vec{\Gamma}_e dV = \int_A \vec{\Gamma}_e \cdot d\vec{A} \quad (5.13)$$

where V is the volume of a flux surface with area A . Assuming a uniformly distributed particle flux over the surface A , one gets:

$$|\Gamma_e| = \frac{1}{A} \int_V \frac{\partial n_e}{\partial t} dV. \quad (5.14)$$

The inward particle velocity v_p is calculated from the particle transport equation:

$$\Gamma_e = -D\nabla n_e + n_e v_p. \quad (5.15)$$

Just after the sawtooth collapse, $n_e(r)$ is flat, and the convective term $n_e v_p$ dom-

inates. Figure 5.8 shows the obtained particle flux for low and high density sawtooth discharges. Typically, for $n_e = 2.5 \times 10^{19} \text{ m}^{-3}$, an inward particle flux $\Gamma_e = (2.5 \pm 0.5) \times 10^{19} \text{ m}^{-2}\text{s}^{-1}$ is found, and $v_p = 1.2 \pm 0.2 \text{ m/s}$ (at $r/a = 0.2$).

The particle pinch can be compared to the neoclassical Ware pinch [14] given by [15]:

$$\Gamma_W = -1.67 \epsilon^{1/2} \frac{E_\phi}{B_\theta} n_e \quad (5.16)$$

where E_ϕ is the toroidal electric field and B_θ the poloidal magnetic field. Figure 5.8 shows a comparison of the particle pinch just after a sawtooth collapse, and the neoclassical Ware pinch. Although the uncertainty in the calculation of Γ_W is large (given by the uncertainty in E_ϕ which is measured at the plasma edge), $\Gamma_W \simeq \Gamma_e$. Note that Γ_e is measured near the plasma centre. At high density steady state plasmas, $\Gamma_e = 0$ throughout the plasma except for the very edge. This means that $v_p = D/L_n$. Since L_n decreases towards the edge, v_p has to increase with radius, even faster than D ($\propto \chi$). On the other hand, the Ware pinch decreases towards the edge. One must conclude that the Ware pinch is not the explanation of the inward particle pinch needed to sustain a peaked $n_e(r)$.

From the obtained v_p , the particle diffusion coefficient can be estimated in steady state, when $\Gamma_e = 0$. Assuming $L_n = n_e/\nabla n_e \simeq 0.2 \text{ m}$, the reasonable value [16] of $D = 0.25 \text{ m}^2/\text{s}$ is obtained.

5.6 Summary

In the RTP experiment, ohmically heated target plasmas have been analyzed. Over a wide range of parameters, including scans of plasma current, n_e and Z_{eff} , typical physical quantities have been established. Some parameters were not available from the experiment, like T_i , $Z_{\text{eff}}(r)$ and detailed radiation terms. For these parameters educated guesses had to be made.

The energy confinement time is consistent with scaling laws derived for other experiments. Saturation of τ_E at higher densities is also a common observation.

The electron collisionality is below unity in high current plasmas, and has a value between 2 - 10 for lower current plasmas. Hence, collisional transport in RTP is close to the transition between the banana and plateau regime.

5.7 Appendix A

The following table gives the expression and typical values for plasma parameters in RTP.

Units are $T_{e,i}$ in [keV], $n_{e,i}$ in [m^{-3}], B in [T], and I_P in [kA].

Quantity		Expression	Numerically	Value (*)	
Current density	j			4×10^6	A/m ²
Internal inductance	l_i	$\frac{\int_0^a (B_\theta^2(r)/2\mu_0)2\pi r dr}{(B_\theta^2(a)/2\mu_0)\pi a^2}$		1.3	
Drift velocity	v_D	$\frac{j}{n_e e}$		1×10^6	m/s
Safety factor	q	$\frac{r B_\phi}{R_0 B_\theta}$			
" at edge	q_a	$\frac{2\pi a^2 B_\phi}{R_0 \mu_0 I_P}$	$187 \frac{B_\phi}{I_P}$	6.8	
" at centre	q_0	$\frac{2B_\phi}{\mu_0 j_0 R_0}$		1.2	
Poloidal magn. field	B_θ	$\frac{\mu_0 \int j(r) dS}{2\pi r}$			T
" at edge	$B_\theta(a)$	$\frac{\mu_0 I_P}{2\pi a}$	$1.22 \times 10^{-3} I_P$	7.3×10^{-2}	T
Thermal energy	W	$\int dV (3/2) [n_e T_e + n_i T_i]$		4×10^2	J
Kinetic pressure	P_K	$(3/2) [n_e T_e + n_i T_i]$		7.2×10^3	J m ⁻³
Magnetic pressure	P_B	$\frac{B^2}{2\mu_0}$		1.9×10^6	J m ⁻³
Beta poloidal	β_p	$\frac{\int P_K dS / dS}{B_\theta^2 / 2\mu_0}$		0.3	
Beta toroidal	β_T	$P_K / P_B = \beta_p \cdot \frac{B_\theta^2}{B_\phi^2}$		3.7×10^{-3}	
El. thermal velocity	$v_{th,e}$	$(2k_b T_e / m_e)^{1/2}$	$1.8755 \times 10^7 T_e^{1/2}$	1.6×10^7	m/s
Ion thermal velocity	$v_{th,i}$	$(2k_b T_i / m_i)^{1/2}$	$4.377 \times 10^5 \left(\frac{T_i}{A}\right)^{1/2}$	3.1×10^5	m/s
Ion-acoustic velocity	c_s	$(k_b T_e / m_i)^{1/2}$	$3.095 \times 10^5 \left(\frac{T_e}{A}\right)^{1/2}$	2.6×10^5	m/s

Quantity		Expression	Numerically	Value (*)	
Alfvén velocity	v_A	$B_\phi(\mu_0 n_i m_i)^{-1/2}$	$2.18 \times 10^{16} \frac{B_\phi}{\sqrt{n_i A}}$	9.6×10^6	m/s
El. cyclotron freq.	ω_{ce}	$\frac{eB_\phi}{m_e}$	$1.76 \times 10^{11} B_\phi$	3.9×10^{11}	rad/s
Ion cyclotron freq.	ω_{ci}	$\frac{ZeB_\phi}{m_i}$	$9.58 \times 10^7 B_\phi Z/A$	2.1×10^8	rad/s
Electron plasma freq.	ω_{pe}	$\left(\frac{n_e e^2}{m_e \epsilon_0}\right)^{1/2}$	$56.4 \sqrt{n_e}$	2.8×10^{11}	rad/s
Ion plasma freq.	ω_{pi}	$\left(\frac{n_i Z^2 e^2}{m_i \epsilon_0}\right)^{1/2}$	$1.32 Z \frac{\sqrt{n_i}}{A}$	6.6×10^9	rad/s
Trapped bounce freq.	ω_{be}	$\epsilon^{1/2} \frac{v_{th,e}}{(qR_0)}$			rad/s
Electron gyroradius	ρ_e	$v_{th,e}/\omega_{ce}$	$1.07 \times 10^{-4} T_e^{1/2}/B_\phi$	4.1×10^{-5}	m
Ion gyroradius	ρ_i	$v_{th,i}/\omega_{ci}$	$4.57 \times 10^{-3} \frac{(T_i A)^{1/2}}{B_\phi Z}$	1.5×10^{-3}	m
	ρ_s	c_s/ω_{ci}	$3.23 \times 10^{-3} \frac{(T_e A)^{1/2}}{B_\phi Z}$	1.2×10^{-3}	m
Debye shielding dist.	λ_D	$\left(\frac{\epsilon k_b T_e}{n_e e^2}\right)^{1/2}$	$2.35 \times 10^5 (T_e/n_e)^{1/2}$	3.9×10^{-5}	m
Coulomb logarithm	$\ln \Lambda$		$37.8 - \ln(n_e^{1/2}/T_e)$	15	
Electron coll. time	τ_e	$c_1 \frac{\epsilon_0^2 (k_b m_e T_e)^{1/2}}{n_i Z^2 e^4 \ln \Lambda}$	$1.09 \times 10^{16} \frac{T_e^{3/2}}{n_i Z^2 \ln \Lambda}$	1.7×10^{-5}	s
Ion coll. time	τ_i	$c_2 \frac{\epsilon_0^2 (k_b m_i T_i)^{1/2}}{n_i Z^4 e^4 \ln \Lambda}$	$6.60 \times 10^{17} \frac{A^{1/2} T_i^{3/2}}{n_i Z^4 \ln \Lambda}$	6.2×10^{-4}	s
Heat exchange time	τ_{ei}	$\frac{m_i}{2m_e} \tau_e$	$0.99 \times 10^{19} \frac{A T_e^{3/2}}{n_i Z^2 \ln \Lambda}$	1.5×10^{-2}	s
El. collisionality	ν_e^*	$\frac{\nu_e q R_0}{\epsilon^{3/2} v_{th,e}}$	$4.9 \times 10^{-24} \frac{n_e q R_0^{5/2} Z}{T_e^2 r^{3/2}} \ln \Lambda$		
Classical resistivity	η	$\frac{m_e}{n_e e^2 \tau_e}$	$5.0 \times 10^{-5} \frac{Z \ln \Lambda}{T_e^{3/2}}$	5.0×10^{-8}	Ωm
Toroidal electric field	E	$V_L/(2\pi R_0)$	$0.22 V_L$	0.4	V/m
Runaway el. field	E_c		$2.6 \times 10^{-20} \frac{n_e}{Z T_e} \ln \Lambda$	16.3	V/m

(*): Values are calculated at the plasma centre, unless stated otherwise. Assumptions are: $I_P = 60$ kA, $T_e = 0.7$ keV, $T_i = 0.5$ keV, $A = 1$, $Z_{\text{eff}} = 1$ and $n_e(0) = 2.5 \times 10^{19} \text{ m}^{-3}$. In the table, k_b is Boltzmann's constant, $c_1 = 3(2\pi)^{3/2}$ and $c_2 = 12\pi^{3/2}$.

References

- [1] SCHÜLLER F.C. *et al.* (1990) Proc. 18th Conf. on Controlled Fusion and Plasma Physics, Berlin.
- [2] KONINGS J.A., HOGWEIJ G.M.D., LOPES CARDOZO N.J., OOMENS A.A.M., SCHÜLLER F.C. and the RTP team (1994) *Plasma Physics and Controlled Fusion* **36**, 45.
- [3] HOGWEIJ G.M.D. *et al.* (1992) Proc. 19th Eur. Conf. on Contr. Fusion and Plasma Phys., Innsbruck, Vol. I p.75.
- [4] CORDEY J.G., CHALLIS C.D. and STUBBERFIED P.M. (1988) *Plasma physics and Controlled Fusion* **30**, 1625-1635.
- [5] ROSENBLUTH M.N., HAZELTINE R.H. and HINTON F.L. (1972) *Phys. Fluids* **15**, 116.
- [6] WILSON J.B. (1992) *Nucl. Fusion* **32**, 257.
- [7] OOMENS A.A.M. (1994) *Trans. of Fusion Techn.* **25**, 267.
- [8] KADOMTSEV B.B. (1987) *Phil. Trans. R. Soc. Lond.* **A322**, 125.
- [9] TAYLOR J.B. (1990) *Rapport IFSR* 447.
- [10] YUSHMANOV P.N. *et al.* (1990) *Nucl. Fusion* **30**, 1999.
- [11] WATKINS M.L. *et al.* (1976) *Methods Comput. Phys.* **16**, 165.
- [12] GENTLE K.W., GEHRE O. and KRIEGER K. (1992) *Nucl. Fusion* **32**, 217.
- [13] HOGWEIJ G.M.D. *et al.* (1991) *Plasma Physics and Controlled Fusion* **33**, 189; see also JET-P (1990) 45.
DE HAAS J.C.M. *et al.* (1991) *Nucl. Fusion* **31**, 1261.
- [14] WARE A.A. (1970) *Phys. Rev. Lett.* **25**, 15.
- [15] BALESCU R. (1988) Transport processes in plasmas, Part 2: Neoclassical transport theory, Elsevier Science Publishers B.V., Amsterdam.
- [16] BALET B. *et al.* (1993) *Nucl. Fusion* **33**, 1345.

Chapter 6

Transport analysis in RTP

This chapter has been published as:

Transport analysis in ohmic and ECR heated plasmas in the RTP tokamak

J.A. KONINGS, G.M.D. HOGWEIJ, N.J. LOPES CARDOZO,
A.A.M. OOMENS, F.C. SCHÜLLER and the RTP team

in *Plasma Physics and Controlled Fusion* **36** (1994) 45.

Abstract: *Global and local power balance studies in ohmic and ECR heated plasmas in the RTP tokamak ($R_0 = 0.72$ m, $a = 0.16$ m, $B_T = 2.14$ T) are reported, and compared with models. In ohmic plasmas the energy confinement time is consistent with the Goldston-ohmic scaling law. Using ECRH, high T_e and ∇T_e are obtained. An updated version of the Rebut-Lallia-Watkins transport model successfully describes χ^{eff} in these extreme plasma conditions. Improved confinement ($\tau_E^{\text{ECRH}} = 2 \cdot \tau_E^{\Omega}$) is observed in low density, low current plasmas when the ECRH power is comparable to the ohmic input power.*

6.1 Introduction

The Rijnhuizen Tokamak Project (RTP) is dedicated to the study of transport processes in tokamak plasmas. For this purpose, the tokamak is equipped with a number of high resolution diagnostics. Transport studies are performed in ohmic plasmas and plasmas with Electron Cyclotron Resonance (ECR) heating.

ECR heating has been studied extensively in PDX, DIII-D, DITE, TFR, TEXT, T-10, JFT-2M, and TCA [1]. Characteristic observations with the EC resonance near the magnetic axis are an increase of the central electron temperature and a peaking of the profile, a decrease of the loop voltage, a flattening of the electron density profile and a deterioration of confinement for high power ECRH. In the RTP experiment, similar observations have been made with ECRH (60 GHz, 100 ms, 180 kW O-mode) launched from the low field side [2].

In this paper the effect of ECRH on local transport is investigated. ECRH is used to induce extreme plasma conditions for which transport models are tested. The global energy confinement time is compared to scaling laws. A steady-state local power balance analysis is performed and a comparison is made with the Rebut-Lallia-Watkins transport model. Special attention is paid to the ECR power deposition profile, which is deduced from ray tracing calculations and ECR modulation studies.

6.2 Experimental

6.2.1 RTP

The RTP tokamak (major radius $R_0 = 0.72$ m, minor radius $a = 0.16$ m) has a maximum toroidal field $B_T = 2.4$ T, plasma current $I_P \leq 150$ kA and a discharge duration of 250 ms. The results reported in this paper have been obtained in hydrogen and helium plasmas with line averaged electron densities $\bar{n}_e = (0.5 - 4) \times 10^{19}$ m⁻³, plasma currents $I_p = 60 - 125$ kA, toroidal magnetic field $B_T = 2.14$ T and central electron temperature $T_e(0) = (0.5 - 0.9)$ keV in the ohmic phase. Typically, $Z_{\text{eff}} = 2 - 4$ (in the experimental period before the vessel was boronized) and $1 - 2$ (after boronization).

6.2.2 ECRH

Electron Cyclotron Resonance Heating is applied using a single Varian pulse-type gyrotron (60 GHz, 100 ms) operated at nominal power levels of 60 - 180 kW. The

TE₁₁ O-mode (mode purity 90%) [3] is launched in the mid-plane, perpendicular to the toroidal field, from the low field side.

Transmitted ECR power is measured using an array of nine antenna horns placed in an orthogonal cross at the high field side facing the ECR launcher. In this way the beam width and position are obtained in toroidal and poloidal direction [4].

6.2.3 Diagnostics

The RTP experiment is equipped with diagnostics to perform detailed transport studies, including a scannable, single-point Thomson scattering system [5], a 20-channel double-heterodyne ECE radiometer [6], a 19-chord interferometer [7], a 6-channel ECE polychromator [8], a SXR pulse height analyser [9], 80-channel 5-camera SXR tomography [10], an XUV spectrometer, HXR and visible light monitors, a bolometer and a neutral particle analyser.

The 20-channel ECE radiometer operates in second harmonic X-mode. An absolute calibration is done against Thomson scattering in high density ohmic plasmas ($n_e(0) = 7 \times 10^{19} \text{ m}^{-3}$). A correction is made for finite optical thickness. In ECR heated plasmas with low density ($n_e \leq 2.5 \times 10^{19} \text{ m}^{-3}$) suprathermal electrons may contribute to the ECE signal, leading to an overestimate of T_e in the channels on the low field side. For these cases, only the high field side ECE channels were used for T_e -profile analysis.

6.3 Local Power Balance analysis

A local power balance analysis (LPB) is performed using an adapted version of the time-independent 1-D transport code SNAP developed at PPPL [11]. Assuming toroidal symmetry and circular flux surfaces, local transport coefficients are calculated in steady-state plasmas.

The measured input parameters are I_P , loop voltage, $T_e(r)$ from Thomson scattering and ECE, $n_e(r)$ from the interferometer, and ion temperature T_i measured for some discharges by the neutral particle analyser. The calculation of the total ECR power and the deposition profile is discussed in section 6.4.1. Radiation losses (P_{RAD}) are estimated from XUV spectroscopy and bolometry, and are modelled by the predictive transport code ICARUS [12].

SNAP calculates the effective ion charge Z_{eff} assuming neo-classical resistivity, the ohmic power deposition $p_{\text{OH}}(r)$, the total thermal energy W , the energy con-

finement time τ_E , the electron-ion energy exchange and the effective electron heat diffusivity

$$\chi^{\text{eff}}(r) = -\frac{q_e(r)}{n_e(r)\nabla T_e(r)}, \quad (6.1)$$

where q_e is the electron heat flux.

The accuracy of τ_E is $\approx 15\%$, based on the uncertainty in the ECE data (5%), the interferometer (5% after Abel inversion) and the uncertainty in T_i . For $n_e(r)$ and $T_e(r)$ obtained using the Thomson scattering system the error in τ_E is less than 15%.

As an extension of the SNAP code, the error on $\chi_{e,PB}^{\text{eff}}(r)$ is estimated using the error analysis method described by LOPES CARDOZO *et al.* [13] and HOGEWELJ *et al.* [14]. In this method, $T_e(r)$ and $q_e(r)$ are written as the sum of zero order profiles and first order perturbations. The profiles are expanded in Fourier series, of which higher frequencies are truncated, minimizing the sum of the truncation and the statistical error. The error in the heat conductivity is expressed analytically in terms of the errors on q_e and T_e . Typically, the error on $\chi_{e,PB}^{\text{eff}}$ is 20 % at $r/a = 0.5$.

6.4 Results

Additional heating is accomplished by an ECR pulse of maximally 90 ms during the current flat-top. Typically, the line integrated density $\bar{n}_e = (0.5 - 3.5) \times 10^{19} \text{ m}^{-3}$, with a limit on the maximum density due to cut-off of the ECR absorption ($n_{\text{crit}} = 4.5 \times 10^{19} \text{ m}^{-3}$ at 60 GHz for O-mode launched from the low field side).

To find the optimum magnetic field for ECRH absorption, the single-pass transmitted power has been measured with decreasing toroidal field during the ECRH pulse for several values of \bar{n}_e and I_P during the flat top of the discharge. Scanning the magnetic field ($\Delta B_T = 0.2 \text{ T}$) has revealed a pronounced minimum in transmission (down to 15% of the input power) when the resonance is located near the magnetic axis [3].

6.4.1 ECR deposition profile

The nominal input power $P_{\text{ECR}}^{\text{nom}}$ of the ECR launcher has been obtained from calorimetric measurements, and is maximally 180 kW. A small fraction of this input power (15 %) consists of spurious modes that are lost after multiple reflections, i.e. through diagnostic ports or absorbed in the viewing dump of the ECE diagnostic.

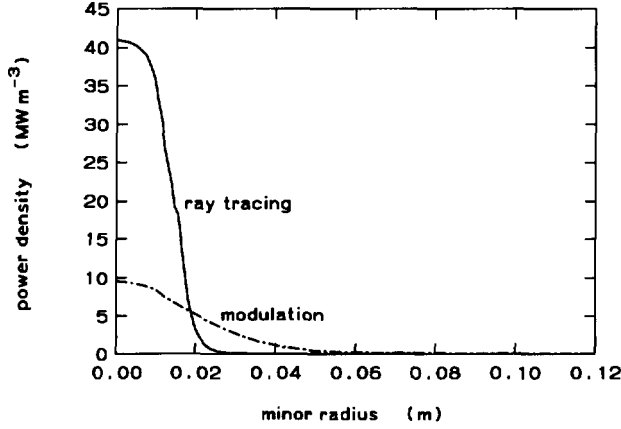


Figure 6.1: ECR power deposition profile $p_{\text{ECR}}(r)$ ray tracing calculations (full line) and from ECR modulation experiments. Plasma conditions are: $P_{\text{ECR}}^{\text{act}} = 150$ kW, $I_p = 125$ kA, $n_e(0) = 2.8 \times 10^{19} \text{ m}^{-3}$, $T_e(0) = 1.1 \text{ keV}$ (time averaged).

Of the remaining ‘actual’ input power ($P_{\text{ECR}}^{\text{act}} = 150$ kW), 124 kW is in the main lobe of the antenna pattern, whereas the remaining power is in side lobes or in X-mode [3]. Single pass absorption leads to a peaked ECR power density profile $p_{\text{ECR}}(r)$. In second pass, some power will be absorbed in a broader deposition region (‘the background’) and a small fraction will be lost through the windows of the vessel.

In this study, $p_{\text{ECR}}(r)$ has been obtained from ray tracing calculations and, for a few discharges from ECR modulation experiments.

Using ray tracing calculations with TORAY [12], only single pass absorption is taken into account. For the plasma conditions at hand, a peaked deposition profile is obtained (e.g. for $T_e(0) = 1.1 \text{ keV}$ and $n_e(0) = 2.8 \times 10^{19} \text{ m}^{-3}$, $p_{\text{ECR}}(0) = 42 \text{ MW/m}^3$, full width at 10 % is 4 cm). The total absorbed power depends on $T_e(r)$.

From ECR modulation studies, $p_{\text{ECR}}(r)$ can be derived by solving the diffusion equation of the temperature perturbation for the first and second Fourier harmonics [16]. According to this analysis, $p_{\text{ECR}}(r)$ can be modelled by the sum of a Gaussian shaped profile and a $1/r$ -dependent background level assuming that reflected power is absorbed at the resonance layer. In sawtooth discharges ($I_p = 125$ kA, $n_e(0) = 2.8 \times 10^{19} \text{ m}^{-3}$, and $T_e(0) = 1.1 \text{ keV}$, time averaged) the total absorbed ECR power is 120 kW. Of this total absorbed power 70 % (84 kW) is contained in the central

Gaussian ($p_{\text{ECR}}(0) = 9.4 \pm 0.9 \text{ MW/m}^3$, full width at 10 % maximum power level 8 cm), and 30 % (36 kW) in the background level.

Figure 6.1 shows $p_{\text{ECR}}(r)$ obtained from ray tracing calculations and ECR modulation experiments. The single pass absorbed power from ray tracing is 15 % higher than the power in the central Gaussian from modulation studies, but close to the one estimated by SMITS *et al.* [3] from transmission measurements. The width of the ray tracing profile is smaller than both the one obtained from modulation studies and from transmission measurements. It must be noticed, however, that ray tracing calculates $p_{\text{ECR}}(r)$ without taking mechanisms into account which could broaden $p_{\text{ECR}}(r)$, like instabilities or sawteeth activity.

In the power balance analysis we have taken $p_{\text{ECR}}(r)$ from ray tracing calculation. In this way dependencies of single pass absorption to $T_e(r)$ and $n_e(r)$ could be included. To account for multiple pass absorption, the remaining power after the single pass is assumed to be absorbed in a $1/r$ -dependent deposition profile.

6.4.2 T_e - and n_e -profiles

Figure 6.2 shows typical T_e - and n_e - profiles for ohmically and ECR heated plasmas. The measurements are taken well after switch-on of the ECRH pulse (≥ 40 ms), to assure a steady-state plasma from the energy balance point of view. It should be noted that full readaption of the current density profile to the resistivity profile occurs with a time constant of 30 to 40 ms. One of the most striking characteristics is the high value of $T_e(0)$ (up to 4 keV) during ECRH. The profiles are sharply peaked with gradients up to 50 keV/m inside $r/a \approx 0.25$. During ECRH the Thomson scattering value of $T_e(0)$ shows a large variability (1-5 keV), but for $r/a \geq 0.1$ there is a good reproducibility in T_e . The scatter in $T_e(0)$ is larger than the experimental error in the Thomson scattering measurement, which has been interpreted as an indication of filamentation of the plasma [29].

Figure 6.2b shows $n_e(r)$ as measured by the interferometer. The Abel inversion of interferometric data is confirmed by the Thomson scattering measurements as long as $n_e(r)$ is peaked. The n_e -profile broadens when ECRH is switched on and the total number of particles increases. Just after switch on (typically after 0.2 - 0.5 ms) a decrease of $n_e(0)$ is observed, which is strongest for plasmas with low \bar{n}_e and low I_P . Thomson scattering measurements just after switch on of ECRH show that the decrease in $n_e(0)$ can be 30 %.

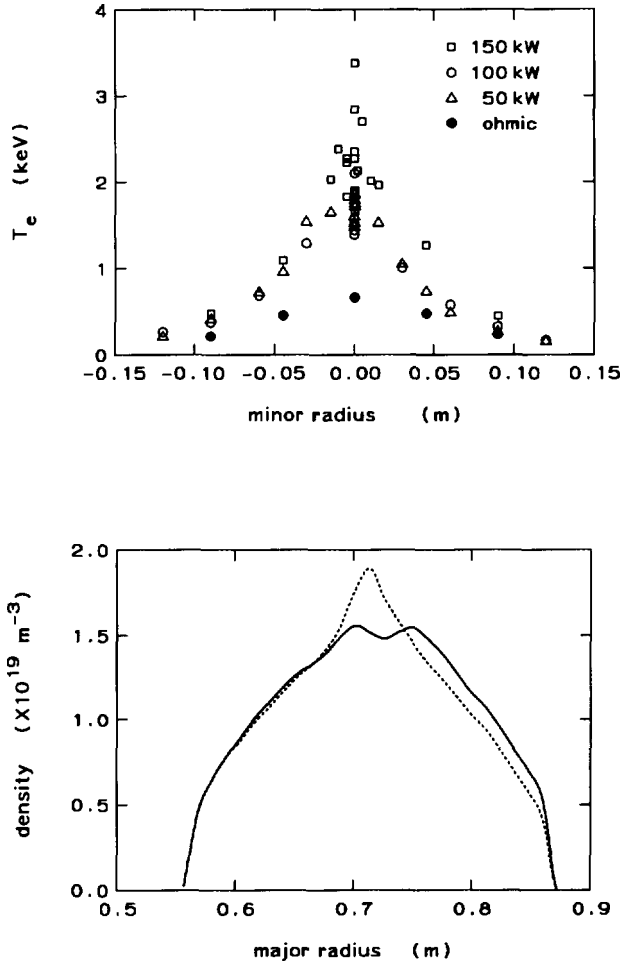


Figure 6.2: The electron temperature (top graph) as a function of minor plasma radius. The profiles are obtained by Thomson scattering in a series of repeated discharges. Plasma conditions are $I_p = 60 \text{ kA}$ and $n_e(0) = 1.5 \times 10^{19} \text{ m}^{-3}$. The ohmic power is 132 kW, decreasing to 47 kW during ECRH ($P_{\text{ECR}}^{\text{act}} = 50, 100$ and 150 kW). The bottom graph shows typical density profiles during ECRH ($P_{\text{ECR}}^{\text{act}} = 150 \text{ kW}$) as measured by the 19-chord interferometer after Abel inversion.

Figure 6.3 shows $T_e(0)$ as a function of $n_e(0)$, both measured by Thomson scattering, for all discharges in the RTP database. In ohmic plasmas, $T_e(0)$ is nearly independent of $n_e(0)$. For $P_{\text{ECR}}^{\text{nom}} = 60$ to 180 kW, $T_e(0)$ decreases when n_e increases from the lowest values obtained to the ECR cut-off density. In low current plasmas ($I_P = 60$ kA), $T_e(0)$ as measured by Thomson scattering is nearly independent of $P_{\text{ECR}}^{\text{nom}}$ over a wide range of intermediate densities.

T_i -measurements were available for a few discharges. Typically $T_i = 0.7 \cdot T_e$ in the ohmic phase; T_i did not change during ECRH within the error bars.

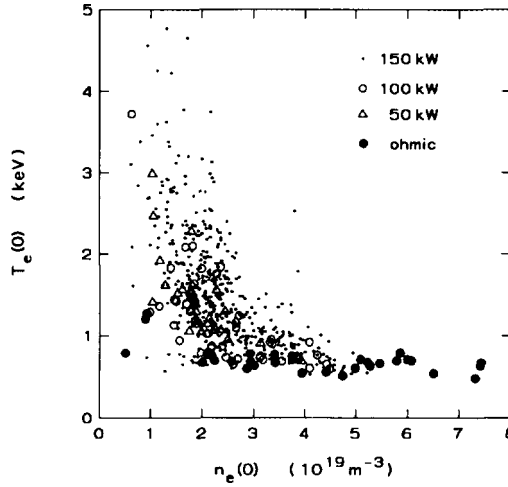


Figure 6.3: $T_e(0)$ versus $n_e(0)$ measured by Thomson scattering. Closed symbols are ohmic discharges. The ECR cut-off density $n_{\text{crit}} = 4.5 \times 10^{19} \text{ m}^{-3}$ at 60 GHz.

6.4.3 Global confinement

The energy confinement time τ_E in ohmically heated plasmas is compared to the Goldston-ohmic scaling law [17]:

$$\tau_E^{\text{Goldston-ohmic}} = 1.0 \times 10^{-21} \bar{n}_e q_a^{0.5} a^{1.04} R^{2.04}, \quad (6.2)$$

where \bar{n}_e is the line averaged density, q_a the edge safety factor, a and R the minor and major radius, respectively. Units are [ms], [10^{19} m^{-3}] and [m]. Figure 6.4a shows

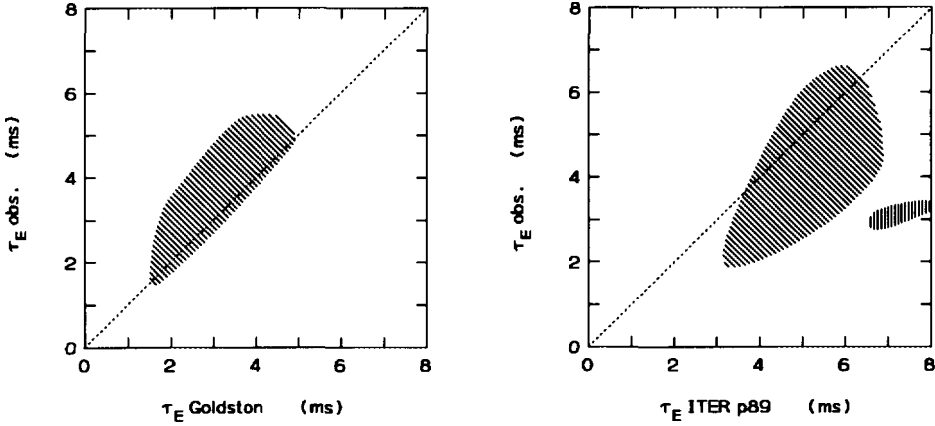


Figure 6.4: The observed energy confinement time compared to scaling laws for ohmic plasmas (Goldston-ohmic scaling) and ECR heated plasmas (ITER89-P additional heating scaling law). Shaded areas indicate measurements over a scan of plasma conditions ($\bar{n}_e = (0.5 - 4) \times 10^{19} \text{ m}^{-3}$, $I_p = 60 - 125 \text{ kA}$) in hydrogen (skew shading) and helium plasmas (vertical shading). Scaling with ion mass as predicted by ITER89-P leads to a separation of shaded areas.

that the agreement between the experimentally observed τ_E (plasma conditions $\bar{n}_e = (0.5 - 4) \times 10^{19} \text{ m}^{-3}$, $I_p = 60 - 125 \text{ kA}$) and the Goldston-ohmic scaling law is good (standard deviation $\sigma^2 = 1.13$).

For ECR heated plasmas, a comparison is made with the ITER89-P scaling [18]:

$$\tau_E^{\text{ITER89-P}} = 48 I_p^{0.85} R^{1.2} a^{0.3} \kappa^{0.5} \bar{n}^{0.1} B_T^{0.2} A_i^{0.5} P_{\text{TOT}}^{-0.5}, \quad (6.3)$$

where κ is the elongation, B_T the toroidal magnetic field, A_i the atomic mass and P_{TOT} the total input power ($P_{\text{OH}} + P_{\text{ECR}}^{\text{nom}}$). Units are [ms], [MA], [m], [10^{20} m^{-3}], [T] and [MW]. Figure 6.4b shows that the calculated confinement from the ITER89-P data base is more optimistic than the observed τ_E . Scaling with ion mass (ITER89-P) is not observed in RTP as shown by the helium discharge data.

Figure 6.5 shows the experimental τ_E as a function of $n_e(0)$ for plasma currents of 60, 90 and 125 kA. In ohmic plasmas τ_E depends linearly on density and saturates

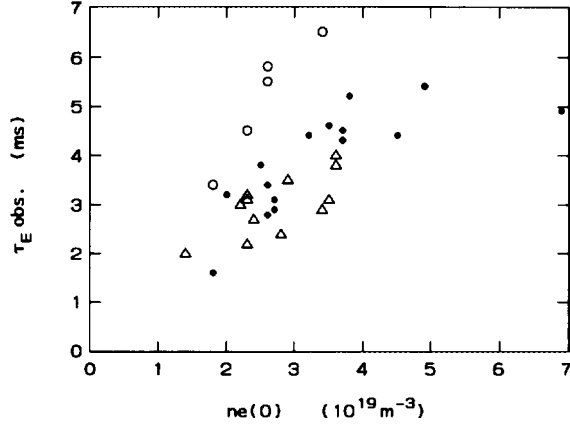


Figure 6.5: The observed τ_E as a function of $n_e(0)$ for $I_p = 60$ kA. The results are for ohmic plasmas (closed circles) and with additional ECR power: $P_{ECR}^{nom} = 60$ (open circles) and 180 kW (open triangles).

for $n_e(0) > 4 \times 10^{19} \text{ m}^{-3}$. In low power ECR heated plasmas τ_E increases; for instance τ_E increases from 1.6 ms (ohmically heated, $P_{OH} = 132$ kW) to 3.4 ms when $P_{ECR}^{nom} = 60$ kW ($P_{OH} = 83$ kW) is applied ($\bar{n}_e = 1.1 \times 10^{19} \text{ m}^{-3}$, $I_p = 60$ kA). Further increase of P_{ECR}^{nom} leads to a decrease in τ_E to 2.0 ms for $P_{ECR}^{nom} = 180$ kW ($P_{OH} = 47$ kW).

For higher \bar{n}_e and higher I_p the improvement of τ_E for low ECRH power is less pronounced. This can be seen in Fig. 6.6 which shows the thermal energy W as a function of total input power P_{TOT} for discharges with $I_p = 60 - 125$ kA and $\bar{n}_e = 1.7 \times 10^{19} \text{ m}^{-3}$. For ECR heated plasmas, W shows a slight increase as function of P_{ECR}^{act} with low dW/dP . For higher \bar{n}_e and higher I_p , dW/dP increases.

6.4.4 LPB analysis

A local power balance analysis has been performed with parameter scans of n_e , I_p and P_{ECR}^{nom} . For $p_{ECR}(r)$, the profile shape is taken as discussed in section 6.4.1. As a typical result, Fig. 6.7 shows $\chi_{e,PB}^{eff}(r)$ for ohmic plasmas and Fig. 6.8 for $P_{ECR}^{act} = 50$ and 150 kW ($I_p = 60$ kA). The shaded areas indicate the error bars, which are obtained as described in section 6.3. The improvement of τ_E during low power ECRH is brought about by a reduction of $\chi_{e,PB}^{eff}$ throughout the plasma. Figure 6.9

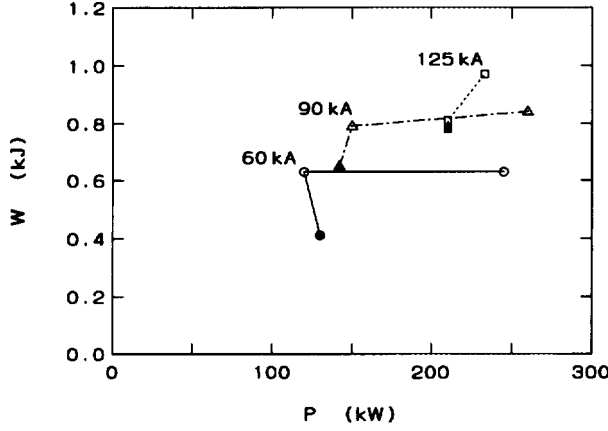


Figure 6.6: Total thermal energy W as a function of total input power P_{TOT} for $I_p = 60, 90$ and 125 kA. To make a comparison between the discharges useful, differences in density have been accounted for by normalizing W to $\bar{n}_e = 1.7 \times 10^{19} \text{ m}^{-3}$ (using regression analysis on the energy confinement, $\tau_E \sim \bar{n}_e^{0.5}$). Ohmic discharges are indicated by closed symbols. Additional ECR power $P_{\text{ECR}}^{\text{nom}} = 60$ and 180 kW (open symbols).

shows q_e (normalized to density) from the LPB analysis as a function of ∇T_e at radial position $r/a = 0.5$. Within this position 90% of the ECR power is deposited. The electron heat flux q_e hardly changes and the reduced $\chi_{e, PB}^{\text{eff}}$ is attributed to an increase in $n_e \nabla T_e$.

From ECRH modulation experiments and sawtooth analysis, an incremental thermal diffusivity can be obtained:

$$\chi_e^{\text{inc}} = -\frac{\partial q_e}{\partial (n_e \nabla T_e)}. \quad (6.4)$$

From both types of experiments, the same value is obtained ($\chi_e^{\text{inc}} = 6 \pm 1.5 \text{ m}^2/\text{s}$ at $r/a = 0.6$, $I_p = 90$ and 125 kA) [16, 19]. From the local power balance analysis with $P_{\text{ECR}}^{\text{act}} = 50$ to 150 kW, we can take $\Delta q_e / \Delta (n_e \nabla T_e)$ as χ_e^{inc} . This leads to a value of $10 \pm 3 \text{ m}^2/\text{s}$, which is close to χ_e^{inc} from the dynamic transport studies.

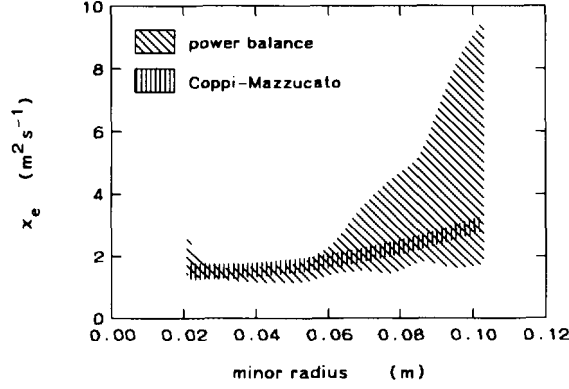


Figure 6.7: χ_e^{eff} from LPB (skew shading) compared to the Coppi-Mazzucato model (vertical shading) for plasma conditions $n_e(0) = 2.0 \times 10^{19} \text{ m}^{-3}$ and $I_p = 90 \text{ kA}$.

6.5 Comparison with model predictions

6.5.1 Profile consistency

In ohmically heated plasmas, the shape of $T_e(r)$ is directly coupled to the ohmic power deposition profile. An expression for χ_e which is consistent with this profile preserving feature for ohmically heated plasmas is given by COPPI and MAZZUCATO [20]:

$$\chi_{e,CM}^{\text{eff}} = 3.64 \times 10^{14} \left(\frac{B_T}{q T_e} \right) [\ln \Lambda Z_{\text{eff}} / n_e^2]^{2/5}, \quad (6.5)$$

where B_T is the toroidal magnetic field, q the safety factor and $\ln \Lambda$ the Coulomb logarithm. Units are $[\text{m}^2/\text{s}]$, $[\text{T}]$, $[\text{keV}]$ and $[\text{m}^{-3}]$.

A comparison of $\chi_{e,CM}^{\text{eff}}$ with $\chi_{e,PB}^{\text{eff}}$ from the power balance is shown in Fig. 6.7 for $I_p = 90 \text{ kA}$. The agreement between model and experiment is good within the error bars. For low and high current plasmas ($I_p = 60$ and 125 kA , respectively) no radiation data was available. However, given the uncertainties in the power balance, the agreement between model and experiment is reasonable within $r/a < 0.8$.

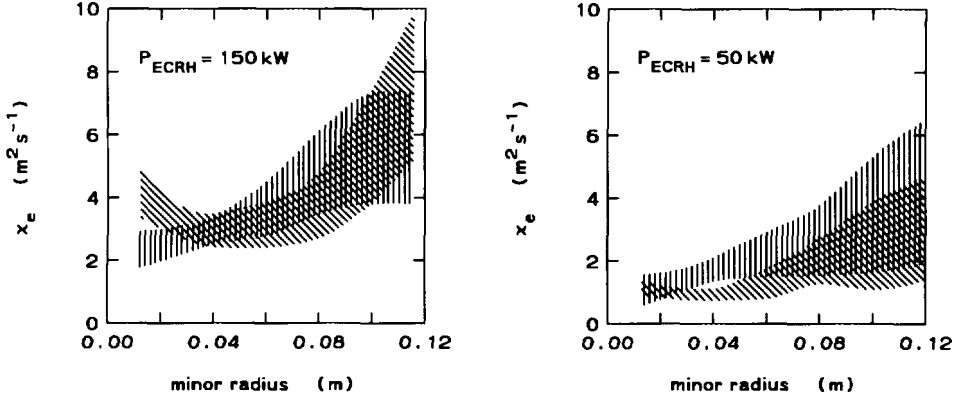


Figure 6.8: $\chi_e^{\text{eff}}(r)$ from steady-state local power balance (skew shading) and from the RLW model (vertical shading). Plasma conditions are: $n_e(0) = 2.5 \times 10^{19} \text{ m}^{-3}$, $I_p = 60 \text{ kA}$, $Z_{\text{eff}} \approx 2 - 3$. Additional ECR power $P_{\text{ECR}}^{\text{act}} = 150 \text{ kW}$ and 50 kW . Shaded areas indicate the statistical error (see section 6.3).

6.5.2 Rebut - Lallia - Watkins model

The Rebut-Lallia-Watkins (RLW) transport model [21], [22], gives an expression for enhanced thermal transport in a turbulent magnetic field. The electron heat flux is given by:

$$q_e = n_e \chi_{e,neo}^{\text{eff}} \nabla T_e + n_e \chi_{e,RL}^{\text{anom}} \left(1 - \frac{(\nabla T_e)_c}{\nabla T_e} \right) \cdot \nabla T_e \cdot H[\nabla T_e - (\nabla T_e)_c] H[\nabla q], \quad (6.6)$$

where

$$\chi_{e,RL}^{\text{anom}} = \alpha \left[\frac{\nabla T_e}{T_e} + \frac{2 \nabla n_e}{n_e} \right] \sqrt{\frac{T_e}{T_i}} \left(1 - \sqrt{\frac{r}{R}} \right) \sqrt{1 + Z_{\text{eff}}} \left(\frac{q^2}{\nabla q B_T R^{1/2}} \right). \quad (6.7)$$

Here $\chi_{e,neo}^{\text{eff}}$ is the neoclassical thermal diffusivity, q the safety factor, r and R are the major and minor radius, respectively, and H is the Heaviside step function. The critical gradient is given by:

$$k_b (\nabla T_e)_c = \frac{\beta}{q} \left(\frac{\eta j B_T^3}{n_e (k_b T_e)^{1/2}} \right)^{1/2}, \quad (6.8)$$

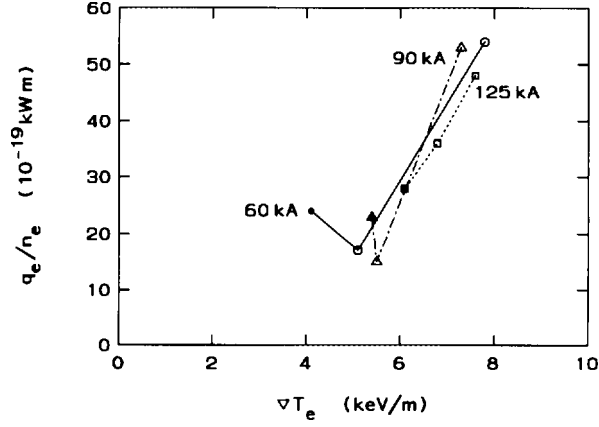


Figure 6.9: *Electron heat flux normalized to local density vs. ∇T_e as calculated from the local power balance analysis at $r/a = 0.5$. Ohmic discharges are indicated by closed symbols. Additional ECR power $P_{\text{ECR}}^{\text{act}} = 50$ and 150 kW (open symbols).*

where k_b is Boltzmann's constant, η is the plasma resistivity, j the current density and B_T the toroidal magnetic field. The dimensionless parameters α and β have been tuned to fit results of confinement studies in JET ($\alpha = 2$ and $\beta = 6$) [23]. The same values have been used in this study. The effective electron thermal diffusivity is given by:

$$\chi_{e,RL}^{\text{eff}} = \chi_{e,neo}^{\text{eff}} + \chi_{e,RL}^{\text{anom}} \left(1 - \frac{(\nabla T_e)_c}{\nabla T_e} \right). \quad (6.9)$$

In ohmic plasmas in RTP the observed ∇T_e is close to the critical gradient, so the RLW model cannot be used. Simulations with a 1-D transport code in which $T_e(r)$ is calculated assuming the RLW model [24] show that the predicted ∇T_e is only marginally larger than the experimentally observed gradient (e.g. at $r/a = 0.5$, $\nabla T_e = 5.7$ keV/m and 5.0 keV/m for the calculated and experimental gradient, respectively).

In ECR heated plasmas, the RLW model predicts a $\chi_{e,RL}^{\text{eff}}$ that is an overestimate of $\chi_{e,PB}^{\text{eff}}$. An explanation for the disagreement could be the large difference between T_e and T_i ($T_e > T_i$) and the very steep ∇T_e in RTP during ECRH. It is suggested [25] that the ratio $[T_e/T_i]^{1/2}$ in the expression for $\chi_{e,RL}^{\text{anom}}$ should be replaced by $[T_e/(T_i + T_e)]^{1/2}$. In the original RLW model developed at JET, the factor $[T_e/T_i]^{1/2}$

was obtained for NBI heated discharges with $T_i > T_e$, thus $[T_e/T_i]^{1/2} \approx [T_e/(T_i + T_e)]^{1/2}$. During ICRH ($T_i \approx T_e$) the factor could not be determined accurately due to uncertainties in the power deposition profiles and the measured $T_i(r)$. For JET the modification alters $\chi_{e,RL}^{anom}$ by typically 10 % during NBI, but becomes significant during ICRH (30 %). At RTP, $T_e = (2 - 4) \cdot T_i$ and the modification changes $\chi_{e,RL}^{anom}$ by typically 55 %.

Figure 6.8 shows $\chi_{e,RL}^{eff}(r)$ for the ECR heated plasmas, as predicted by the RLW model using the modified expression for $\chi_{e,RL}^{anom}$. The error on $\chi_{e,RL}^{eff}$ is dominated by the uncertainty in ∇T_e and $\nabla q/q$ (indicated by the shaded area in Fig. 6.8). Compared to the local power balance analysis there is correspondence within the error bars outside $r/a > 0.3$. In the region with the very steep ∇T_e , $\chi_{e,RL}^{eff}$ slightly overestimates $\chi_{e,PB}^{eff}$. It must be noted, however, that no systematical errors have been taken into account, which could affect $\chi_{e,PB}^{eff}$ especially in the steep gradient region, where the statistical error is rather small.

6.6 Discussion and Conclusions

In the RTP tokamak ohmic target plasmas have an energy confinement time in agreement with the Goldston-ohmic scaling law (Fig. 6.4). For low n_e , τ_E depends linearly on density. The saturation at higher densities (Fig. 6.5) is a common observation, which has first been reported in Alcator [26], [27] and ISX-A [28]. The local power balance analysis in ohmically heated plasmas shows that $\chi_{e,PB}^{eff}$ is close to the predicted $\chi_{e,CM}^{eff}$ of the Coppi-Mazzucato model.

The good absorption of ECR power is demonstrated by the minimum in the measured transmitted ECR power and the very peaked $T_e(r)$ within $r/a = 0.25$ (Fig. 6.2). Comparison with the Rebut-Lallia-Watkins model shows that $\chi_{e,RL}^{eff}$ is too optimistic. The modified expression for $\chi_{e,RL}^{eff}$ successfully describes $\chi_{e,PB}^{eff}$ in these extreme plasma conditions for $r/a > 0.2$ for the $P_{ECR}^{act} = 150$ kW case.

Improved confinement is observed when only 60 kW ECR power is applied to an ohmic target plasma with low current ($I_p = 60$ kA) and low density ($\bar{n}_e \leq 1.8 \times 10^{19} \text{ m}^{-3}$). For these plasma conditions, the decrease in ohmic power is more than the additional ECR power, leading to a net decrease of total input power during ECRH. With only a slight increase in thermal energy, τ_E improves by a factor 2 (for $\bar{n}_e = 1.1 \times 10^{19} \text{ m}^{-3}$). For higher \bar{n}_e the improvement is still significant but less pronounced (Fig. 6.6, $\bar{n}_e = 1.7 \times 10^{19} \text{ m}^{-3}$). The improvement is caused by a decrease of $\chi_{e,PB}^{eff}(r)$ throughout the plasma; the reduction of thermal transport cannot be

attributed to a local 'transport barrier'. Observations of improved confinement with low power ECRH are reported by RIVIERE *et al.* [30] (low density plasmas) and W7-AS [31] (low power ECRH compared to high power ECRH). At ASDEX improved confinement is observed during lower hybrid current drive [32].

The improved confinement during low power ECRH is brought about by an increase of $n_e \nabla T_e$ by more than a factor two, while the electron heat flux q_e hardly changes. One mechanism could be a reduction of the thermal diffusivity during ECRH. However, high values of χ_e^{inc} found *both* in ohmic and ECR heated discharges indicate that the diffusive component of transport is not affected [33]. This could suggest that non-diffusive processes, like inward electron heat convection, are induced by ECRH. Inward electron heat transport has been observed in the DIII-D experiment within the deposition radius in case of ECR heating [34]. Note that also in the case of RTP with central heating, a large fraction of ECR power is deposited off axis. The error bars on q_e , however, do not allow a conclusive answer yet. More dedicated experiments are needed to identify the responsible mechanism for the improved confinement.

Acknowledgements

The authors are indebted to Dr. D. Boucher (JET) for the discussions about the Rebut-Lallia model and to Dr. M.C. Zarnstorff (Princeton) for making the SNAP code available. This work was performed under the Euratom-FOM association agreement with financial support from NWO and Euratom.

References

- [1] ALIKAEV V.V. *et al.* (1987) *Sov. J. Plasma Phys.* **13**, 1.
ASHRAF M. *et al.* (1988) Proc. 12th Int. Conf. on Plasma Phys. and Contr. Nucl. Fusion Res., Nice, Vol. 1, p.541.
HOSHINO K. *et al.* (1992) *Phys. Rev. Lett.* **69**, 2208.
HSUAN H. *et al.* (1984) Proc. 4th Int. Symp. on Heating in Toroidal Plasmas, Rome, p.809.
PIETRZYK Z.A. *et al.* (1992) submitted to *Nucl. Fusion* August 1992.
SING D.C. *et al.* (1990) Proc. 13th IAEA Conf. on Plasma Physics and Contr. Nucl. Fusion Res., Washington, Vol. 1, p.757.
STALLARD B.W. *et al.* (1990) *Nucl. Fusion* **30**, 2235.
TFR-GROUP and FOM-ECRH TEAM (1988) *Nucl. Fusion* **28**, 1995.
- [2] SCHÜLLER F.C. *et al.* (1991) Proc. 18th Eur. Conf. on Contr. Fusion and Plasma Phys., Berlin, Part I, p.121.
- [3] SMITS F.M.A. (1991a) Thesis Rijksuniversiteit Utrecht 17-12-1991.
- [4] SMITS F.M.A. *et al.* (1991b) Proc. 18th Eur. Conf. on Contr. Fusion and Plasma Phys., Berlin, Part IV, p.217.
- [5] BARTH C.J. (1988) *Appl. Opt.* **27**, 2981.
- [6] VERRECK M. *et al.* (1991) Proc. 18th Eur. Conf. on Contr. Fusion and Plasma Phys., Berlin, Part IV, p.341.
- [7] VAN LAMMEREN A.C.A.P. *et al.* (1991) Proc. 18th Eur. Conf. on Contr. Fusion and Plasma Phys., Berlin, Part II, p.73.
- [8] SCHOKKER B.C. *et al.* (1991) Proc. 18th Eur. Conf. on Contr. Fusion and Plasma Phys., Berlin, Part I, p.125.
- [9] DA CRUZ D.F., MEIJER J.H. and DONNÉ A.J.H. (1992) *Rev. Sci. Instrum.* **63**, 5026.
- [10] DA CRUZ D.F. and DONNÉ A.J.H. (1990) *Rev. Sci. Instrum.* **61**, 3067.
- [11] TOWNER H.H. and GOLDSTON R.J. (1984) *Bull. Am. Phys. Soc.* **29**, 1305.
- [12] KRITZ A.H. *et al.* (1982) Proc. 3rd Int. Symp. on Heating in Toroidal Plasmas, Grenoble (France), 22-26 March Vol. II p.707
WESTERHOF E. (1989) Rijnhuizen Report 89-183, The Netherlands.
- [13] LOPES CARDOZO N.J., HOGWEIJ G.M.D. and HORDÓSY G. (1989) *Plasma Physics and Controlled Fusion* **31**, 471.
- [14] HOGWEIJ G.M.D., HORDÓSY G. and LOPES CARDOZO N.J. (1990) *Comput. Phys. Commun.* **59**, 245.
- [15] SCHÜLLER F.C. *et al.* (1992) Proc. 14th Int. Conf. on Plasma Phys. and Contr. Nucl. Fusion Res., Würzburg.

- [16] GORINI G. *et al.* (1992) submitted to *Phys. Rev. Lett.*
- [17] GOLDSTON R. (1984) *Plasma Physics and Controlled Fusion* **25**, 65.
- [18] YUSHMANOV P.N. *et al.* (1990) *Nucl. Fusion* **30**, 1999.
- [19] HOGEWELJ G.M.D., LOPES CARDOZO N.J., PETERS M. and THE RTP TEAM (1992) Proc. 19th Eur. Conf. on Contr. Fusion and Plasma Phys., Innsbruck, Part I, p.75.
- [20] COPPI B. and MAZZUCATO E. (1979) *Phys. Lett.* **71A**, 337.
- [21] REBUT P.H. *et al.* (1987) Proc. 14th Eur. Conf. on Contr. Fusion and Plasma Phys., Madrid, Part I, p.172.
- [22] REBUT P.H. *et al.* (1988) Proc. 12th Int. Conf. on Plasma Phys. and Contr. Nucl. Fusion Res., Nice, Vol. 2, p.191.
- [23] LALLIA P.P. and REBUT P.H. (1989) Workshop on the New Phase for JET: the Pumped Divertor Proposal, September 25-26 p. 184.
- [24] BOUCHER D. (1992a) Thesis l'École Polytechnique, Paris, September 1992.
- [25] BOUCHER D. (1992b) *private communication*.
- [26] SCHRAM D.C. and SCHÜLLER F.C. (1980) *Physica* **100C**, 371.
- [27] GONDHALEKAR A. *et al.* (1978) Proc. 7th IAEA Int. Conf., Innsbruck 1978, Vol.1, IAEA, Vienna (1979), p.199.
- [28] MURAKAMI M. *et al.* (1978) Proc. 7th IAEA Int. Conf., Innsbruck 1978, Vol.1, IAEA, Vienna (1979) p.269.
- [29] LOPES CARDOZO N.J. and SCHÜLLER F.C. (1992) *Plasma Physics and Controlled Fusion* **34**, 1939.
- [30] RIVIERE A.C. (1986) *Plasma Phys. and Contr. Fusion* **28**, 9A 1263
- [31] WELLER A. *et al.* (1991) *Plasma Physics and Controlled Fusion* **33**, 1559.
- [32] SÖLDNER *et al.* (1990) Plasma Physics and Controlled Nucl. Fusion Research (Proc. 13th Int. Conf. Washington DC, 1990) **1**, Vienna (1991), p.613
- [33] LOPES CARDOZO N.J. *et al.* (1992) Proc. 14th Int. Conf. on Plasma Phys. and Contr. Nucl. Fusion Res., Würzburg.
- [34] LUCE T.C., PETTY C.C. and DE HAAS J.C.M. (1992) *Phys. Rev. Lett.* **68**, 52.

Chapter 7

Improved confinement during ECRH

In this chapter the transition from the ohmic target plasma to the improved confinement regime during low power ECRH is investigated. The basic experimental technique is to apply square wave modulated ECRH. The modulation frequency f_{mod} is chosen well in excess of the inverse confinement time, so that a quasi steady state is reached with only small temperature perturbations. Two experiments are reported: a scan of f_{mod} at constant effective power, and a scan of the effective power achieved by scanning the duty cycle of the modulation. The frequency scan shows that τ_{Ee} is an increasing function of f_{mod} , with best confinement achieved with CW ECRH. A suprathreshold electron population of 5 – 10 keV, created by ECRH, may be associated with the improvement of confinement.

7.1 Introduction

A common observation in various devices is that on-axis Electron Cyclotron Resonance Heating (ECRH) leads to strongly peaked $T_e(r)$ and, at high ECRH power, to a degradation of energy confinement [1]. In the RTP tokamak, similar observations are made with high power, centrally deposited ECRH. Interestingly, observations with low power ECRH showed an improvement of confinement, compared to the ohmic target plasma, by more than a factor two [2]. Plasma conditions were $q_a = 6.8$, $n_e(0) = 2.2 \times 10^{19} \text{ m}^{-3}$, $P_{\text{ECRH}} = 60 \text{ kW}$ (LFS O-mode) and $P_{\text{OH}} = 50 \text{ kW}$. Increasing P_{ECRH} from 60 to 180 kW showed an increase of the thermal energy W by less than 10%, corresponding to a degradation of confinement of $\tau_E = 5.4$ to 2.6 ms.

In this paper the transition from the ohmic target plasma to the improved confinement regime is investigated. Two specific questions are addressed: (i) is there an ECRH power threshold for the improved confined regime, and (ii) is the improvement induced by ECRH and what is the typical time scale involved. To investigate the presence of a threshold, an ECRH power scan is done. Since P_{ECRH} could not be reduced below 60 kW in continuous (CW) gyrotron operation, a further reduction of the effective power is achieved by square wave modulation. If the frequency of the modulation is large compared to the inverse energy confinement time, the T_e variations are small and steady state confinement analysis can be done by integrating over a few modulation periods.

In another experiment, the frequency of the modulation is scanned at constant effective input power, in an attempt to estimate the typical time scale associated to the mechanism that causes the improvement of confinement.

7.2 ECRH Power scan

Square wave ECRH modulation is performed by switching the anode current of the gyrotron on and off. In this study the modulation is applied at a frequency of 0.8 kHz, which is fast compared to the inverse energy confinement time ($\tau_E = 3 - 5 \text{ ms}$). The rise and decay time of the power step is $\sim 15 \mu\text{s}$.

By varying the duty cycle, the effective ECRH power is scanned between 0 and 180 kW. As filling gas helium is used with $n_e(0) = (2.5 \pm 0.2) \times 10^{19} \text{ m}^{-3}$, $B_T = 2.22 \text{ T}$ and $q_a = 6.8$ (non-sawtooth in the ohmic phase). The time averaged analysis is done 40 ms after the start of the ECRH modulation. In this semi-steady state the

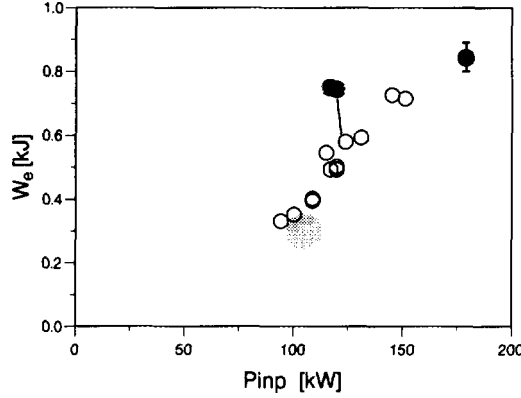


Figure 7.1: *Electron thermal energy vs. the effective input power (ohmic + ECRH as used in the local power balance analysis). The shaded area indicates the position of the ohmic target plasmas in RTP. CW: (solid symbols) 60 and 180 kW respectively; Modulated: (open symbols) $f = 0.8$ kHz, 180 kW, duty cycle = 10 – 70%. Two measurements with effectively the same ECRH input power are connected by the line.*

T_e fluctuations due to the fast modulation ($\Delta T_e(0)/T_e \leq 10\%$) have been averaged in the analysis over 4 modulation periods.

Figure 7.1 shows the electron thermal energy W_e as function of the effective input power P_{inp} . The energy is obtained from $T_e(r)$ as measured by heterodyne ECE and $n_e(r)$ from the interferometer. In the CW case, also TV Thomson scattering data are available, which show a $T_e(r)$ consistent with ECE, apart from fine structures which are beyond the ECE resolution ($\Delta r/a[\text{ECE}] \sim 0.1$; $\Delta r/a[\text{TVTS}] \sim 0.01$). The increase of W_e due to ECRH is consistent with changes in $\beta_p + l_i/2$ deduced from the vertical magnetic field. An increase of P_{ECRH} from 0 to 180 kW results in a linear increase in W_e , without any threshold or sharp transition. Application of $P_{\text{ECRH}} = 60$ kW continuously shows a significant increase in W_e . In Fig. 7.1 two conditions can be found that have effectively the same ECRH input power (CW: $P_{\text{ECRH}} = 60$ kW; modulated: $P_{\text{ECRH}} = 180$ kW, duty cycle = 33%). In the CW case, W_e is 35% higher than with modulated ECRH. These two conditions will now be discussed in more detail.

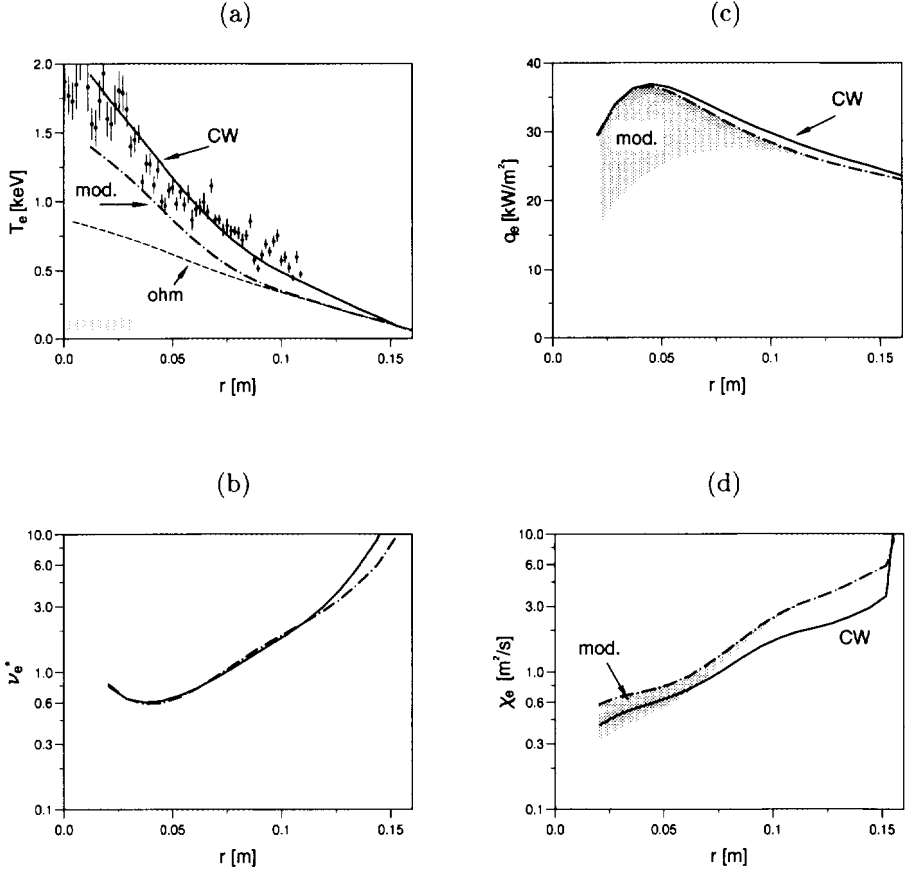


Figure 7.2: (a): $T_e(r)$ measured by heterodyne ECE for the ohmic case, and modulated/CW ECRH with effectively the same input power. In the modulated case ($f_{\text{mod}} = 0.8$ kHz) $T_e(r)$ is averaged over 4 modulation periods. The Thomson scattering measurement in the CW case is indicated by the solid symbols with error bars. The shaded area indicates the FWHM of the CW ECRH deposition profile. (b): Electron collisionality ν_e^* for the two compared cases. The difference in T_e is balanced by a difference in Z_{eff} , such that the same $\nu_e^*(r)$ is obtained. (c): Local electron heat flux q_e for modulated and CW ECRH with effectively the same input power. The shaded area indicates the uncertainty in q_e due to differences in $p_{\text{ECRH}}(r)$ (FWHM= 6 – 16 cm). (d): Electron thermal diffusivity χ_e from the local power balance analysis. The shaded area indicates the uncertainty in χ_e due to differences in $p_{\text{ECRH}}(r)$ (FWHM= 6 – 16 cm).

The different values of W_e are caused by differences in $T_e(r)$, as shown in Fig. 7.2a. For CW ECRH, T_e is higher over the whole plasma radius, also outside the ECRH deposition region (FWHM $\simeq 6$ cm). Ray-tracing calculations show that due to the difference in $T_e(r)$ the difference in single-pass absorbed power is only 6% of the nominal input power, assuming that the electron velocity distribution function is the same for modulated and CW ECRH. It is well possible, however, that the population of suprathermal electrons is smaller during modulated ECRH, which will decrease the efficiency of single-pass absorption. After multiple reflections, the power will be absorbed with a much broader deposition profile. In the local power balance analysis, we have taken for the time averaged $p_{\text{ECRH}}(r)$ during modulation two extreme cases: (i) $p_{\text{ECRH}}(r)$ equal to the CW deposition profile (Gaussian with FWHM = 6 cm), and (ii) a very broad $p_{\text{ECRH}}(r)$ with FWHM = 16 cm. Figure 7.2d shows the thermal diffusivity χ_e , as calculated by SNAP [3]. The shaded area indicates the two limits of $p_{\text{ECRH}}(r)$. For equal deposition ECRH profiles, χ_e is lower in the CW case over the whole plasma radius. In the other limit for $p_{\text{ECRH}}(r)$, χ_e is still lower outside $\rho = 0.5$.

For the two compared cases in Fig. 7.1, the differences in $T_e(r)$ lead to differences in ohmic input power. The figure shows, however, that for both cases the total input power is comparable. This is caused by a difference in Z_{eff} , due to a small oxygen leakage which occurred at the start of the experimental session. Z_{eff} is 6.8 in the CW and 3.5 in the modulated case. As a result, the same total net heat flux is obtained, see Fig. 7.2c. Interestingly, this also holds for the electron collisionality (Fig. 7.2b). Thus, the reduction of χ_e is not accompanied by changes in collisionality.

In conclusion, two plasma conditions are compared with the same effective input power, but applied modulated and CW. A difference of 35% in $\chi_e(r)$ is obtained, outside $\rho = 0.5$. In the next section this discrepancy is further investigated by scanning the modulation frequency at constant duty cycle. This can reveal the typical time scale of the processes associated with the improvement of confinement.

7.3 ECRH Frequency scan

At fixed ECRH power and duty cycle (180 kW, 33%) a frequency scan was performed from 0.8 – 4.2 kHz. For the higher modulation frequencies, no time averaged steady state could be reached, since the number of modulation cycles is limited by the gyrotron idling time. In these cases, the time dependent response of the plasma can be deduced from the change in $\beta_p + I_i/2$ as obtained from the vertical magnetic field

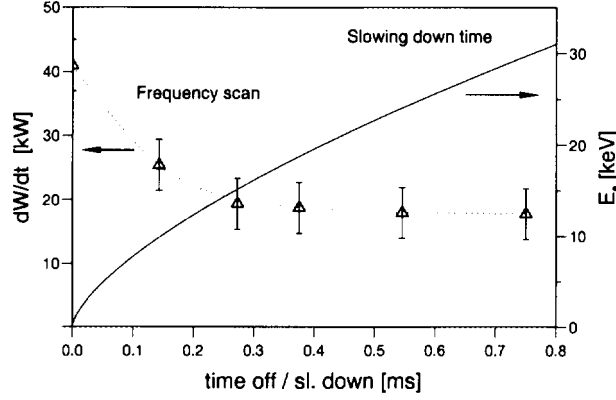


Figure 7.3: *Frequency scan: (triangles) time derivative of W (measured by the vertical magnetic field) at switch-on of fast modulated ECRH ($f = 0.8 - 4.2$ kHz). Slowing-down time: (full line) of suprathermal electrons with respect to the thermal bulk. The abscissa denotes the 'off'-time of the gyrotron, which determines whether a suprathermal population can be sustained. Plasma conditions are $n_e(0) = 2.5 \times 10^{19} \text{ m}^{-3}$ and $Z_{\text{eff}} = 3.5$.*

B_z necessary to keep the plasma position unchanged.

Fixed plasma conditions in the frequency scan experiment were $n_e(0) = (2.5 \pm 0.2) \times 10^{19} \text{ m}^{-3}$, $B_T = 2.22 \text{ T}$ and $q_a = 6.8$. Figure 7.3 shows dW/dt as function of the time that the gyrotron is switched-off during the modulation. For $f_{\text{mod}} < 1.2$ kHz, dW/dt is obtained by a fit of the B_z signal with two exponential curves with a fast decay time $\tau_1 = 1.0 - 2.5$ ms to follow dW/dt , and a longer time ($\tau_2 = 20 - 40$ ms) that corresponds to the current diffusion time at which l_i changes. For $f_{\text{mod}} > 1.2$ kHz, the increase in B_z was taken by a linear fit in the first 2.5 ms after switch-on.

As is shown in Fig. 7.3, for $f_{\text{mod}} > 2$ kHz dW/dt increases and approaches the CW case. This occurs with a characteristic $1/e$ -time of $\tau = 0.12$ ms.

It is well possible that differences between modulated and CW ECRH can be explained by differences in a suprathermal component of the electron distribution function. Such a component can only be sustained if the 'off-time' of the modulation is sufficiently short compared by the slowing down time which is given by [4]

$$\tau^{-1} = 5.06 \frac{\gamma n_e}{(\gamma^2 - 1)^{3/2}} \frac{\ln \Lambda}{17} (2 + Z_{\text{eff}}) \quad (7.1)$$

in units $[s^{-1}]$, $[10^{19} m^{-3}]$. Here $E = (\gamma - 1)E_0$ is the energy of the electron with rest mass E_0 . Equating the characteristic time $\tau = 0.12$ ms to the slowing-down time of suprathermal electrons, fixes the energy of a possible population of such electrons associated to the improved confinement at $E = 5$ to 10 keV. This agrees well with theoretical calculations showing that the ECRH absorption is largest when the resonant electrons have an energy of 2.5 times the thermal energy [5].

7.4 Discussion and Conclusion

Summarizing, improvement of confinement, as observed in RTP when low power CW ECRH is applied, is not observed when the same effective power is applied in a modulated way at a modulation period short compared to the energy confinement time. The ECRH power scan at fixed modulation frequency shows a linear increase in W_e , without any threshold or sharp transition to the improved confinement regime. The modulation frequency scan shows that the difference between CW and modulated ECRH decreases at increasing modulation frequency. Two cases that were analyzed with the same $\nu_e^*(r)$, show that the reduction of χ_e is not caused by changes in collisionality.

The improvement of confinement is either related to a reduced χ_e or to a non-diffusive transport component, like an inward heat flux. A reduction of χ_e can be caused by a lower electrostatic or magnetic turbulence level during ECRH. Although no experimental observations of reduced turbulence during ECRH are reported (even the opposite might be expected since a suprathermal population is a source of free energy that generally increases the turbulence level), observation of global changes induced by local sources have been observed [6, 7]. Concerning non-diffusive transport, convection or not- ∇T_e -driven thermal transport could be important. Experiments at DIII-D [8] show that during off-axis ECRH a peaked $T_e(r)$ is observed which is sustained by an inward electron heat flux. In the q_e vs. $n_e \nabla T_e$ diagram the reduction of thermal transport is reflected by an increased offset.

From the frequency scan it is concluded that with CW ECRH a suprathermal population of 5–10 keV can be sustained, which is absent with modulated ECRH. It is important to note that *it is not the population itself that contributes to the thermal W_e and τ_{Ee}* , since the measured $T_e(r)$ really is the thermal bulk temperature and, moreover, the slowing down time is short compared to τ_{Ee} . If ECE was dominated by suprathermal radiation ($I_{rad} \sim T^2$), $T_e(r)$ would be significantly different from the Thomson scattering measurement, which is not sensitive to the suprathermal

population.

If a suprathermal population is not sustained during ECRH with low f_{mod} , the ECRH single-pass absorption will be less efficient and more power will be deposited, after reflections, in the background, hence $p_{\text{ECRH}}(r)$ can be broader than in the CW case. We have demonstrated, however, that even in case that $p_{\text{ECR}}(r)$ is extremely broad, $\chi_e(r)$ is still significantly lower outside $\rho = 0.5$.

The reduction of χ_e could be caused by the created suprathermal electron population. The question remains, however, what the mechanism is and why the improvement occurs also outside the ECRH deposition region. The overall decrease of χ_e could be caused by changes in the current density profile in the ECRH region. This causes changes in the q -profile and, thus, the magnetic shear. It is known [9] that local changes in $j(r)$ can reduce χ_e . However, the time scale at which $j(r)$ can adapt is much longer than the typical time of 0.12 ms, as was found in the frequency modulation scan.

Summarizing, this study shows a difference in confinement for CW and modulated ECRH. From the time scale involved it is concluded that a non-thermal population as induced by ECRH could be responsible for the improvement. A modification of $j(r)$ changes $q(r)$, which could explain why the reduction of χ_e occurs over the full plasma radius, also outside the ECRH deposition region. Future experiments, like off-axis modulated ECRH, might further reveal the mechanism associated to the improvement of confinement.

References

- [1] ALIKAEV V.V. *et al.* (1987) *Sov. J. Plasma Phys.* **13**, 1.
SING D.C. *et al.* (1990) Proc. 13th IAEA Conf. on Plasma Physics and Contr. Nucl. Fusion Res., Washington, Vol. 1, p.757.
TFR-GROUP and FOM-ECRH TEAM (1988) *Nucl. Fusion* **28**, 1995.
- [2] KONINGS J.A., HOGWEIJ G.M.D., LOPES CARDOZO N.J., OOMENS A.A.M., SCHÜLLER F.C. and the RTP team (1994) *Plasma Physics and Controlled Fusion* **36**, 45.
- [3] TOWNER H.H. and GOLDSTON R.J. (1984) *Bull. Am. Phys. Soc.* **29**, 1305.
- [4] KNOEPFEL H. and SPONG D.A. (1979) *Nucl. Fusion* **19** 785.
- [5] FIDONE I., MEYER R.L. and GRANATA G. (1983) *Phys. Fluids* **26** 3292.
- [6] GENTLE K. (1994) Proc. 21th Conf. on Controlled Fusion and Plasma Physics, Montpellier.
- [7] STROTH U. *et al.* (1993) Proc. Workshop on Local Transport Studies in Fusion Plasmas, Varenna, Vol. ISPP-14, Soc. Italiana di Fisica, Bologna 161.
- [8] LUCE T.C., PETTY C.C. and DE HAAS J.C.M. (1992) *Phys. Rev. Lett.* **68** 52.
- [9] GOLDSTON R.J. *et al.* (1994) Invited presentation 21th Conf. on Controlled Fusion and Plasma Physics, Montpellier; to be published in special issue of *Plasma Physics and Controlled Fusion*.

**NEXT PAGE(S)
left BLANK**

Chapter 8

Controlled contamination: the Z_{eff} scan

*Transport analysis is performed in a series of discharges where Z_{eff} was varied by using mixtures of helium and neon as filling gas. Z_{eff} was scanned over the range 5.1 – 9.5 ($q_a = 6.8$, $n_e(0) = (2.0 - 2.8) \times 10^{19} \text{ m}^{-3}$). As a reference for clean conditions, deuterium was used, in which also a density scan was performed. For increasing Z_{eff} , the following observations were made: an increasing loop voltage and $T_e(0)$, a slight broadening of $T_e(r)$ and a moderate increase of radiation losses. Regression analysis shows only a very weak dependence of χ_e on Z_{eff} both in ohmic and ECR heated discharges. The scaling of χ_e with n_e and Z_{eff} is consistent with the scaling of the global τ_{Ee} , both showing an absence of scaling with Z_{eff} . Scaling with the collisionality shows $\chi_e \sim \nu_e^{*0.4}$ in ohmic discharges. A comparison is made to the predictions of transport models. Although some correlation is found, there is no model that predicts the observed χ_e both in ohmic plasmas and during ECRH.*

8.1 Introduction

The understanding, let alone control, of anomalous transport in tokamak plasmas is still an unresolved issue. It is currently believed that neoclassical (collision induced) transport is enhanced by electrostatic and/or magnetic fluctuations. A large number of transport theories have been developed, of which none is capable of predicting the observed transport under all various experimental conditions.

The large number of viable models can only be reduced by extensive comparison with experimental data. To check specific parametric dependencies, preferably an experimental dataset should be used in which only one parameter is scanned. This is not a trivial task, since (masked) coupling between plasma parameters might be present.

In RTP, an experiment was performed in which the effective ion charge (Z_{eff}) was scanned, without changing other parameters like electron temperature (T_e) and density (n_e) too seriously. Comparison between the measured Z_{eff} dependence of local transport coefficients and the Z_{eff} dependence predicted by the various transport models could eliminate some of those models as a viable explanation for anomalous transport. Although RTP is a small machine ($\beta \sim 0.3$, $\nu_e^* \simeq 1$), this type of experiment is relevant to larger devices. Anomalous transport is observed in both large and smaller tokamaks with the same dependence on parameters. The extensive number of diagnostics available at RTP allows electron transport studies with high spatial and temporal resolution.

Experimental data on the dependence of the energy confinement and the local thermal diffusivity χ_e on Z_{eff} is scarce [1, 2]. In PLT [5] τ_E increases in higher Z plasmas (no regression analysis given), whereas in ISX-A [6] a decrease of τ_E is observed after impurity injection. In TFR [7] a decrease of confinement is observed in the ‘iron dominated’ regime. In JET [3] the Z_{eff} dependence was studied for the *incremental* diffusivity; the scaling $\chi_e^{\text{inc}} \sim Z_{\text{eff}}^{0.5}$ was found in limiter discharges.

This chapter reports on the experiment in RTP where Z_{eff} was scanned, using a mixture of helium (${}^4_2\text{He}$) and neon (${}^{20}_{10}\text{Ne}$) as filling gas. By changing their relative fraction Z_{eff} was varied while other parameters (like q_a , n_e) were kept constant. As an extension of the Z_{eff} scan, transport studies in deuterium (${}^2_1\text{D}$) were performed. This allowed discharges at $Z_{\text{eff}} = 1.5$, while the mass/charge ratio remains the same as for helium and neon. The Z_{eff} scan was performed for $q_a = 6.8$ and densities $n_e(0) = (2.0 - 2.8) \times 10^{19} \text{ m}^{-3}$, for both ohmically and ECR heated plasmas.

This chapter reports on both the Z_{eff} experiment and the comparison with trans-

port models. In Section 8.2 the experimental observations of deuterium, helium and neon plasmas are described. Then, in Section 8.3, the results of confinement studies and local power balance analysis are presented. In Section 8.4 a comparison is made with the various transport models that have been discussed in Chapter 4 of this thesis. The implications of the results for anomalous transport are discussed in the final section.

8.2 Experimental observations

Machine operation and plasma conditions: Controlled contamination of plasmas was obtained using a mixture of helium and neon as filling gas, *before* breakdown. By varying the relative pressure between the two gasses, Z_{eff} was scanned. In high current plasmas ($q_a = 3.4$) density control was difficult, and often disruptions occurred. Therefore, the dataset analyzed is limited to $q_a = 6.8$. In clean conditions typically $\tau_E = 4$ ms, current flat top $\simeq 140$ ms, $T_e(0) = 650$ eV (during ECR heating $T_e(0) = 1.5 - 3$ keV). The Z_{eff} scan reported here consists of 27 good discharges measured on the same day. Transport studies in deuterium plasmas were done on another day, just after boronization [4] of the vessel. A density scan was performed with $n_e(0) = (2.1 - 5.5) \times 10^{19} \text{ m}^{-3}$ for $q_a = 6.8$ ($Z_{\text{eff}} = 1.4 - 2.4$).

Figure 8.1 shows the obtained Z_{eff} as function of the relative fraction of neon in the plasma. Z_{eff} is calculated from neoclassical resistivity, assuming that $Z_{\text{eff}}(r)$ is constant over the plasma cross-section. This assumption is empirically justified in other devices by comparing the experimental electric resistivity with theoretical predictions. In Fig. 8.1 the full line indicates the expected volume averaged value of Z_{eff} in helium-neon discharges assuming $n_{\text{Ne}}/n_{\text{He}} = \text{constant}$, i.e. a flat Z_{eff} -profile. In the calculation the averaged ionization states in coronal equilibrium are used, given the ohmic $T_e(r)$ [10]. Coronal equilibrium might not be reached for the higher ionization states of Ne. The ionization rate of Ne^{8+} is $S \simeq 6 \times 10^{-18} \text{ [m}^3/\text{s]}$ and for Ne^{9+} $S \simeq 1 \times 10^{-18} \text{ [m}^3/\text{s]}$ at $T_e = 0.5$ keV [9]. The time needed to reach equilibrium is $(n_e \cdot S)^{-1} \simeq 5$ ms for Ne^{8+} and $\simeq 30$ ms for Ne^{9+} , respectively, where transport of Ne is neglected. This may explain why the measured Z_{eff} tends to be somewhat lower than the prediction. Z_{eff} is measured 70 ms after the beginning of the flat top of the plasma current in ohmically heated discharges, and 40 ms after switch-on of ECRH.

Figure 8.1 shows that in helium plasmas without neon $Z_{\text{eff}} = 5.1$ was reached. This suggests that these target plasmas were already contaminated by impurities.

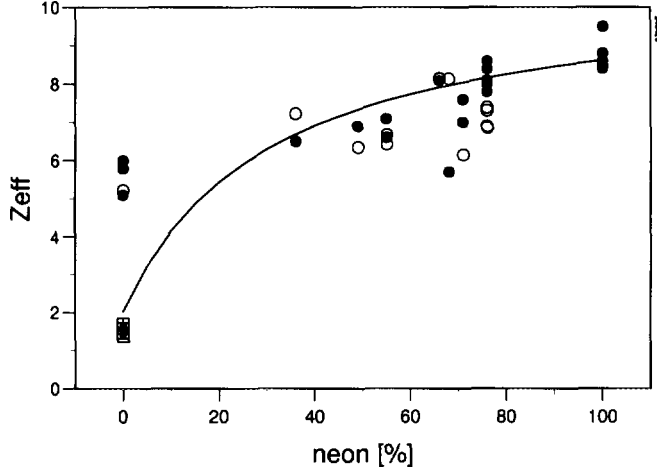


Figure 8.1: Z_{eff} (obtained from resistivity with neoclassical correction) as function of the fraction of neon in the filling gas for Ohmic plasmas (closed symbols) and ECR heated plasmas ($P_{\text{ECR}}^{\text{nom}} = 120$ kW) (open symbols) in helium/neon discharges (circles) and deuterium (squares). The full line is the expected Z_{eff} (see text). Note that in helium without neon $Z_{\text{eff}} = 5.1$, probably caused by the presence of other impurities. The low Z_{eff} deuterium plasmas were measured on another day after boronization of the vessel.

The deuterium plasmas turned out to be very clean ($Z_{\text{eff}} \simeq 1.5$).

Figure 8.2 shows $T_e(0)$ as function of Z_{eff} both in ohmically and ECR heated plasmas. In this figure the deuterium results with comparable densities have been included. The ohmic plasmas show a moderate increase of $T_e(0)$ as function of Z_{eff} from 0.59 to 0.89 keV. For the deuterium discharges, $T_e(0)$ is systematically lower during ECRH compared to helium-neon. This is caused by a slightly lower toroidal magnetic field ($B_T = 2.16$ T, while $B_T = 2.20$ T in He-Ne), which slightly broadens the ECR power deposition profile with a lower power density on axis.

The analysis presented in the following sections is based on a dataset of 27 ohmically heated discharges, with $Z_{\text{eff}} = 5.1 - 9.5$ and $n_e(0) = (2.0 - 2.8) \times 10^{19} \text{ m}^{-3}$. For the regression analysis on τ_E and χ_e the ohmic dataset is extended with 10 data points from a density scan in deuterium ($Z_{\text{eff}} = 1.5 - 2.4$ and $n_e(0) = (2.9 - 5.4) \times 10^{19} \text{ m}^{-3}$). The ECRH dataset contains 17 discharges with 120 kW nominal input power, $Z_{\text{eff}} = 1.4 - 8.4$ and $n_e(0) = (2.0 - 2.8) \times 10^{19} \text{ m}^{-3}$. Table 8.1 (page 108) shows the

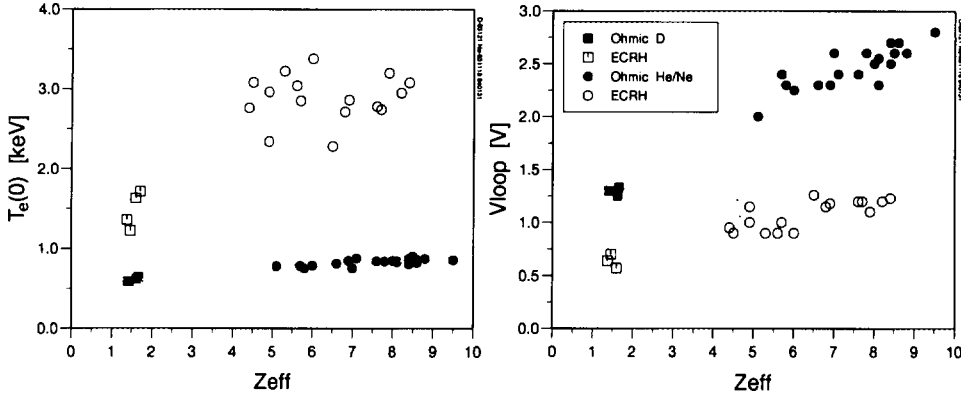


Figure 8.2: (a): Central electron temperature as function of Z_{eff} .

(b): Loop voltage as function of Z_{eff} . In the scan $I_P = 60$ kA was kept constant, so V_L is proportional to the ohmic input power.

Ohmic plasmas (closed symbols) and ECR heated plasmas ($P_{ECR}^{nom} = 120$ kW) (open symbols) in helium/neon (circles) and deuterium (squares) discharges.

range of some parameters in the dataset.

Electron density profiles are obtained by Abel inversion of the line integrated interferometer data. On average, 17 channels could be used in the analysis. Figure 8.3 shows the peakedness of $n_e(r)$ given by the ratio of central electron density to volume average density. Note that ECRH causes the $n_e(r)$ profile to broaden. Comparison between multi-position Thomson scattering measurements and interferometer data in the ohmic phase shows that the profile shapes are consistent.

Ion temperatures have not been measured in these experiments, and are set to a parametrized profile shape with $T_i(0) = 0.5$ keV in the ohmic phase; $T_i(r)$ is kept fixed at its ohmic value during ECRH. The importance of the electron-ion coupling will be discussed in Section 8.3.1.

Electron temperature profiles are measured by multi-point Thomson scattering at one timeslice in the ohmic phase, and time resolved by heterodyne ECE (low field side, X-mode). The latter diagnostic is calibrated against the ohmic $T_e(r)$ from Thomson scattering. For this purpose, $T_e(r)$ is fitted by a smooth profile of the form given independently by Kadomtsev [8]¹ and Taylor [11]¹

¹Neoclassical effects are not included in this equation. Further assumptions are: a flat Z_{eff} profile

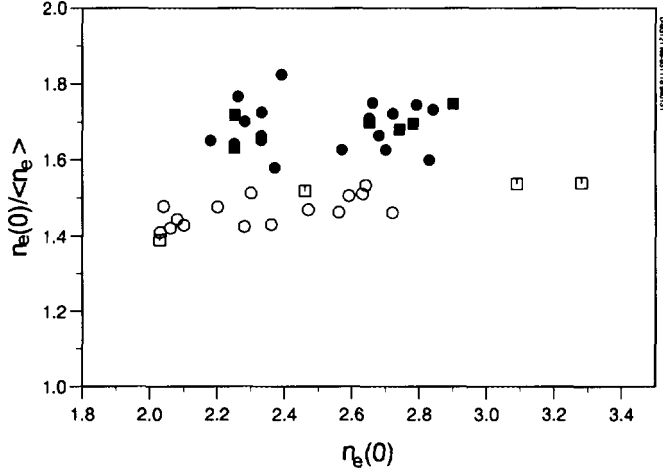


Figure 8.3: Central electron density normalized to the volume averaged density for all discharges in the Z_{eff} scan, comprising helium/neon (circles) and deuterium (squares). The peaking of $n_e(r)$ is independent of Z_{eff} . Compared to ohmic plasmas (closed symbols), $n_e(r)$ broadens during ECRH (open symbols).

$$T_e^{KT}(r) = T_e(0) \cdot \left\{ 1 + \left(\frac{r}{a} \right)^2 \left(\frac{q_a}{q_0} - 1 \right) \right\}^{-4/3} \quad (8.1)$$

where q_a and q_0 are the safety factor at the edge and in the centre, respectively. A fit of $T_e^{KT}(r)$ is performed to the experimental data with q_0 and $T_e(0)$ as free parameter (see Fig. 8.4). In high Z_{eff} plasmas, $q_0 = 1.8$ is found, while in clean conditions $q_0 = 1.5$ yields the best fit. Hence $T_e(r)$ is slightly more peaked in the low- Z_{eff} deuterium plasmas. Although it is expected that for high Z_{eff} plasmas radiation in the outer part of the plasma causes a more peaked $T_e(r)$ [19], in these discharges the effect of cooling due to radiation is dominated by an increase in input power.

To interpret the 2nd harmonic ECE radiation as temperature, the optical depth τ must be included in the analysis. For the conditions at hand, typically $\tau = 3.5$ in the centre, $\tau < 1$ for $|r| > 0.1$ m. An absorber was facing the ECE antenna, so that reflections could be neglected. Non-linearities of the envelope detector in each

and V_L is constant over the plasma radius.

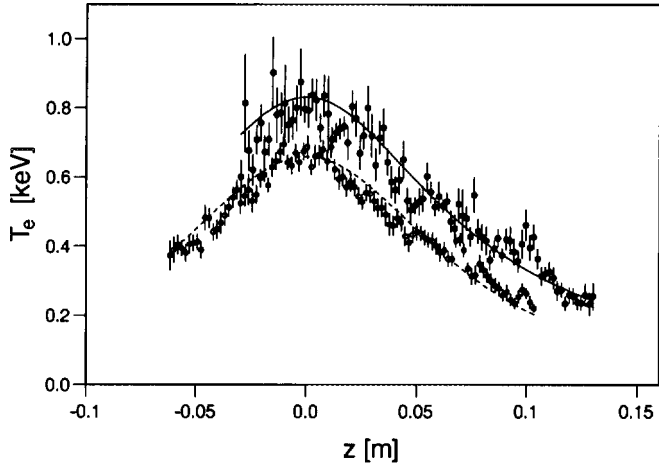


Figure 8.4: $T_e(r)$ as measured by the multi-position Thomson scattering diagnostic for ohmic discharges with $Z_{\text{eff}} = 8.1$ (closed symbols, r19931118.034) and $Z_{\text{eff}} = 1.4$ (open symbols, r19931216.023). The lines indicate the best fit through the data based on the profile shape of Kadomtsev and Taylor ($q_0 = 1.8$ and 1.5 , respectively). Measurement at $t = 140$ ms (ohmic phase), $q_a = 6.8$.

ECE-channel were incorporated individually.

In high Z_{eff} plasmas suprathermal or runaway electron populations can be created, even at higher densities, due to a higher E -field (especially during the start-up phase of the plasma). For some discharges indeed the ECE signals were dominated by non-thermal radiation. Figure 8.5 shows three typical time traces. In the lower Z_{eff} plasmas, a ‘normal’ thermal behaviour was observed. For 100% neon discharges ECE clearly showed a non-thermal behaviour. For some discharges, a high signal level was observed initially, but after typically 60 ms thermalization occurred. Discharges which showed a suprathermal behaviour (as seen either by ECE or by a high value of $\beta_p + I_i/2$ as measured by the vertical magnetic field) were not used in the analysis.

Determination of Z_{eff} . The effective ion charge is calculated from the measured $T_e(r)$ and the loop voltage measured at the outer boundary of the ohmic plasma. Assuming full current diffusion (i.e. $E(r) = E$), the average resistivity over the plasma volume is calculated using Spitzer resistivity with the neoclassical correction

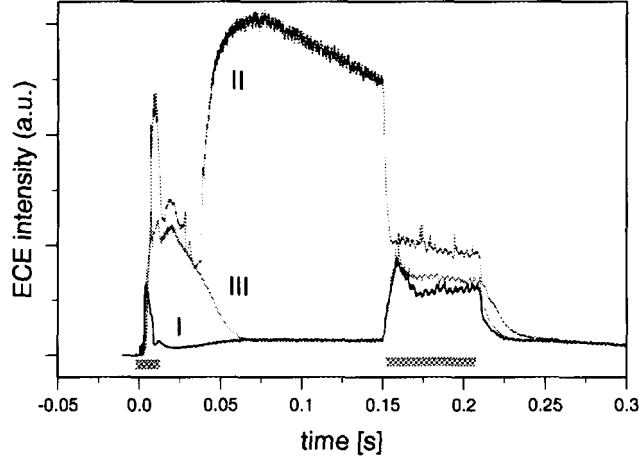


Figure 8.5: Typical heterodyne ECE timetraces from the Z_{eff} scan. Signal I shows a ‘normal’ thermal behaviour. In 100% neon plasmas, suprathermal radiation dominates (II). For high Z_{eff} , sometimes ‘thermalization’ occurred (III). ECRH (LFS 120 kW) is applied from $[-2, 8]$ and $[150, 210]$ ms.

for trapped particles.

Z_{eff} as calculated by SNAP can be compared to an estimation of Z_{eff} on axis. The latter one, which is independent of the neoclassical correction since no trapped particles are present on axis, is calculated from Spitzer resistivity, $T_e(0)$, V_L and q_0 by

$$Z_{\text{eff}} = 3.7 \frac{q_0}{B_\phi} V_L T_e(0)^{3/2} \left(\frac{16.1}{\ln \Lambda} \right) N(Z)^{-1} \quad (T_e \text{ in keV}), \quad (8.2)$$

where $N(Z)$ is the Spitzer-Härm correction for non-hydrogenic plasmas [20]. Figure 8.6 shows the comparison of Z_{eff} on axis (using q_0 that was found in the fit of $T_e(r)$ using equation (8.1)) and Z_{eff} calculated by SNAP. The latter one is consistent with Z_{eff} on axis if the neoclassical correction is taken into account.

Radiation losses were measured by a bolometer. The total level, which is expected to be proportional to $n_e^2(Z_{\text{eff}} - 1)$, is shown in Fig. 8.7. Despite the rather large error bars on the measurements, clearly a trend can be observed showing more radiation (up to 40 kW) for higher Z_{eff} plasmas. However, the magnitude is moderate compared to the ohmic input power (typically 140 kW). In deuterium plasmas

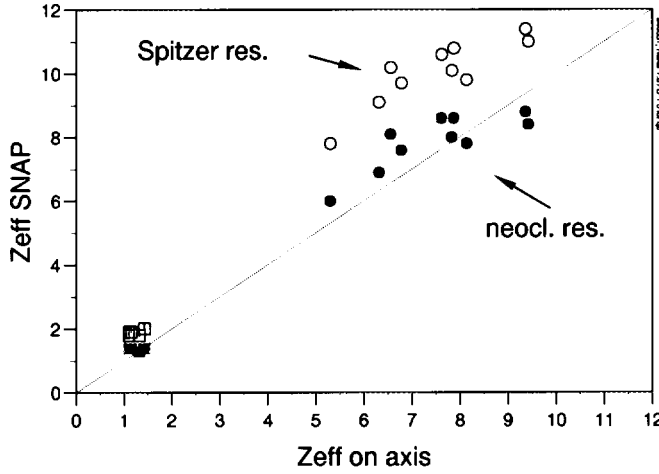


Figure 8.6: Z_{eff} calculated by SNAP, using Spitzer resistivity (open symbols) and with neoclassical correction (closed symbols). The value is compared with Z_{eff} on axis using equation 8.2 and q_0 from the fitted $T_e(r)$.

Z_{eff} was so low that radiation was hardly detectable (≤ 5 kW).

Simulations with the ICARUS predictive transport code (see Chapter 2 of this thesis), showed that line radiation of impurities is the main contribution to the total radiation level. Radially resolved, the radiation is located near the plasma edge (outside $r/a = 0.8$). Therefore, in this study radiation losses have been neglected in the local power balance analysis, which is justified as long as the analysis is limited to $r/a < 0.8$.

Electron Cyclotron Resonance Heating was applied from the low field side (O-mode), with nominal input power of $P_{\text{ECR}}^{\text{nom}} = 120 \pm 5$ kW. The actual input power is lower, as has been argued before [17], since a fraction ($\approx 20\%$, 25 kW) is lost at windows, spurious modes, etc. For the ECR power deposition profile, ray-tracing calculations were performed to estimate the amount of single pass absorbed power. Depending on the actual T_e and n_e , about 80 - 95% of the actual input power is absorbed single pass inside $r = 4$ cm (central deposition). The remaining 5-20 % is assumed to be deposited with a $1/r$ -profile.

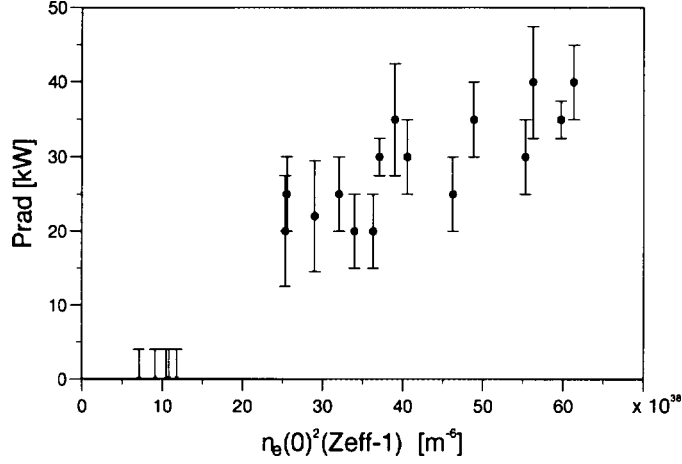


Figure 8.7: *Total radiation level as measured by the bolometer. For the (clean) deuterium discharges the radiation level was very low (≤ 5 kW).*

8.3 Transport analysis

A local power balance analysis was performed using the SNAP code (see Chapter 2 of this thesis). After a careful transformation of $T_e(r)$ and $n_e(r)$ to one-dimensional flux coordinates, SNAP calculates a.o. the local thermal diffusivity, resistivity and Z_{eff} .

8.3.1 Global confinement

Figure 8.8a shows the *electron* energy confinement time as function of Z_{eff} for ohmically heated plasmas and during ECRH. The electron energy confinement is defined by:

$$\tau_{Ee} = \frac{W_e}{P_{oh} + P_{ecrh} - P_{ei}} \quad (8.3)$$

where P_{oh} is the ohmic input power, P_{ecrh} the additional ECRH power, and P_{ei} the power transferred from the electrons to the ions. For the conditions at hand, P_{ei} is 5 – 10% of the ohmic input power, and 10 – 15% of the total input power during ECRH. Note that τ_{Ee} is used rather than τ_E , since it is the electron thermal transport that is of interest in this study.

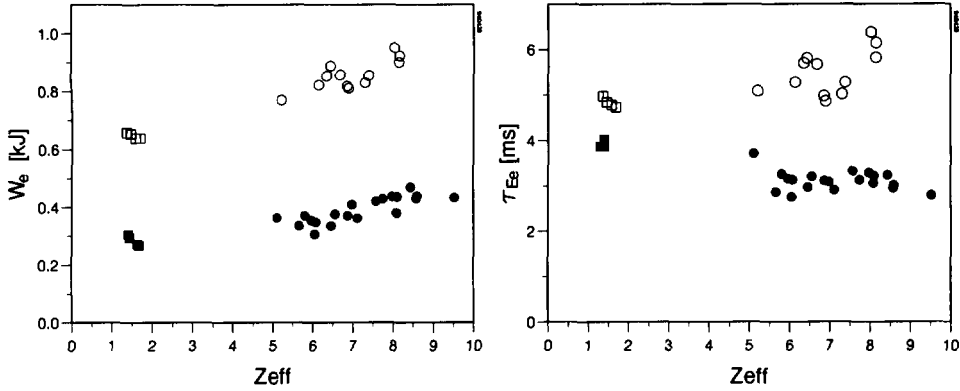


Figure 8.8: (a): Electron thermal energy in ohmic discharges (closed symbols) and during ECRH (open symbols). (b): The electron energy confinement time for ohmic plasmas (solid symbols) and during ECRH ($P_{\text{ECR}}^{\text{nom}} = 120 \text{ kW}$) (open symbols). Results are shown for deuterium plasmas (squares), and helium/neon discharges (circles).

During ECRH ($P_{\text{ECR}}^{\text{nom}} = 120 \text{ kW}$) the confinement time increases compared to the ohmic phase. Improvement of confinement during ECRH was observed before in RTP in clean discharges [17]. Note that the improvement is even more pronounced in the higher Z_{eff} plasmas.

A linear regression analysis is performed on τ_{Ee} using the logarithms of n_e and Z_{eff} . The choice of scalers is important, since correlation between scalers gives a large error in the estimated regression. Table 8.1 gives the cross-correlation coefficients of the scalers that have been used in the regression analysis for τ_{Ee} . For scalers which are determined without random error, the regression is seriously affected if the correlation coefficient r between the scalers exceeds 0.9, and it is considered safe to require $r < 0.7$. The acceptable value of r is reduced if the scalers do have a random error. The reduction depends on the ratio of random error to the range of scalers. In our dataset, n_e and T_e are well determined.

A number of conclusions can be drawn from table 8.1. Firstly, T_e and n_e are not correlated in ohmic discharges. They are, however, anti-correlated during ECRH, which is in agreement with L-mode scaling [16]. There is no significant correlation between n_e and Z_{eff} both in the ohmic case and during ECRH. In ohmic plasmas

Table 8.1: *The cross-correlation coefficients for parameters that were used in the regression analysis. The data set contains 37 and 17 elements for ohmically and ECR heated ($P_{\text{ECR}}^{\text{nom}} = 120 \text{ kW}$) discharges, respectively. Units are $[10^{19} \text{ m}^{-3}]$ and $[\text{keV}]$.*

Ohmic				Parameter range			
$N = 37$	$n_e(0)$	$T_e(0)$	Z_{eff}	Mean	Std.Dev.	Minimum	Maximum
$n_e(0)$	1.00	-0.61	-0.55	2.9	0.9	1.8	5.5
$T_e(0)$	-0.61	1.00	0.93	0.75	0.09	0.59	0.89
Z_{eff}	-0.55	0.93	1.00	5.1	3.0	1.4	9.5

ECRH				Parameter range			
$N = 17$	$n_e(0)$	$T_e(0)$	Z_{eff}	Mean	Std.Dev.	Minimum	Maximum
$n_e(0)$	1.00	-0.88	-0.63	2.4	0.4	1.8	3.3
$T_e(0)$	-0.88	1.00	0.72	2.51	0.60	1.22	3.33
Z_{eff}	-0.63	0.72	1.00	6.0	2.3	1.4	8.2

T_e is coupled to Z_{eff} via the resistivity. During ECRH this effect is less pronounced, as demonstrated by a lower correlation coefficient, since the ohmic heating power has a smaller contribution. The following scaling was found with n_e and Z_{eff} as the independent scalers:

$$\tau_{Ee}(\text{Ohmic}) = (2.0 \pm 0.1) n_e^{0.73 \pm 0.07} Z_{\text{eff}}^{-0.16 \pm 0.03}, \quad (8.4)$$

in units $[\text{ms}]$ and $[10^{19} \text{ m}^{-3}]$.

The root-mean-square error of this fit (rmse) is 4.2%, which is smaller than the experimental error in τ_{Ee} (typically 10%). The favourable scaling with density is consistent with previous regression analyses on RTP data.

For the ECRH dataset we find

$$\tau_{Ee}(\text{ECRH}) = (7.3 \pm 0.4) n_e^{0.40 \pm 0.14} Z_{\text{eff}}^{0.03 \pm 0.04}, \quad (8.5)$$

with rmse= 3%. The relatively large error in the exponent of n_e is due to the limited range in which the density has been varied during ECRH. In practice, n_e was almost constant. A scaling without n_e yields:

$$\tau_{Ee}(\text{ECRH}) = (57 \pm 0.06) Z_{\text{eff}}^{0.09 \pm 0.03}, \quad (8.6)$$

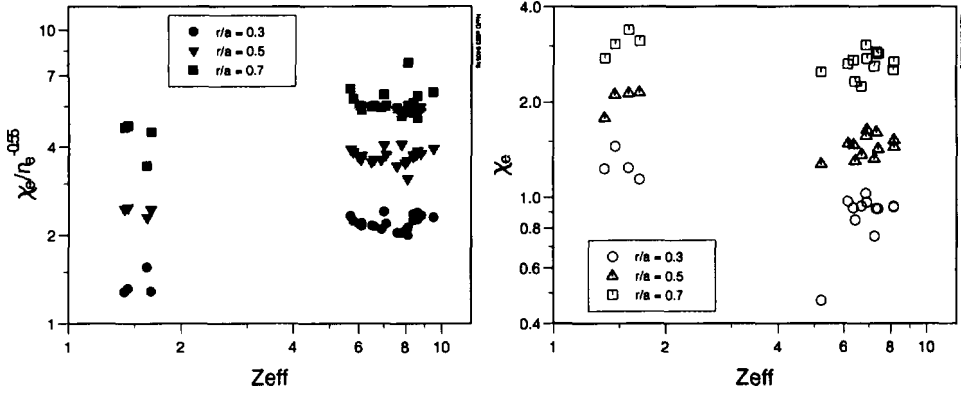


Figure 8.9: Results of the local power balance analysis: the electron thermal diffusivity as function of Z_{eff} . In ohmic plasmas, χ_e is normalized to $n_e(r)^{-0.55}$ as obtained from regression analysis. Results are for ohmically heated discharges (closed symbols) and during ECRH ($P_{ECR}^{nom} = 120$ kW) (open symbols).

with $rmse = 3.5\%$. In both cases no scaling with Z_{eff} is found.

8.3.2 Local transport

A local power balance analysis has been performed on the Z_{eff} scan data using the SNAP code. The electron energy balance includes the ohmic input power from loop voltage and plasma current, electron-ion coupling (which is negligible), and the ECRH power deposition profile from (single pass) ray-tracing taking multiple pass reflections into account. Radiation is neglected, as has been argued in Section 8.2.

Figure 8.9 shows the thermal electron diffusivity $\chi_e(r)$ as function of Z_{eff} . A regression analysis of χ_e at the various position yields the following dependencies for ohmically and ECR heated plasmas:

$$\chi_e(\rho) \sim n_e(\rho)^\alpha Z_{eff}^\beta. \quad (8.7)$$

with

	Ohmic		ECRH	
	α	β	α	β
$\chi_e(\rho = 0.3) :$	-0.65 ± 0.12	0.29 ± 0.02	-	-0.22 ± 0.08
$\chi_e(\rho = 0.5) :$	-0.46 ± 0.12	0.25 ± 0.03	-	-0.21 ± 0.04
$\chi_e(\rho = 0.7) :$	-0.54 ± 0.18	0.16 ± 0.04	-	-0.09 ± 0.04

In the regression analysis the local values of $\chi_e(r)$ and $n_e(r)$ have been incorporated. In ohmic plasmas, the density dependence is within the errorbars equal at all radii, and consistent with the scaling of global energy confinement. To show the Z_{eff} dependence, the ohmic χ_e in Fig. 8.9 is normalized to $n_e(r)^{-0.55}$. During ECRH, the change in density was too small to include n_e in the regression analysis. There is, however, no correlation between n_e and Z_{eff} (see Table 8.1). Comparing the ohmic and ECR cases, an opposit, although weak, scaling is found for Z_{eff} . In the ohmic case, the local analysis is consistent with the scaling of τ_{Ee} . During ECRH, the scaling of χ_e with Z_{eff} at $\rho = 0.7$ is consistent with the global scaling, but near the plasma centre χ_e shows a stronger, although still weak dependence on Z_{eff} .

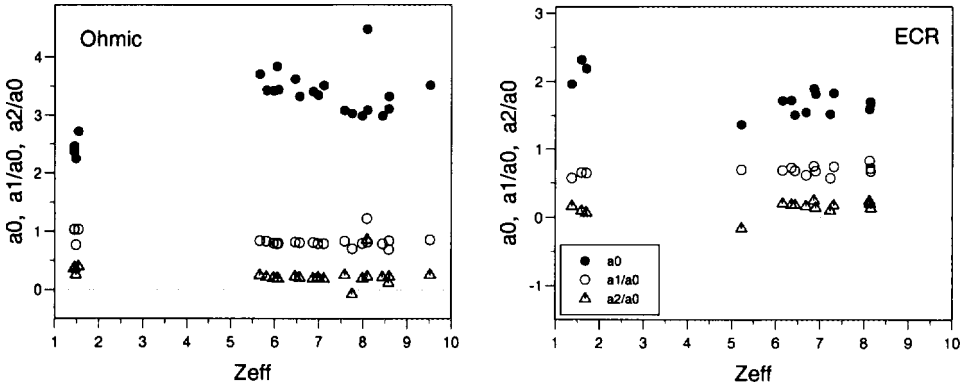


Figure 8.10: The first 3 Legendre coefficients of $\chi_e(r)$ over the interval $\rho = [0.2, 0.8]$ from the Z_{eff} experiment. Left graph: ohmic heating, right graph: during ECRH. The interpretation of the coefficients: a_0 : mean value; $a_1/a_0 > 0$ (< 0): linearly increasing (decreasing); $a_2/a_0 > 0$ (< 0): concave (convex). All coefficients apply to the same scale.

Using an alternative representation, $\chi_e(r)$ can be expressed in terms of Legendre coefficients (see Appendix A). The advantage of this representation is that profile characteristics from a large dataset are displayed, like an increasing, decreasing, concave or convex behaviour. Figure 8.10 shows the first three Legendre coefficients for the experimental $\chi_e(r)$ in the Z_{eff} dataset. The first Legendre coefficient (a_0) slightly changes when Z_{eff} is increased: a positive slope in the ohmic case, and an inverse trend during ECRH. This is consistent with the scaling of Z_{eff} in eq. (8.7). Striking is the lack of dependence of the other Legendre coefficients on Z_{eff} . It indicates that it is only the mean value of $\chi_e(r)$ that is modified, but not its shape.

8.3.3 Scaling with collisionality

In the experiments described above, the response of χ_e to the engineering parameter Z_{eff} was searched for. However, the transport relevant parameter that actually is varied (using the ‘knob’ Z_{eff}) is the electron collisionality ν_e^* . In this section the dependence of χ_e to ν_e^* is studied.

Values of ν_e^* as function of radius are shown in Fig. 8.11 for low and high Z_{eff} and ohmic and ECR heated discharges. In the ohmic case, $\nu_e^* > 1$ everywhere (neoclassical plateau regime), while during ECRH $\nu_e^* < 1$ (banana regime) over a large region of plasma radius. It is thus well possible that during ECRH another transport regime is applicable. Note that in the ohmic case an increase in Z_{eff} has a large effect on ν_e^* . During ECRH, ν_e^* is dominated by the high T_e , while changes in Z_{eff} only have a marginal influence for $r/a \leq 0.5$.

Figure 8.12 shows χ_e at three radial positions as function of the electron collisionality. In the ohmic case, χ_e is normalized by the local density dependence that was found by regression analysis on χ_e using n_e and ν_e^* as scaling parameters.

$$\chi_e(\rho) \sim n_e(\rho)^\gamma \nu_e^*(\rho)^\delta. \quad (8.8)$$

with

	Ohmic	
	γ	δ
$\chi_e(\rho = 0.3) :$	-1.23 ± 0.12	0.38 ± 0.03
$\chi_e(\rho = 0.5) :$	-1.19 ± 0.13	0.43 ± 0.04
$\chi_e(\rho = 0.7) :$	-1.31 ± 0.21	0.45 ± 0.07

From the regression analysis it follows that the scaling of χ_e with collisionality is

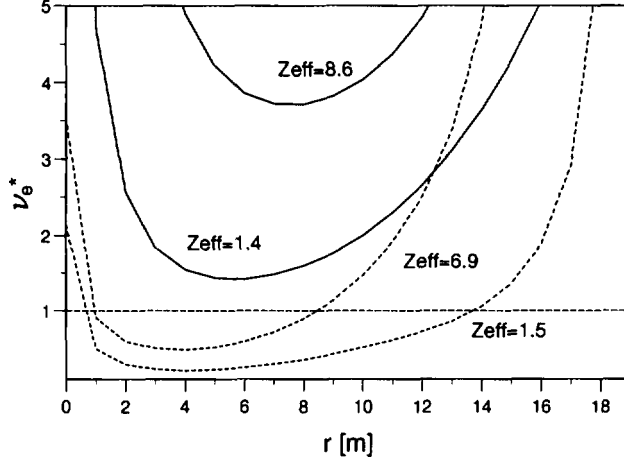


Figure 8.11: The electron collisionality for 4 cases in the Z_{eff} dataset: low and high Z_{eff} in ohmically heated plasmas (full curve) and during ECRH (dashed curve). Densities are $\langle n_e \rangle = 1.6 \times 10^{19} \text{ m}^{-3}$ (ohmic cases) and $\langle n_e \rangle = 1.7 \times 10^{19} \text{ m}^{-3}$ (ECRH cases). The transition banana-plateau regime is near $\nu_e^* = 1$.

stronger than the previous scaling with Z_{eff} . This means that a masked dependence on T_e exists, which shows up when ν_e^* is used as scalar.

During ECRH, ν_e^* is modified only moderately at each radial position, and a large scatter is observed between χ_e and ν_e^* . The tendency of χ_e to increase with ν_e^* could be caused by colinearity between ν_e^* and ρ .

8.4 Comparison with transport models

The experimentally obtained $\chi_e(r)$ in the Z_{eff} scan are compared to the predictions of a selection of transport models that were discussed in Chapter 4 of this thesis.

Based on the scaling of $\chi_e(r)$, a number of models can be immediately rejected: the ones that show a too strong positive or negative dependence on Z_{eff} (or ν_e^*). Of the remaining models, the comparison with the experimental dataset will be made in two ways. Firstly, the cross-correlation coefficient between χ_e from model and experiment is calculated at three radial positions. Cross-correlation is a commonly used method to detect trends in datasets. In another method, each χ_e is expanded in

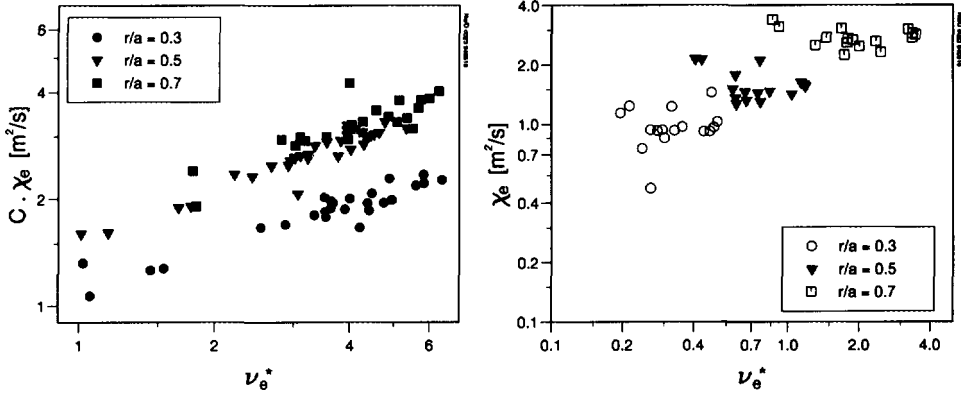


Figure 8.12: The electron thermal diffusivity as function of the electron collisionality ν_e^* . Results are for ohmically heated discharges (left figure) and during ECRH ($P_{\text{ECR}}^{\text{nom}} = 120 \text{ kW}$) (right figure). In the ohmic case, χ_e is normalized by the scaling with density ($C_{\text{norm}} = (\langle n_e \rangle / n_e(r))^{-1.2}$ with $\langle n_e \rangle = 1.6 \times 10^{19} \text{ m}^{-3}$ the averaged density over the whole dataset).

its Legendre coefficients, and the coefficients are compared. This method allows the comparison of profile characteristics and can reveal correlated trends in the shapes of $\chi_e(r)$ which are missed in the cross-correlation analysis.

For each transport model, $\chi_e(r)$ is calculated with the following input parameters from experimental data: $T_e(r)$, $n_e(r)$, V_L , and magnetics. Derived quantities that are used as input data are Z_{eff} (assumed to be constant as function of radius), $n_i(r)$ (calculated from $n_e(r)$ and Z_{eff}), a parametrized $T_i(r)$, and $q(r)$.

8.4.1 Cross-correlation analysis

For the comparison between χ_e obtained from model and experiment, the cross-correlation coefficient is used, which is defined as:

$$c_{xy} = \frac{\frac{1}{N} \sum_i (x_i - \bar{x})(y_i - \bar{y})}{\sqrt{\frac{1}{N} \sum_i (x_i - \bar{x})^2} \sqrt{\frac{1}{N} \sum_i (y_i - \bar{y})^2}}, \quad (8.9)$$

where x_i and y_i correspond to χ_e from experiment and model, respectively, i denotes each $\chi_e(r)$ in the dataset, and \bar{x} , \bar{y} are the mean values over the dataset.

The detailed results of the cross-correlation analysis are presented in appendix A. In the ohmic case, a few models show a significant positive correlation: the driftwave model of WEILAND, the model of OHKAWA based on current filamentation, and COPPI, MAZZUCATO, GRUBER based on profile consistency. Interestingly, anti-correlation is displayed by DIAMOND, BIGLARI (trapped ion driven). During ECRH, however, the latter model shows a positive correlation. The only other models that show a positive correlation during ECRH is the drift mode for untrapped electrons (SIMILON, DIAMOND). Note that, in contrast to observations in clean conditions [17], the REBUT-LALLIA-WATKINS model performs badly.

In general, there is no model that shows correlation with the Z_{eff} dataset *both* in the ohmic case and during ECRH.

8.4.2 Correlation between Legendre coefficients

The use of cross-correlation coefficients is a crude method in which trends in profile shapes like an increasing, decreasing, concave or convex profiles become unimportant. For each transport model a similar plot could be given as Fig. 8.10, revealing immediately trends in $\chi_e(r)$ as Z_{eff} is varied. An example is given in Fig. 8.13 for the models of WEILAND and OHKAWA.

Except for the averaged value a_0 , the higher order Legendre coefficients in the experimental dataset showed a remarkable lack of scaling with Z_{eff} . On that basis, already some models can be discarded for analysis, when a_1 and a_2 vary significantly as function of Z_{eff} . For the remaining candidates, the correlation between the Legendre coefficients is estimated (see Appendix C).

There is no model that shows the same trend as the experimental data for all three characteristics (mean value, increasing/decreasing, concave/convex) simultaneously. The models of WEILAND and COPPI, MAZZUCATO, GRUBER show the same trend as the experimental dataset for average value a_0 . The insensitivity of the profile shape of $\chi_e(r)$ to changes in Z_{eff} is not predicted by any of the selected transport models.

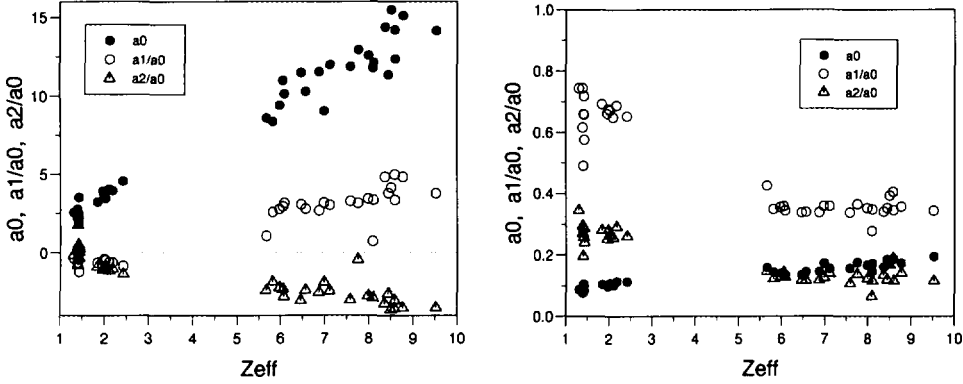


Figure 8.13: The first 3 Legendre coefficients fitted to $\chi_e(r)$ of the model of WEILAND (left) and OHKAWA (right) in ohmically heated plasmas. The interpretation of the coefficients: a_0 : mean value; $a_1/a_0 > 0$ (< 0): linearly increasing (decreasing); $a_2/a_0 > 0$ (< 0): concave (convex). For example: WEILAND gives a flat $\chi_e(r)$ for low Z_{eff} , and linearly increasing and bulbous $\chi_e(r)$ -profile for higher Z_{eff} .

8.5 Discussion and Conclusion

A Z_{eff} scan was performed in a mixture of helium and neon discharges. Z_{eff} was calculated using neoclassical resistivity. A consistent picture was obtained for the fit of $T_e(r)$, Z_{eff} on axis (with no trapped particles) and Z_{eff} calculated by SNAP. The obtained value is close to, but systematically lower than the expected Z_{eff} based on the averaged ionization states of neon. This is well possible caused by the fact that full ionization of Ne^{9+} might not be reached for the conditions at hand, at the time of analysis.

In full neon discharges, the ECE measurement was dominated by suprathermal radiation. As a consequence, the 100% neon discharges were excluded from the ECRH dataset (the Thomson scattering measurement was always in the ohmic phase).

In the regression analysis it was shown that n_e and Z_{eff} are decoupled, and can be used as scalers for τ_{Ee} . During ECRH, τ_{Ee} increases with respect to the ohmic phase, which is consistent with previous observations of improved confinement during ECRH.

The central conclusion of this study is that *there is no scaling of τ_{Ee} with Z_{eff}* . The increase of W_e when Z_{eff} increases from 1.5 to 9.5 is balanced by the increase in (ohmic) input power. χ_e shows a weak dependence on Z_{eff} , and, more pronounced, scaling with ν_e^* . This means that collisions play an essential role in anomalous transport. The fact that during ECRH $\nu_e^* < 1$ over a large region of plasma radius, while $\nu_e^* > 1$ in the ohmic phase, can explain the improvement of confinement during ECRH, since the average χ_e is lower. It does not explain, however, the degradation of confinement when more ECR power is applied [17], unless there is a critical value for ν_e^* below which χ_e becomes independent of collisionality.

For the comparison of transport models, radial trends of χ_e were compared to χ_e from experiment. Two methods have been used: the ‘standard’ cross-correlation at three radial positions, and the comparison of χ_e ’s expressed in their Legendre coefficients. Some models could be immediately rejected based on the scaling with Z_{eff} . Correlation with our dataset shows that for some models good agreement was found, either in ohmic or ECR heated discharges. There is, however, no model that gives a good prediction in both regimes. If, however, another ‘mode’ is reached during ECRH (e.g. the improved confinement regime as discussed in Chapter 6), then it is not surprising that ohmic and ECR conditions cannot be predicted well simultaneously. Most models predict a single relation between q_e and ∇T_e , and the transition to another regimes is not accounted for.

8.6 Appendix A. Expansion in Legendre polynomials

In this section a method is presented that quantifies characteristics of a profile in terms of Legendre coefficients. This allows the comparison of profile characteristics (like that of $\chi_e(r)$) in a large dataset.

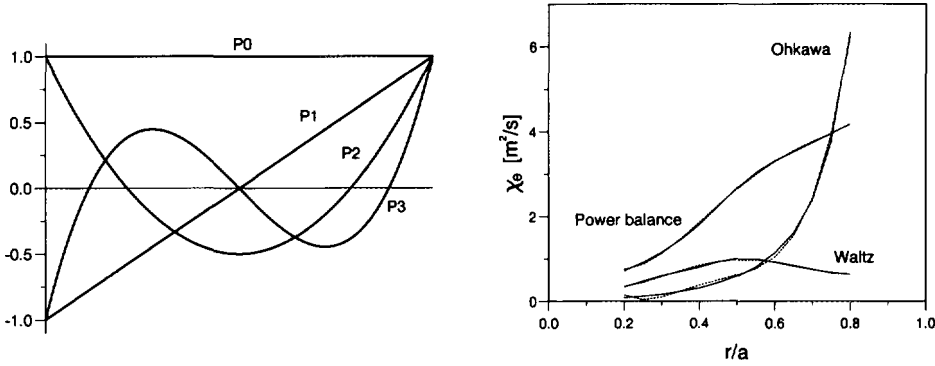


Figure 8.14: *Legendre polynomials as function of x in the range $[-1, +1]$. The left graph shows the first four basic functions. The right figure is an example of fitted $\chi_e(r)$ profiles in the range $[0.2, 0.8]$ with Legendre polynomials. The dashed curves indicate the fitted profile, when only 4 Legendre terms are included. The fit parameters are: Power balance ($a_0=2.52$, $a_1/a_0=0.76$, $a_2/a_0=-0.07$, $a_3/a_0=-0.10$: linearly increasing, not concave or convex); WALTZ ($a_0=0.76$, $a_1/a_0=0.18$, $a_2/a_0=-0.47$, $a_3/a_0=0.01$: not linearly increasing and concave); OHKAWA ($a_0=1.21$, $a_1/a_0=1.75$, $a_2/a_0=1.26$, $a_3/a_0=0.77$: linearly increasing, hollow).*

The basic idea is that a profile is expanded in a set of functions, like:

$$\chi_e(r) = \sum_{k=0}^M a_k P_k(r) \quad (8.10)$$

where the coefficients a_k need to be fitted, given the set of fixed basis functions $P_k(r)$. Then, the coefficients a_1, a_2, \dots, a_M form a representation of $\chi_e(r)$.

The set $P_k(r)$ can be chosen arbitrarily, provided they form a set of orthogonal functions. For the application to $\chi_e(r)$ profiles, the choice of Legendre polynomials as basis functions seems appropriate. They are given by:

$$P_n(x) = \frac{1}{2^n n!} D^n (x^2 - 1)^n \quad (8.11)$$

where D^n is defined as $D^n f(x) = f^{(n)}(x)$ the n -th derivative, and x lies in the interval $[-1, +1]$. Explicitly, the first 5 terms are given by:

$$\begin{aligned} P_0(x) &= 1 & P_3(x) &= \frac{1}{2}(5x^3 - 3x) \\ P_1(x) &= x & P_4(x) &= \frac{1}{6}(25x^4 - 12x^2 - 1) \\ P_2(x) &= \frac{1}{2}(3x^2 - 1) & & \text{etc.} \end{aligned}$$

Figure 8.14a shows the first few Legendre polynomials. If $\chi_e(r)$ in the interval $\rho = [0.2, 0.8]$ is expanded in these functions, the coefficients a_0, \dots, a_k represent the relative contribution of each Legendre term to $\chi_e(r)$. The choice for this set of basis functions now becomes clear: each polynomial ‘represents’ a typical characteristic. For example, the zeroth order gives the mean value over the interval. The first coefficient indicates the linear behaviour (i.e. linearly increasing or, if a negative coefficient is found, a decreasing trend of the fitted profile over the interval). The contribution of the second Legendre term gives information about hollowness (concave or convex) of the fitted function. The third term is somewhat more difficult to interpret. It typically shows up stronger when higher frequency components are present.

The use of Legendre coefficients for the expansion of $\chi_e(r)$ is limited to outside the plasma centre, since in the centre $d\chi_e(r)/dr = 0$, which cannot be fitted by only the first few Legendre terms. Usually, this limitation is unimportant, since there are large uncertainties in χ_e near the centre due to the small ∇T_e .

As an example, Fig. 8.14b also shows typical $\chi_e(r)$ profiles from experiment and transport models. Only 4 Legendre functions are needed to obtain a good fit ($\chi^2 < 0.01$). The fit coefficients (see figure caption) give the characteristics of the profile shape satisfactorily.

8.7 Appendix B. Comparison with models: cross-correlation

This appendix gives the correlation between $\chi_e(r)$ from power balance analysis and from a number of transport models. The model numbers indicate the section where the model was described in Chapter 4 of this thesis. The data set contains 37 and 17 elements for ohmically and ECR heated ($P_{\text{ECR}}^{\text{nom}} = 120$ kW) discharges, respectively. The cross-correlation coefficients are calculated at three radial positions ($\rho = 0.3, 0.5$ and 0.7).

CROSS-CORRELATION χ_e		Ohmic ($N = 37$)			ECRH ($N = 17$)		
<i>Author(s)</i>	<i>Model</i>	$\rho = 0.3$	0.5	0.7	$\rho = 0.3$	0.5	0.7
(2.1) Waltz, Dominguez	Trapped electron	-0.64	-0.52	0.10	-0.17	0.21	0.01
	Circulating electron	0.55	0.53	0.23	-0.17	-0.47	-0.27
	Linear combination	-0.59	-0.31	0.41	-0.35	-0.05	-0.10
(2.3) Similon, Diamond	Circulating; Tor. cur.	-0.09	-0.21	0.30	0.60	0.81	0.56
	Trapped dissipative	0.64	0.66	0.43	-0.35	-0.64	-0.56
	Trapped collisionless	-0.59	-0.58	-0.13	0.65	0.82	0.61
(2.5) Diamond, Biglari	Trapped ion driven	-0.72	-0.73	-0.29	0.69	0.83	0.56
(2.6) Weiland	η_i and trapped el.	0.71	0.71	0.31	-0.71	-0.81	-0.74
(3.1) Kadomtsev, Pogutse	Magn. turb.	0.23	0.35	0.50	-0.69	-0.64	-0.56
(3.2) Ohkawa	Current filamentation	0.73	0.69	0.23	-0.42	-0.50	-0.16
(3.3) Rebut, Lallia	Critical gradient	0.26	0.38	-0.26	-0.67	-0.84	-0.86
(4.1) Zhang, Mahajan	Electromagnetic turb.	0.43	0.44	0.41	-0.70	-0.72	-0.72
(4.2) Guzdar	High freq. el.magn.	-0.39	-0.27	-0.42	-0.68	-0.88	-0.84
(5.1) Coppi, Mazzucato	Profile consistency	0.94	0.90	0.53	-0.58	-0.58	-0.30
(5.2) Dnestrovskij	Canonical profiles	-0.32	0.56	0.33	-0.77	-0.81	-0.63

8.7 Appendix C. Comparison with models: Legendre coefficients

This appendix gives the correlation between $\chi_e(r)$ from power balance analysis and from a number of transport models. As described in Appendix A, each $\chi_e(r)$ is expanded in Legendre polynomials according to $\chi_e(r) = \sum_{k=0}^M a_k P_k(r)$. The thus obtained Legendre coefficients from model and experiment are cross-correlated.

A positive correlation means that χ_e from the model shows the same trend as the experimental data in the Z_{eff} scan. The coefficients can be interpreted as (see text): a_0 : mean absolute value; a_1 : linear behaviour; a_2 : concave or convex.

The results are summarized in the following table. The model numbers indicate the section where the model was described in Chapter 4 of this thesis.

CROSS-CORRELATION LEGENDRE COEFFICIENTS		Ohmic ($N = 37$)			ECRH ($N = 17$)		
<i>Author(s)</i>	<i>Model</i>	a_0	a_1/a_0	a_2/a_0	a_0	a_1/a_0	a_2/a_0
(2.1) Waltz, Dominguez	Trapped electron	-0.28	-0.52	0.07	0.02	-0.53	0.49
	Circulating electron	0.42	-0.63	-0.27	-0.47	-0.12	-0.28
	Linear combination	0.03	-0.49	-0.14	-0.27	-0.49	0.46
(2.3) Similon, Diamond	Circulating; Tor. cur.	0.10	0.16	-0.11	0.63	-0.38	0.65
	Trapped dissipative	0.68	-0.38	0.11	-0.48	-0.41	0.55
	Trapped collisionless	-0.52	0.12	-0.10	0.68	-0.43	0.59
(2.5) Diamond, Biglari	Trapped ion driven	-0.55	-0.38	0.07	0.75	-0.43	0.56
(2.6) Weiland	η_i and trapped el.	0.61	-0.78	-0.93	-0.13	-0.31	-0.81
(3.1) Kadomtsev, Pogutse	Magn. turb.	0.45	-0.25	-0.11	-0.67	-0.51	0.12
(3.2) Ohkawa	Current filamentation	0.48	0.33	0.02	-0.36	-0.37	-0.48
(3.3) Rebut, Lallia	Critical gradient	0.23	-0.76	-0.55	-0.80	-0.88	0.04
(4.1) Zhang, Mahajan	Electromagnetic turb.	0.64	-0.77	-0.63	-0.72	-0.82	0.11
(4.2) Guzdar	High freq. el.magn.	-0.37	-0.20	-0.70	-0.80	-0.03	-0.64
(5.1) Coppi, Mazzucato	Profile consistency	0.78	0.05	-0.49	-0.51	-0.09	-0.46
(5.2) Dnestrovskij	Canonical profiles	0.34	-0.34	0.31	-0.77	-0.51	0.25

References

- [1] CHRISTIANSEN J.P., CORDEY J.G. and THOMSON K. (1990) *Nucl. Fusion* **30**, 1183.
- [2] CHRISTIANSEN J.P. *et al.* (1992) *Nucl. Fusion* **32**, 291.
- [3] LOPES CARDOZO N.J. and DE HAAS J. (1990) *Nucl. Fusion* **30**, 521.
- [4] OOMENS A.A.M. (1994) *Trans. of Fusion Techn.* **25**, 267.
- [5] MESERVEY E. *et al.* (1984) *Nucl. Fusion* **24**, 3.
- [6] MURAKAMI M. *et al.* (1979) *Proc. 7th IAEA Int. Conf.*, Innsbruck 1978, Vol.1 269 IAEA-CN-37/N-4, Vienna.
- [7] TFR-GROUP and FOM-ECRH TEAM (1988) *Nucl. Fusion* **28**, 1995.
- [8] KADOMTSEV B.B. (1987) *Phil. Trans. R. Soc. Lond.* **A322**, 125-131.
KADOMTSEV B.B. (1992) *Plasma Physics and Controlled Fusion* **34**, 1931.
- [9] SUMMERS H.P. (1979) Astrophysics Research Division, Culham Laboratory report AL-R-5.
- [10] POST D.E. and JENSEN R.V. (1977) *Atomic Data and Nuclear Data Tables* **20**, 397.
- [11] TAYLOR J.B. (1990) Report IFSR 447.
- [12] KAYE S.M., LEVINTON F.M., HATCHER R., KAITA R., KESSEL C., LEBLANC B., MCCUNE D.C. and PAU S. (1992) Report PPPL-2807.
- [13] TFR EQUIPE (1977) *Nucl. Fusion* **17**, 213.
- [14] VAN LAMMEREN A. (1991) Thesis Rijksuniversiteit Utrecht.
- [15] VAN MILLIGEN B.P.H. (1991) Thesis Rijksuniversiteit Utrecht.
- [16] SMITS F. (1991) Thesis Rijksuniversiteit Utrecht.
- [17] KONINGS J.A. *et al.* (1994) *Plasma Physics and Controlled Fusion* **36**, 45.
- [18] ARUNASALAM V. *et al.* (1990) *Nucl. Fusion* **30**, 2111.
- [19] DNESTROVSKIY YU.N., BEREZOVSKIY E.L., LYSENKO S.E., PIVINSKIY A.A. and TARASYAN K.N. (1991) *Nucl. Fusion* **31**, 1877.
- [20] SPITZER L. and HÄRM R. (1953) *Phys. Rev. Letters* **89**, 977.

Chapter 9

Poloidal asymmetries induced by off-axis ECRH

This chapter reports on off-axis ECRH heating experiments in RTP. Using off-axis ECRH, steady-state asymmetric $T_e(r)$ profiles are reproducibly obtained, as measured by ECE at two different toroidal positions. The asymmetry is most pronounced if the resonance position is more than $0.1(r/a)$ from the magnetic axis. A simple model based on transport of heated electrons along magnetic field lines and the toroidal position of the ECE diagnostic with respect to the ECRH launcher, can qualitatively explain the main aspects of the observed asymmetries.

9.1 Introduction

In the RTP tokamak, Electron Cyclotron Resonance Heating (ECRH) is used to study transport both in steady state and during transients. Since ECRH only couples to resonant electrons, it can be used as a localized heating source. By changing the ECRH resonance condition, the spatial deposition position can be controlled, which allows direct modification of the electron temperature profile $T_e(r)$ and the local power balance.

This chapter reports on off-axis ECRH heating experiments accomplished by scanning the toroidal magnetic field. Previous observations in RTP [1] have shown that under off-axis heating, asymmetric $T_e(R)$ profiles measured by the ECE radiometer (as function of major radius R in the midplane) were reproducibly obtained if the resonance position was sufficiently far off-axis.

It is important to understand the reason why $T_e(R)$ is asymmetric. If the asymmetry in $T_e(R)$ is an artefact in the measurement, then it can lead to a misinterpretation of the calculated transport coefficients. In the local power balance analysis, $T_e(R)$ is usually transformed to local flux coordinates (ρ, Θ, ϕ) . In the case of RTP, cylindrical (1D) symmetry is assumed based on the concept of equilibration of pressure on flux surfaces. When $T_e(R)$ is not symmetric with respect to the magnetic axis, a correct interpretation of $T_e(\rho)$ fails. For dynamic transport studies, the perturbed temperature \tilde{T}_e can also be asymmetric and give rise to differences in transport coefficients obtained on the low- and high field side.

It is shown by DENDY [2] that off-axis ECRH can lead to helical bands of suprathermal electrons. Whether these form or not depends on the resonant flux surface: helical bands form where q is (close to) a simple rational number, whereas for irrational q poloidal symmetry is obtained. The presence of helical bands of suprathermal electrons could influence the ECE measurement. The increased cyclotron radiation could then be incorrectly interpreted as temperature.

In this chapter further analysis of the origin the asymmetric steady state $T_e(R)$ is done. Experiments are performed in which the ECRH resonance position is scanned, with the ECE diagnostic at two toroidal positions. This allows a check whether the observed asymmetries can be related to geometrical factors.

This chapter is structured as follows. First, the ECRH position scan is described. Of special interest is the ECRH deposition profile which is obtained from the ECE time response at switch-on and switch-off of ECRH. Then, asymmetries in steady state $T_e(R)$ are discussed. A very simple model is presented which could explain the

observed asymmetries, based on transport of heated electrons along field lines. The model is tentative, but the results give hope that further extensions of the model can give a satisfactory description of the data.

9.2 ECRH Position scan

The RTP tokamak (major radius $R_0 = 0.72$ m, minor radius $a = 0.16$ m) is equipped with an extensive number of diagnostics to identify (electron) thermal transport [3], a.o. a scannable single-point Thomson scattering system, a 20-channel double-heterodyne ECE radiometer (channel bandwidth 3 GHz, spatial resolution ≈ 1.5 cm), and a 19-chord interferometer. In recent experiments also a 100 channel Thomson scattering system was available. For steady state transport analysis a modified version of the time-independent 1-D transport code SNAP developed at PPPL [4] is used.

In this experiment, ECRH is applied from the low field side (100 ms, 60 GHz, O-mode) in the equatorial plane. Off-axis ECRH heating is achieved by a toroidal magnetic field scan from 1.99 to 2.35 T (central heating $B_T = 2.14$ T), which corresponds to a shift in resonance position from -5 to $+7$ cm. The off-axis position scan is performed in helium plasmas with $q_a = 6.8$, $n_e(0) = (3.3 \pm 0.1) \times 10^{19} \text{ m}^{-3}$, $P_{OH} = 115$ kW in the ohmic phase and nominal ECRH input power $P_{ECR} = 180$ kW. T_e -profiles are measured using second harmonic X-mode ECE. For the plasma conditions at hand, the correction for optical thickness for 2nd harmonic X-mode [5] is negligible in the centre, becomes 10% at $r/a = 0.45$, and increases to 40% near the edge.

Figure 9.1 shows the ECRH deposition profiles at various deposition positions, measured from the time response of the heterodyne ECE both at switch-on and switch-off of ECRH:

$$p_{ECRH}(r) = \frac{dW_e}{dt} = \frac{3}{2}n_e(r)\frac{\partial T_e(r)}{\partial t} + \frac{3}{2}T_e(r)\frac{\partial n_e(r)}{\partial t} \quad (9.1)$$

where it is assumed that the initial time response of $T_e(r)$ and $n_e(r)$ is only caused by the change in input power $p_{ECRH}(r)$, and that the transport diffusion coefficients and convective terms do not change instantaneously at switch-on/off of the gyrotron. In the present analysis, we have neglected possible fast changes of $n_e(r)$ (second term in Eq.(9.1)) and the small displacement of the plasma column at switch-on and switch-off (the shift in the first 0.5 ms is typically 0.5 cm).

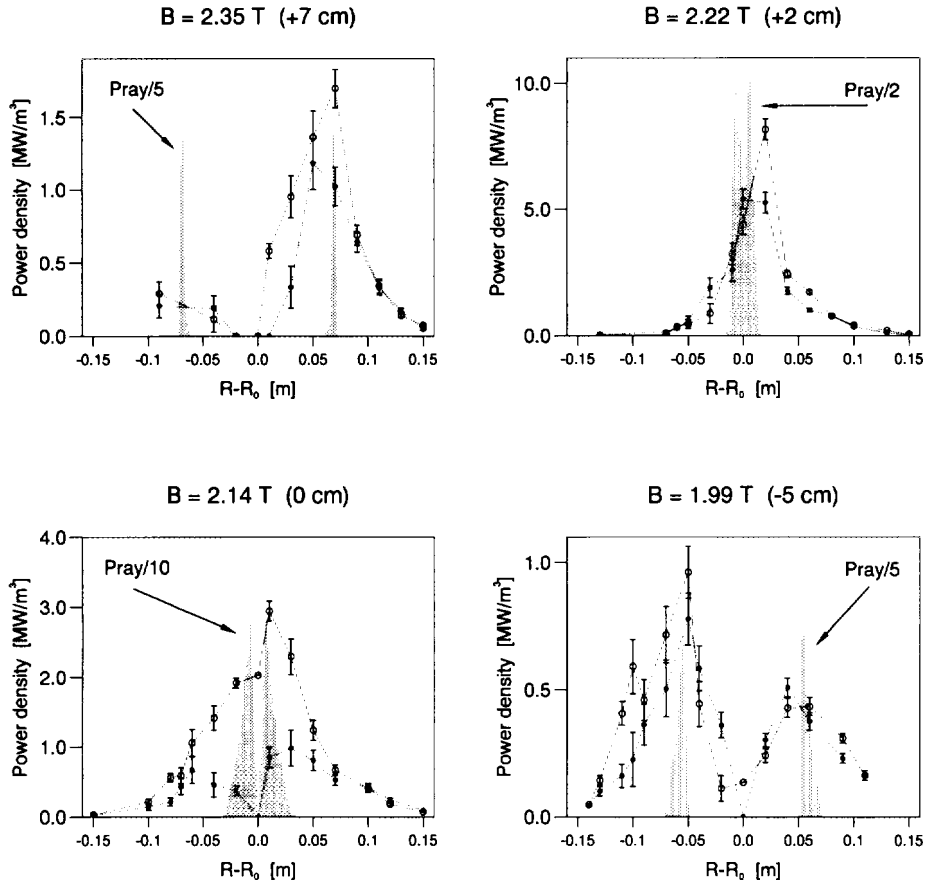


Figure 9.1: The ECRH power deposition profiles as obtained from the time response of $T_e(r)$ at switch-on (solid symbols) and switch-off (open symbols). The shaded area indicates the scaled $p_{\text{ECRH}}(r)$ from ray tracing calculations.

Figure 9.1 also shows $p_{\text{ECRH}}(r)$ obtained from ray tracing calculations, in which the steady state $T_e(r)$ and $n_e(r)$ during ECRH are included. Note that ray tracing predicts a very narrow deposition profile, because only single-pass absorption is taken into account. Absorption after multiple reflections will broaden the deposition profile. The narrowest $p_{\text{ECRH}}(r)$ is obtained at $B_T = 2.22$ T. At this resonance position the deposition is very close to the magnetic axis due to the Shafranov shift and the relativistic downshift of the absorbing electrons.

The power deposition profile measured at switch-off of ECRH is broader and higher than that measured at switch-on. Table 9.1 gives the volume integrated values for both cases, and also the single pass absorbed power from ray-tracing calculations. The single pass absorbed power is generally lower than the measured

Table 9.1: *The volume integrated power for the deposition profiles from Fig. 9.2. Also the single pass absorbed power from ray-tracing calculations is included, using the steady-state values of T_e and n_e during ECRH. The nominal input power is 180 kW.*

P_{ECRH} [kW]	Switch on	Switch off	Ray tracing
B_T			
2.35	90	118	58
2.22	130	137	132
2.14	97	157	120
1.99	67	88	57

one. The fact that at switch-off more power is found, is probably partly caused by an increase of absorption at higher T_e . Note that at switch-off P_{ECRH} is unrealistically high in the case of $B_T = 2.14$ T.

Typical profiles of the steady state $T_e(r)$ during the off-axis ECRH scan are shown in Fig. 9.2. For resonance positions $-2 < r_{\text{res}} < +5$ cm a peaked $T_e(r)$ is observed with high $T_e(0)$. For $r_{\text{res}} < -2$ and $r_{\text{res}} > +5$ cm a broadening of $T_e(r)$ is observed and, surprisingly, an enhancement on the side where $p_{\text{ECRH}}(r)$ is deposited. Note that, while generally there is good agreement between T_e [Thomson scattering] and T_e [ECE], in the case of very peaked profiles $T_e(r)$ [ECE] exceeds $T_e(0)$ [TS] significantly. The asymmetry in $T_e(r)$ is reflected in $p_{\text{ECRH}}(r)$ (Fig. 9.1), being higher at the side where ECRH is deposited, either on the low field side (LFS) or on the high field side (HFS). The asymmetry cannot be explained by

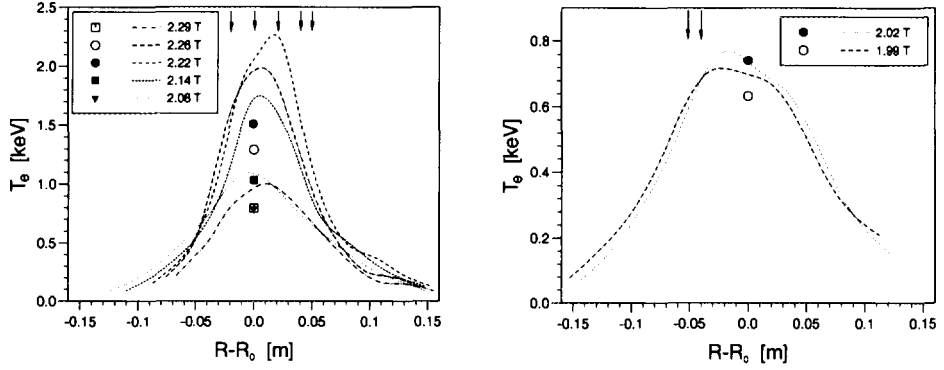


Figure 9.2: $T_e(r)$ from ECE during the ECRH resonance position scan. For $-2 < r_{\text{res}} < +5$ cm $T_e(r)$ is peaked (left graph), whereas for larger r_{res} (b) a broadening occurs (right graph), and an asymmetry in $T_e(r)$ is observed. Closed symbols (at $r = 0$) indicate single-point Thomson scattering measurements. The arrows indicate the resonance position.

relativistically downshifted suprathermal radiation from the plasma centre, which would enhance the ECE only on the low field side.

The ECRH off-axis scan was repeated after a one year shutdown, during which the RTP tokamak was upgraded, and the number of diagnostics was extended. A multi-position Thomson scattering system (TVTS) became operational [6], allowing high resolution measurement of $T_e(z)$ along a vertical chord from $z = -50$ to $+150$ mm, with $\Delta z = 1.7$ mm. In this study, the TVTS system allows a check for the calibration of the ECE in the ohmic phase on every shot. Also, an 80 channel 5 camera SXR system was installed which yield important additional information on possible asymmetries of T_e - and n_e profiles. The SXR signal is proportional to $n_e^2 T_e^\alpha$, with $\alpha \simeq 0.5$ for the range of T_e of interest here, i.e. $T_e \sim 1$ keV [7]. Moreover, the heterodyne ECE system was positioned at a new toroidal angle $\phi = 220^\circ$ relative to the LFS ECRH launcher, which used to be at 60° before the shutdown.

In a new series of experiments with the same plasma conditions, except that n_e was slightly lower ($n_e(0) = (2.5 \pm 0.3) \times 10^{19} \text{ m}^{-3}$), asymmetries are again observed in the ECE $T_e(r)$. Figure 9.3 shows examples of $T_e(r)$ at $B_T = 1.94$ and 2.04 T.

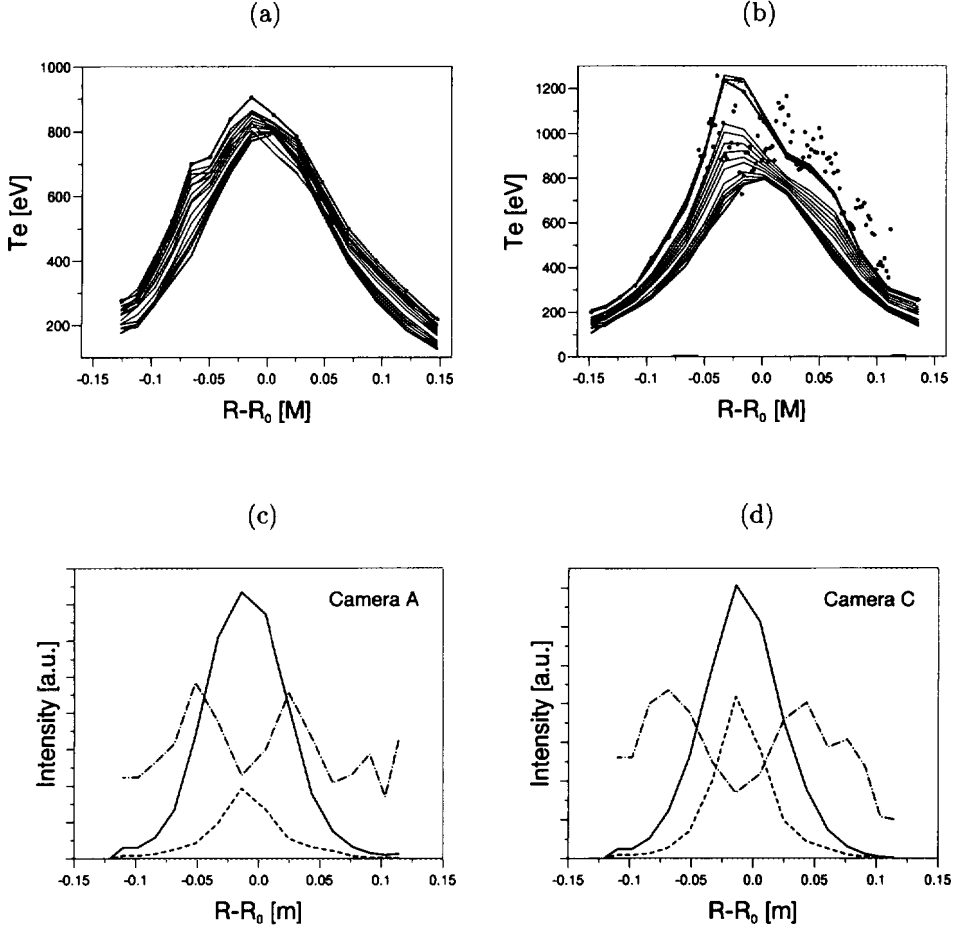


Figure 9.3: Two typical examples of the onset of asymmetries for off-axis ECRH with $B_T = 1.94$ T (a) and $B_T = 2.04$ T (b). The time interval between each curves is $\Delta t = 0.25$ ms. Also shown is the finally reached $T_e(r)$, 40 ms after switch on of ECRH. Panel (b) also shows TVTS data.

Panel (c) and (d) show the SXR emissivity profiles in the ohmic phase (*dashed line*) and during off-axis ECRH (*full line*) ($B_T = 1.94$ T). The ratio between the two intensities $I_{\text{ECRH}}/I_{\text{Ohmic}}$ is shown by the *dotted-dashed line*. Camera A gives a top view, and camera C a horizontal view in the same poloidal plane. Almost no asymmetry is observed.

As before, the measurements are reproducibly obtained, with a symmetric $T_e(r)$ in the ohmic phase and an asymmetric one during ECRH. The time development of $T_e(r)$, shows that the asymmetry develops at the same timescale as the overall development of $T_e(r)$ due to heating and diffusion. With the ECE diagnostic at the new position, a stronger enhancement of $T_e(r)$ is observed on the opposite side of r_{res} .

For only a few discharges TVTS data are available during ECRH. An example is shown in Fig. 9.3. An enhancement is observed on the low field side. The dataset is, however, too limited to conclude how the observed enhancement depends on r_{res} .

No pronounced asymmetries are observed by the SXR measurements. Figure 9.3 shows two profiles as seen from the top camera and from a camera in the equatorial plane, both at the same toroidal position ($\phi = 15^\circ$ relative to the ECRH launcher). The ratio of the signal in the ohmic phase and during ECRH shows that the increased intensity is almost symmetric with respect to the central cord. For all other off-axis experiments in this study, asymmetries were much less pronounced than the ECE measurements.

Summarizing, asymmetries are observed by ECE and, for the few measurements available, on TVTS data. SXR measurements show little asymmetry. For the ECE measurement, the character of the asymmetry depends both on the toroidal position of the ECE diagnostic, and on r_{res} . This suggests that transport along magnetic field lines, and the helicity of lines are involved. These features are now discussed in more detail.

9.3 A model

To explain asymmetries in a steady state $T_e(r)$ during off-axis ECRH, one could think of electrons that are heated at the position of the ECRH launcher, and are observed by the ECE diagnostic, before they have had interaction with the thermal bulk by collisions. Assuming the picture of nested magnetic flux surfaces, and heated electrons following magnetic field lines [2], the observed asymmetry will then depend on the helical twist of the field lines, i.e. on the q -profile, and on the toroidal position of the ECE diagnostic with respect to the ECRH launcher. Such a model, which will now be discussed in more detail, could explain why the asymmetry in $T_e(r)$ has a different character for different toroidal positions of the ECE and different values of r_{res} at the low and high field side.

Consider the low field side ECRH launcher at toroidal position $\phi = 0^\circ$. In a

poloidal cross-section, the surface at which electrons are resonantly heated is given in vertical direction by the antenna pattern of the launcher, (2.5 cm at the plasma centre) and by defraction of the rays. The resonance condition ($B_T = 2.14$ T at 60 GHz) determines the horizontal position of absorption. The horizontal width is in principle determined by the bandwidth of ECRH ($\leq 1\%$) and is broadened by absorption of downshifted suprathermal electrons. The actual dimension of the heating area is obtained from ray-tracing calculations, using the measured $T_e(r)$ and $n_e(r)$. For the conditions at hand, $dx = 0.8$ cm and $dy = 2.5$ cm.

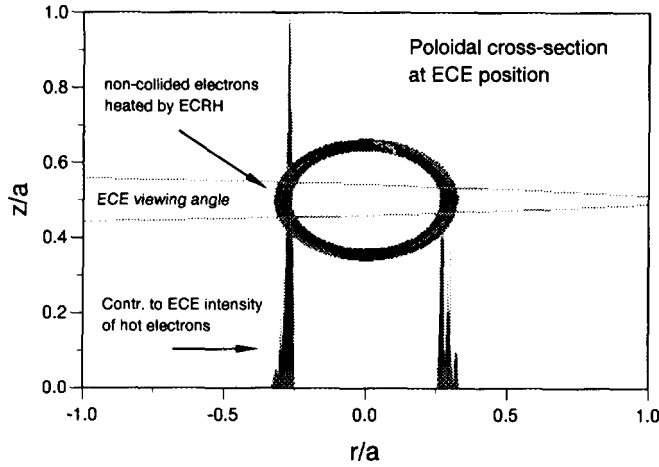


Figure 9.4: *The distribution of non-collided electrons that are heated at the position of the ECRH launcher, and are detected by the ECE diagnostic (see text). The heated area with high power density is followed 10 turns around the torus. Each time the electrons pass the ECE sight of line, they will contribute to the ECE intensity.*

In the model, the heating area at the position of the ECRH launcher is projected to the poloidal cross-section at the toroidal position of the ECE measurement ($\phi = 60^\circ$ for the first measurement series and 220° for the second). Using a fine rectangular grid (50×70 pixels), the new shape of the heated area is calculated, given the pitch of the field lines (the q -profile). The shear of the magnetic field leads to a deformation of the surface, while the total area is conserved. The thus obtained area is again transformed by going 2π in toroidal direction.

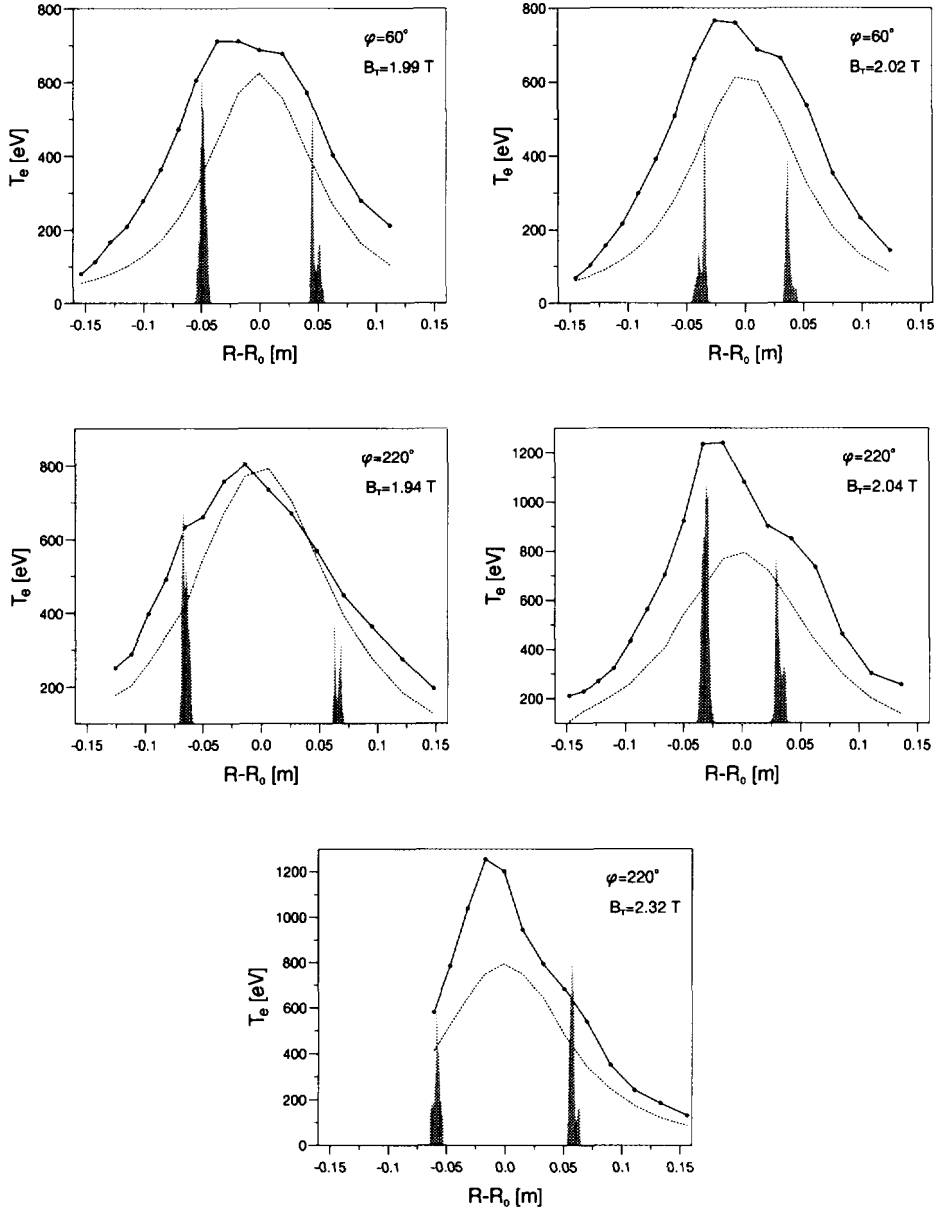


Figure 9.5: $T_e(r)$ from the 20-channel ECE at $\phi = 60^\circ$ (top) and $\phi = 220^\circ$ (bottom) during the ECRH resonance position scan. The shaded areas indicate the position of the expected additional intensity to ECE due to directly heated electrons by ECRH. The absolute scale of the shaded area is arbitrary.

After multiple turns around the torus, the surface is completely smoothed out in poloidal direction. The procedure is performed both in co- and counterclockwise direction. Figure 9.4 gives an example of the smoothing of the surface, summed over 10 turns around the torus. Also shown is the angle that is viewed by the ECE diagnostic [8], and the contribution to the ECE signal due to radiation of the suprathermal electrons.

An estimate of the poloidal distribution of suprathermal electrons is obtained by summing the distribution after N turns around the torus, multiplied by a decay function e^{-N/N_0} . Here N_0 is the number of turns a ‘hot’ electron makes before it gets lost by slowing down or radial transport. Depending on the energy of the electron [9], the slowing down process alone leads to $N_0 = O(100)$.

In the implementation of the model, the q -profile is calculated by SNAP from the current density profile that is obtained from $T_e(r)$ and the plasma resistance. Note that this leads to an ambiguity, since during ECRH $T_e(r)$ is disturbed by asymmetries. Therefore, $q(r)$ is calculated in the ohmic phase, and it is assumed that it does not change during off-axis ECRH. Using $T_e(r)$ during ECRH, by averaging over the LFS and HFS, shows that the difference in $q(r)$ compared to the ohmic one is less than 5% at the resonance position. In the numerical analysis, typical 10 turns around the torus are needed to simulate an asymmetry. Increasing this number shows that the intensity on both LFS and HFS increases, and that the asymmetry disappears. Figure 9.5 shows a number of $T_e(r)$ for various B_T , and the predicted additional intensity due to directly heated electrons, as modelled by the above mentioned procedure. It is seen that the position of the enhancement of $T_e(r)$ is well predicted by our simulations for the measured asymmetric $T_e(r)$ before as well as after the shutdown of RTP. Note, however, that the results depend critically on the q value at the resonance position, and on the shear. A slight change in these parameters, can modify the predicted enhancement seriously.

Figure 9.6 shows a comparison of the expected ECE intensity for different values of magnetic shear ($q' = \partial q / \partial \rho$), and for different rational q -surfaces. From the q -profile calculated by SNAP, typically $q' \sim 2$. At this shear level, differences between LFS and HFS are smoothed out quickly, typically after 10 times around the torus. By reducing the shear, a much stronger asymmetry can be maintained. This is especially true near rational q -surfaces with an odd m -number. In this case, the ‘band of suprathermal electrons’ can pass one side of the torus many times, without reaching the other side. Now, $N \geq 100$, which is more realistic with respect to slowing down or radial transport of electrons, and the number of times an electron

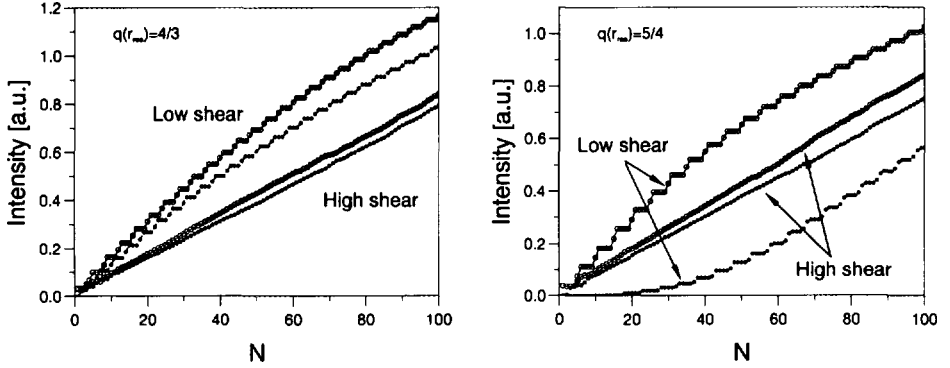


Figure 9.6: A comparison of the expected ECE intensity due to bands of suprathermal electrons on the low field side (open symbols) and high field side (solid symbols). From the q -profile calculated by SNAP, it follows that $q' \simeq 2.4$ (high shear). The figure also shows cases for low shear ($q' = 0.1$). In the latter case, a much stronger asymmetry can be maintained. Conditions are: $q(r_{\text{res}}) = 4/3$ and $5/4$, and $B_T = 2.04$ T. For this figure, the decay function e^{-N/N_0} has been omitted in the calculation.

has to pass the heating volume to become suprathermal.

9.4 Results and Discussion

In this chapter off-axis ECRH experiments are reported. The position scan shows that best absorption takes place with $r_{\text{res}} = +2$ cm, where the deposition is very close to the magnetic axis due to the Shafranov shift and the relativistic downshift of the absorbing electrons. In this case $p_{\text{ECRH}}(r)$ is very peaked (Fig. 9.1). The estimated ECRH deposition profiles obtained at switch-on and switch-off are different. At switch-off, $p_{\text{ECRH}}(r)$ is higher and contains more power. Apparently, the change in T_e is not only caused by switch-off of the heating source. Other studies on RTP [9, 10] show that ECRH can have a strong effect on transport (either conductive or convective) on a fast timescale. It is well possible that these effects blur the measurement of $p_{\text{ECRH}}(r)$ from $\partial T_e(r)/\partial t$ analysis.

The off-axis heating experiments show that asymmetric steady-state $T_e(R)$ profiles are reproducibly obtained for $-2 < r_{\text{res}} < +5$ cm. The asymmetry in $T_e(r)$ is observed by heterodyne ECE measurements. Unfortunately, no extended dataset

of TVTS measurements is available in these experiments, but there are indications (also from other experiments) that also $T_e(z)$ measured by TVTS shows an asymmetry. SXR measurements give fairly symmetric profiles for all values of r_{res} . Note, however, that the SXR intensity is only a weak function of T_e .

Experiments were done with two different toroidal positions of the ECE diagnostic. In both cases, the asymmetries in the ECE $T_e(R)$ can be explained qualitatively by a simple model based on transport of heated electrons along magnetic field lines. The model is very crude in that it makes a number of assumptions. We briefly discuss the most important of these. In the model, the role of trapped particles is neglected. They could well possibly be responsible for an enhancement of T_e on the low field side. However, they cannot explain a simultaneous enhancement on the high field side. Also, we only looked at the position of the enhancement, and the *relative* intensity of the contribution of 'hot' electrons. In a more profound analysis the absolute value should be considered.

The observed asymmetry strongly depends on the magnetic shear. With a smooth q -profile as assumed in the model, the poloidal asymmetry is already washed out after 10 toroidal revolutions. The results of Fig. 9.5 are only obtained if the decay function e^{-N/N_0} is included with $N_0 = 7$. The mean free path of heated electrons is, however, in the order of hundreds of toroidal revolutions, which makes the asymmetry hard to understand. It was found that for low shear values, i.e. shear plateaus around rational q -values, much stronger asymmetries can be maintained. These shear plateaus could be possibly related to (small) magnetic islands, and/or an ergodization of rational q -surfaces. Shear plateaus are also involved to explain striations observed with pellet injection [11].

In summary, it is shown that with a simple model the observed asymmetries could well be caused by a 'band of suprathermal electrons', heated by the gyrotron, that is observed by ECE. Based on geometric arguments (the q -profile, and the toroidal position of the ECE diagnostic) the enhancements in T_e can be tentatively explained.

Since the enhancement is not caused by a change in the bulk temperature, care must be taken when using the ECE $T_e(R)$, under these conditions, for transport analysis.

References

- [1] KONINGS J.A., SEGERS R.A., HOGWEIJ G.M.D., LOPES CARDOZO N.J. and the RTP team (1993) Proc. Workshop on Local Transport Studies in Fusion Plasmas, Varenna Vol. ISPP-14, Soc. Italiana di Fisica, Bologna 45.
- [2] DENDY R.O. (1985) *Plasma Phys. and Contr. Nucl. Fus.* **27**, 1253.
- [3] DONNÉ A.J.H. and the RTP team (1994) *Fizika Plazmy* **20**, 206.
- [4] TOWNER H.H. and GOLDSTON R.J. (1984) *Bull. Am. Phys. Soc.* **29**, 1305.
- [5] JANICKI C. (1993) *Nucl. Fusion* **33**, 513.
- [6] LOPES CARDOZO N.J., SCHÜLLER F.C., BARTH C.J., CHU C.C., PIJPER F.J., LOK J. and OOMENS A.A.M. (1994) *Phys. Rev. Lett.* **73**, 256.
- [7] FERREIRA DA CRUZ D. (1994) *private communication*.
- [8] VAN GELDER J.F.M., HUSMANN K.C.E., MIEDEMA H.S. and DONNÉ A.J.H. (1994) accepted for publication in *Rev. Sci. Instrum.*
- [9] Chapter 7 of this thesis.
- [10] KONINGS J.A., HOGWEIJ G.M.D., LOPES CARDOZO N.J., OOMENS A.A.M., SCHÜLLER F.C. and the RTP team (1994) *Plasma Physics and Controlled Fusion* **36**, 45.
- [11] DUBOIS M.A., PÉGOURIÉ B., SABOT R. and HOANG G.T. (1992) Proc. 19th Eur. Conf. on Contr. Fusion and Plasma Phys., Innsbruck, Vol. I p.103.

Chapter 10

Evaluation and Discussion

In this thesis transport analyses have been reported of plasmas with ohmic heating, with CW and modulated ECRH and with a scan of Z_{eff} . The main conclusions are briefly summarized in Section 10.1. In Section 10.2 a discussion is given of the intriguing observations that were made during ECRH. Specifically, the following questions are addressed: (i) is the improvement of confinement during ECRH caused by a lower value of the thermal diffusion coefficient or do convective terms play a role, and (ii) what process causes the improvement of confinement.

For a discussion of the results of the Z_{eff} scan, and the comparison with transport models, the reader is referred to Chapter 8 of this thesis.

The recent observation of filamentary structures in RTP can have important consequences for the interpretation of the results in this thesis. This subject is discussed in Section 10.3.

Finally, in the last section, some recommendations are made for further transport studies in the near future of RTP.

10.1 Summary of experimental findings

This thesis dealt with the analysis of anomalous transport in the RTP tokamak. The main results can be summarized as follows:

1. For ohmic plasmas the scaling of τ_E is consistent with observations in other devices: τ_E scales linearly with n_e , and saturates at higher densities. The electron collisionality is below unity in $q_a \leq 4$ plasmas, and has a value between 2 - 10 for high q_a plasmas. Hence, collisional transport in RTP is close to the transition between the banana and plateau regime.
2. A scan of Z_{eff} from 1.5 to 9.8 results in only a marginal change in τ_E and χ_e in ohmic and ECR heated discharges. Scaling with collisionality gives $\chi_e \sim \nu_e^{*0.4}$ in the ohmic plasmas, and no scaling ECRH plasmas due to a limited ν_e^* range. A comparison with transport models gives a significant correlation in ohmic plasmas for the driftwave model of WEILAND, the model of OHKAWA based on current filamentation, and COPPI, MAZZUCATO, GRUBER based on profile consistency. During ECRH, the predictions of two models appear to correlate with the experimental dataset: the trapped ion driven mode of DIAMOND, BIGLARI and the drift mode for untrapped electrons of SIMILON, DIAMOND. There is no model that predicts the observed χ_e *both* in ohmic plasmas and during ECRH.
3. On-axis ECRH leads to narrow and very peaked $T_e(r)$ with high T_e on axis. An ECRH power scan shows that τ_E improves when low power ECRH is applied. τ_E decreases for increasing P_{ECRH} .
4. The improvement of confinement is studied in more detail by a scan of the ECRH power achieved by fast modulation of the gyrotron. A characteristic time of 0.12 ms can be associated with the improvement of τ_E . This suggests that a suprathermal electron population of 5 to 10 keV, sustained by ECRH, plays a role in the improvement of τ_E .
5. A scan of the ECRH resonance position results in asymmetric steady state $T_e(R)$ measured by ECE. A tentative analysis shows that transport of suprathermal electrons along magnetic field lines can explain the observed asymmetries.

10.2 Impact of ECRH on transport

One of the intriguing results reported in this thesis is the reduction of transport during ECRH. Two important observations were made: (i) χ_e^{pb} is reduced comparing the ohmic target plasma and 60 kW ECRH, but (ii) further increase of P_{ECRH} leads to an increase of χ_e^{pb} . These observations give rise to the following questions:

1. Can it be empirically confirmed that the improved confinement is caused by a lower value of the thermal diffusion coefficient or do convective terms play a role ?
2. Why is the improvement lost with increasing ECRH power?
3. What is the physical mechanism behind either a lower thermal diffusivity or a higher convective term?

For these questions, we will discuss the evidence that can be extracted from transport studies at RTP. We start with the first question.

In the local power balance analysis, q_e and ∇T_e are established, which yield, by definition, χ_e^{pb} . To interpret χ_e^{pb} as the thermal diffusion coefficient, one must assume that off-diagonal terms in the transport matrix are small. This is not true when strong components, other than the ∇T_e driven flux, contribute to the heat flux. Then, the diffusive and non-diffusive components to q_e cannot be separated. If, however, measurements of χ_e^{pb} are available for several plasma conditions, the two components can in principle be quantified. Additional information can be obtained from dynamic transport experiments, in which only the diffusive flux is measured.

Figure 10.1 gives a schematic of the transport studies reported in this thesis. Three relationships between q_e and ∇T_e are possible: an offset linear relation (Fig. 10.1a), a nonlinear relation with zero offset (Fig. 10.1b), and an offset nonlinear relation. In ohmically heated plasmas (Chapter 5), q_e and ∇T_e cannot be varied much at constant I_P . The heat flux was only marginally scanned by changing the ohmic input power via Z_{eff} (Chapter 8). Scanning the power of on-axis ECRH results in large changes in q_e while ∇T_e steepens, most dramatically near the deposition region. During low power ECRH, the plasma reaches another ‘mode’, the improved confinement regime (Chapter 6). It is clear that the two measurements of χ_e^{pb} in ohmic and during ECRH cannot lie on the same q_e vs. ∇T_e curve, since the transition is characterized by a decrease in q_e and an increase in ∇T_e .

In case of an offset-linear relationship, improvement of confinement is reflected by a different offset of the q_e vs. ∇T_e curve. This could, for example, be caused

by an inward heat flux which is not driven by ∇T_e . In case of a nonlinear relation between q_e and ∇T_e (Fig. 10.1b), the same data are interpreted as χ_e being reduced to reach improvement of confinement.

The transition to the improved confinement mode was the subject of Chapter 7. A further reduction of q_e , achieved by modulated ECRH, showed a smooth transition from the ohmic regime to the ECRH heated regime. It is possible that the plasma is switched between two modes and the time averaged analysis yields an intermediate value. For this hypothesis, the improvement of confinement would have to occur on a very fast time scale. In Chapter 7 it was also found that the improvement occurred over the full plasma radius, also outside the ECRH deposition region. This means that, whether the reduction of χ_e^{pb} is due to an inward heat flux or to a reduced χ_e , the change (i) happens on a fast time scale and (ii) extends over the whole plasma.

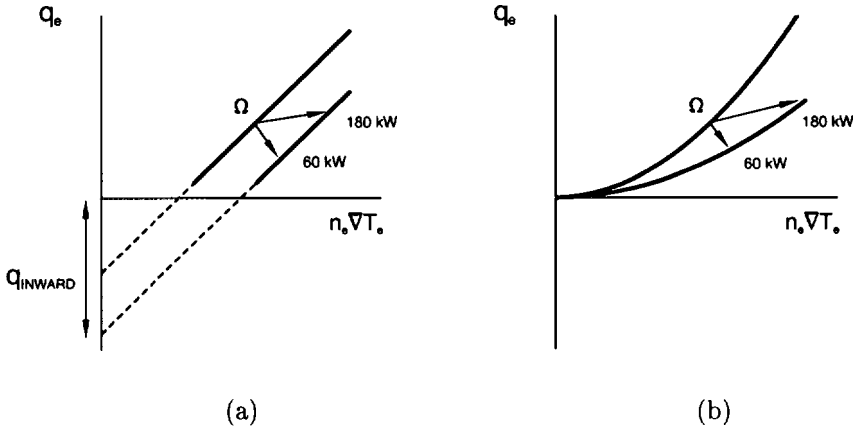


Figure 10.1: Schematic of the heat flux q_e versus $n_e \nabla T_e$. Two possible scalings are drawn: (a) offset-linear and (b) nonlinear. The ECRH experiments presented in this thesis are schematically indicated.

An instantaneous change of χ_e over the entire plasma column is a puzzling phenomenon, because it needs a mechanism that propagates very rapidly. E.g., if a change in the q -profile is responsible, the change will occur on the slow time scale

of the current diffusion time. Fast changes in χ_e over the full plasma radius have also been observed in ECRH experiments in W7-AS [1]. Since externally induced currents do not play a role in a stellarator, one has to exclude a change in magnetic configuration. Any explanation invoking suprathermal electrons also suffers from the timescale that is needed for the diffusion of these.

Evidence for an inward heat flux was obtained in experiments at DIII-D [2]. During off-axis ECRH, a peaked $T_e(r)$ was observed which is sustained by an inward electron heat flux. Although in this case the inward flux does not extend over the full plasma, but occurs inside the deposition region, again it remains an open question what mechanism can switch a pinch term on a fast timescale.

Transient transport analyses at RTP [3] indicate that the offset linear model (Fig. 10.1a) is more realistic than the non-linear scaling. This result is obtained from the incremental diffusivity ($\chi_e^{\text{inc}} = -\partial q_e / \partial(n_e \nabla T_e)$), which is deduced from the propagation of T_e -perturbations induced by the sawtooth instability or by modulated ECRH. It was found that χ_e^{inc} is independent of input power (or T_e) under many different plasma conditions ($q_a = 3.2 - 5.1$, $n_e(0) = (2.0 - 3.0) \times 10^{19} \text{ m}^{-3}$, and $Z_{\text{eff}} = 2 - 5$). This provides evidence that the relation between q_e and $n_e \nabla T_e$ is linear. Moreover, from the steady state power balance analysis (Chapter 6) it was found that increasing P_{ECRH} from 60 to 180 kW, showed an increase of both q_e and ∇T_e , at a ratio that is the same as was found in transient transport studies. Furthermore, the constant value of χ_e^{inc} is consistent with the observation that at increasing additional power χ_e increases.

Note that in case of an inward pinch term, the associated inward heat flux can be 50% of q_e itself at $r/a = 0.5$, given the incremental heat diffusivity from perturbative transport studies. The q_a scan (Chapter 6), showed that the improvement in τ_E is less pronounced at low q_a , thus at higher P_{OH} . This could be explained if at higher ohmic power the relative contribution of e.g. an ECRH induced inward heat flux is smaller.

The cause of the improvement of confinement is still an open question. Most evidence points at the direction of a change in inward heat pinch, but a change of χ_e itself cannot be ruled out. From the Z_{eff} scan (Chapter 8), it was concluded that ohmic and ECR heated plasmas are in different transport regimes, depending on whether ν_e^* exceeds unity or not. In the first case, in ohmic discharges, χ_e^{pb} scales weakly with Z_{eff} but more strongly with the collisionality. During ECRH, χ_e^{pb} also scales weakly with Z_{eff} . In this case, ν_e^* was not varied sufficiently to be used as

a scaler. The difference between the ohmic and ECRH scaling was related to the different regimes of collisionality. In the banana regime, transport would be reduced e.g. by a large fraction of trapped particles that are created by ECRH. Note that the poor correlation between the experimental dataset and the predictions of transport models in both ohmic *and* ECRH conditions is not surprising. Most models give a single relation between q_e and ∇T_e , and the transition between two different regimes is not accounted for.

From the ECRH frequency scan in Chapter 7 the time scale at which the improvement occurs was found to be in the order of $120 \mu\text{s}$. This time could be related to the slowing down time of suprathermal electrons with an energy of 5 to 10 keV.

In conclusion, the Z_{eff} scan shows that a different regime with trapped particles is reached, while the modulation experiments point at suprathermal electrons. This suggests that a suprathermal population of trapped particles plays a role in the improvement of confinement.

10.3 Plasma filamentation and the relation to this thesis

In this thesis transport analysis has been carried out under the usual assumption that the magnetic equilibrium consists of nested toroidal flux surfaces, which are isothermals and isobars.

Recent experiments in the RTP tokamak have shown that the magnetic topology is more complex [4]. Detailed measurements of $T_e(r)$ showed small steps and bumps, which were interpreted as evidence for regions of stochastic field, separated by ‘good’ surfaces. With central ECRH, further departure of the standard picture was found. In the heating volume, several tubes of high T_e and pressure (filaments) were demonstrated. At $r/a \approx 0.2$ a very steep gradient of T_e is found, across which electron thermal transport is reduced to the neoclassical level. Hence, the overall picture is that in the centre several flux tubes form, so that here the poloidal symmetry is broken altogether. This small central region is bounded by a thin, poloidal shell of very low transport. Outside that, the profiles show a fair degree of poloidal symmetry. Not yet measured, but very likely in the view of measurements of density fluctuations in many tokamaks, is that the topology is subject to small scale fluctuations in the frequency range 10 – 100 kHz.

These observations raise the following questions concerning the work presented

in this thesis:

1. If the flux surfaces are broken, is the 1-D transport analysis still meaningful? and if so:
2. (a) Can the concept of broken flux surfaces help to understand the experimental results, or conversely,
(b) Is there evidence in the data presented here that can confirm or contradict the picture of broken flux surfaces?

To answer the first question: Clearly in the centre of the plasma, where several flux tubes can form, a 1-D analysis is not meaningful. However, this affects only the inner 20% of the minor radius, and this region has already been excluded from analysis for other reasons, namely that the evaluation of the fluxes and gradients is too uncertain. Outside this central region, measurements show that the profiles do have a high degree of poloidal symmetry, so that poloidal averaging is still allowed. This means that χ_e^{pb} is a well defined quantity characterizing the radial thermal transport. However, care should be taken with the interpretation of this quantity. Firstly, if the heat flux is a strongly varying function of the poloidal angle (i.e. the energy oozes out at a few 'leaky spots') then the transport coefficients at those leaks cannot be simply related to χ_e^{pb} . Secondly, if the thermal diffusivity $\chi_e(r)$ in the plasma were a strongly varying function of the minor radius, χ_e^{pb} would represent the harmonic radial average of $\chi_e(r)$: $\chi_e^{\text{pb}} = \langle \chi_e^{-1} \rangle^{-1}$. This means that χ_e^{pb} is strongly biased towards the lower values of $\chi_e(r)$. Finally, if the structure is fluctuating, transport may be of a percolative nature. This, too, means that one cannot simply equate a turbulent diffusion coefficient to χ_e^{pb} .

In summary, the plasma exhibits sufficient poloidal symmetry to make χ_e^{pb} a useful quantity to characterize radial thermal transport. If there are fluctuating fine structures in the plasma, the averaging over poloidal angle, radius and time has as a result that the link with the local transport coefficients is totally lost. This is not a problem in empirical transport studies, where one can study the behaviour of χ_e^{pb} as function of various plasma parameters. However, when comparing measured values of χ_e^{pb} to theoretical expressions which have not been averaged in the same way, no success may be expected. In fact, this may be a partial explanation of the lack of correlation between theoretical transport models and experimental data which is generally found in the literature, and also in Chapter 8 of this thesis.

As to the question whether the filamentation hypothesis can help to understand the experimental findings presented in this thesis, or vice versa, the following ob-

servations apply. One of the most striking experimental results is that the improvement of confinement upon switching on ECRH appears to occur ‘instantaneously’ throughout the plasma. This phenomenon of ‘globally controlled local transport’ is very difficult to accomodate in traditional transport models. These require changes of local variables such as the magnetic shear to change the transport, and such changes propagate through the plasma on the time scale of the energy confinement time or more slowly. However, in a plasma with broken flux surfaces, the transport is determined by the measure of destruction of the surfaces. This is determined by the subtleties of poloidal distribution of current density, pressure, plasma flow and electric fields. Changes in this balance could be envisaged to propagate on a much shorter time scale than changes in the global profiles of e.g. the current density.

In Section 10.2 it was hypothesized that an inward convective heat flux is the cause of the improved confinement under ECRH. It may be noted that a theoretical treatment of current filamentation by TAYLOR [5] does predict an inward heat flux, driven by the gradient of the current density. However, the theory is not sufficiently detailed to account for trapped or untrapped suprathermal electrons. Also noteworthy is that one of the models tested in Chapter 8 which showed reasonable correlation with the experimental dataset for ohmic plasmas, the OHKAWA model, is based on current filamentation.

The data presented in this thesis are mainly time averaged measurements of steady state plasmas, with limited spatial resolution. Under these conditions no direct evidence for a complex magnetic topology may be expected. One exception is formed by the measurements of asymmetric ECE profiles under off-axis ECRH (Chapter 9). A model was presented that showed that the location of the asymmetries at two toroidal angles could be understood on the basis of suprathermal electrons following field lines. However, the strength of the effect strongly depends on the magnetic shear. With a smooth q -profile as assumed in the model, the poloidal asymmetry is already washed out after 10 toroidal revolutions. In this case the measured asymmetry is hard to understand, in view of the mean free path of hundreds of toroidal revolutions, and the fact that an electron has to pass the heating volume many times to become significantly suprathermal. However, if the flux surfaces with rational q are degenerated into poloidal shells of stochastic field, this implies the existence of a stair-step q -profile, i.e. shear plateaus around rational q -values. In such a system much stronger asymmetries can be maintained.

10.4 Recommendations for future research

In the near future, an extension of the q_e vs. ∇T_e map is recommended to both sides of the parameter regime that was explored in this thesis. Extension to higher q_e would confirm if q_e vs. $n_e \nabla T_e$ is indeed linear. The low- q_e region, which can be reached in the plasma centre by high power off-axis ECRH, could reveal if indeed the scaling is offset-linear or nonlinear. With the new gyrotron park at RTP ($P_{\text{ECRH}} \geq 500$ kW) both limits can be investigated. Furthermore, using $2\omega_{ce}$ (110 GHz), higher n_e can be reached, allowing the study of L-mode scaling at RTP in comparison with the linear and saturated ohmic confinement regimes as presented in this study.

The mechanism behind improvement of confinement during ECRH can become more clear from the measurement of $j(r)$. Using the 19-channel polarimeter, which will come into operation in the end of 1994, better determination of $q(r)$ is possible. This will demonstrate if reduced transport is accompanied by a change in magnetic shear.

Preferably, a time dependent local power balance should be performed to obtain $\chi_e(r, t)$, to see if the decrease in χ_e occurs instantaneously over the full plasma radius after switch-on of ECRH, or if χ_e is initially low in the centre only, and gradually also decreases at the edge as function of time.

The role of a suprathreshold population as driving the improvement of confinement can be quantified by a scan of Z_{eff} at low power ECRH. At increasing Z_{eff} , the slowing down time decreases and a higher ECRH threshold power might be necessary to sustain the population, thus to reach improvement of confinement.

The observation of asymmetric $T_e(r)$ was explained in Chapter 9 by a basic model with a number of assumptions that should be taken into account in a more refined analysis. In experimental conditions, a current scan will demonstrate whether, given the pitch of the field lines, indeed a hot helical band of electrons is observed by ECE.

Finally, as was discussed in Section 10.3, the existence of filamentary structures can have important consequences for transport studies. It is an exciting prospect that the measurements of filamentation, and detailed transport studies, and the theory of partially ergodic magnetic fields will result in a consistent picture of transport in tokamak plasmas.

References

- [1] STROTH U. *et al.* (1993) Proc. Workshop on Local Transport Studies in Fusion Plasmas, Varenna, Vol. ISPP-14, Soc. Italiana di Fisica, Bologna 161.
- [2] LUCE T.C., PETTY C.C. and DE HAAS J.C.M. (1992) *Phys. Rev. Lett.* **68**, 52.
- [3] HOGEWELJ G.M.D., DE LUCA F., GORINI G., JACCHIA A., KONINGS J.A., LOPES CARDOZO N.J., MANTICA P., PETERS M. and the RTP team (1994) Workshop on Transport in Fusion Plasmas, Aspenäs, Göteborg.
- [4] LOPES CARDOZO N.J., SCHÜLLER F.C., BARTH C.J., CHU C.C., PIJPER F.J., LOK J. and OOMENS A.A.M. (1994) *Phys. Rev. Lett.* **73**, 256.
- [5] TAYLOR J.B. (1993) *Phys. Fluids B* **5**, 4378.

Summary

The process of fusion of small nuclei thereby releasing energy, as it occurs continuously in the sun, is essential for the existence of mankind. The same process applied in a controlled way on earth would provide a clean and an abundant energy source, and be the long term solution to the energy problem. Nuclear fusion requires an extremely hot (10^8 K) ionized gas, a plasma, that can only be maintained if it is kept insulated from any material wall. In the so called 'tokamak' this is achieved by using magnetic fields.

The thermal insulation, which is essential if one wants to keep the plasma at the high 'fusion' temperature, can be predicted using basic plasma theory. A comparison with experiments in tokamaks, however, showed that the electron energy losses are ten to hundred times larger than this theory predicts. This 'anomalous transport' of thermal energy implies that, to reach the condition for nuclear fusion, a fusion reactor must have very large dimensions. This may put the economic feasibility of fusion power in jeopardy. Therefore, in a worldwide collaboration, physicists study tokamak plasmas in an attempt to understand and control the energy losses. From a scientific point of view, the mechanisms driving anomalous transport are one of the challenges in fundamental plasma physics. In Nieuwegein, a tokamak experiment (the Rijnhuizen Tokamak Project, RTP) is dedicated to the study of anomalous transport, in an international collaboration with other laboratories.

In an ideal transport study experiment, one plasma parameter is varied and the effect on transport is measured. This thesis reports on parameter scans in RTP, performed to characterize the thermal energy diffusion. Experiments are reported that provide better insight in the processes that enhance transport in tokamak plasmas.

One parameter scan involves the effective ion charge, Z_{eff} , which is a measure for the contamination of the plasma. Thus, in RTP plasmas were deliberately contaminated, but in a controlled manner. Although the experiment seems simple, in practice it needs considerable tuning to perform a single parameter scan with Z_{eff} . This may be the reason why it has not been attempted yet in other devices.

In plasma physical terms a change in Z_{eff} means that the collision frequency of electrons and ions is changed, which can have important consequences for transport. The result, however, showed no dependence of the electron thermal transport on Z_{eff}

(28.1 WL)

or the absolute collision frequency. However, we did demonstrate a clear dependence of the thermal diffusivity on the normalized collision frequency, the collisionality. A comparison was made with the prediction of various transport models, based on various underlying mechanisms. Interestingly, they show a markedly different dependence on Z_{eff} . The strategy was that the Z_{eff} dependence found experimentally was compared to the prediction of models. This could exclude some of the mechanisms as a viable explanation for anomalous transport. Although in certain plasma conditions agreement was found between model and experiment, there was no model that predicted all observations. The disagreement between transport models and extensive datasets is commonly found in literature.

Another parameter scanned in this study was the level of heating (the power) of the plasma. It was observed that, for certain conditions, a reduction of transport occurred, when additional heating using microwaves was applied. Given this observation, the reduction was studied in more detail by switching the microwave power on and off many times (modulation) at a repetition rate so fast that the plasma could hardly distinguish between continuous or modulated operation of the source. By scanning the modulation frequency, it was concluded that electrons with an energy of three times the thermal bulk are probably involved in the reduction of thermal transport. It was also found that the reduction occurs on a very short timescale and extends far outside the region where the highly energetic electrons are created.

A scan in the position of the microwave power deposition led to the observation of apparently asymmetric temperature distributions. The measurements could be explained by the existence of bands of highly energetic electrons that were heated by the microwaves. These asymmetries are at variance with the assumptions that lie on the basis of the tokamak equilibrium. It is an indication that the magnetic topology more complex than is generally assumed.

Samenvatting

Het proces van samensmelten van twee atoomkernen waarbij energie vrijkomt, zoals dat in de zon gebeurt, is essentieel voor het bestaan van de mens. Indien het zelfde proces van kernfusie op beheersbare wijze zou kunnen worden toegepast op aarde, dan zou dat een schone en overvloedige energiebron zijn, welke het energieprobleem op lange termijn kan oplossen. Om kernfusie te bereiken, is een extreem heet (10^8 K) geïoniseerd gas nodig, een plasma, dat alleen kan blijven bestaan indien het geïsoleerd is van zijn materiële omgeving. In een zogeheten 'tokamak' wordt dit bereikt door middel van magnetische velden.

Met fundamentele plasma theorie kan worden berekend hoe goed de thermische opsluiting moet zijn om de hoge 'fusie' temperaturen te bereiken. Een vergelijking met experimenten in tokamaks laat echter zien dat de energieverliezen via de elektronen een factor tien tot honderd keer hoger zijn dan wordt voorspeld door de theorie. Dit 'anomaal transport' van warmte is er de oorzaak van dat een tokamak zeer grote afmetingen moet hebben om kernfusie te bereiken. Hierdoor staat de economische haalbaarheid van een commerciële fusiereactor ter discussie. Daarom worden, in een wereldwijd samenwerkingverband, tokamakplasma's onderzocht in een poging om de energieverliezen te begrijpen en te beheersen. Wetenschappelijk gezien vormen de aandrijvingsmechanismen van anomaal transport één van de meest uitdagende aspecten van het fundamentele plasmafysische onderzoek. Een tokamak experiment in Nieuwegein (het Rijnhuizen Tokamak Project, RTP) richt zich, in samenwerking met buitenlandse laboratoria, op het onderzoek naar anomaal transport.

In het ideale experiment om transport te bestuderen, wordt slechts één parameter gevarieerd, en de resulterende verandering in transport gemeten. In dit proefschrift worden een aantal parameter scans beschreven, welke tot doel hebben het energietransport in RTP te karakteriseren. De experimenten geven een beter inzicht in de processen welke ten grondslag liggen aan het verhoogde transport in tokamakplasma's.

In één van de experimenten werd de effectieve ionenlading, Z_{eff} , gevarieerd. Deze parameter is een maat voor de vervuiling van het plasma. Aldus werden in RTP plasma's opzettelijk, maar gecontroleerd, verontreinigd. Het experiment lijkt eenvoudig om uit te voeren, maar in de praktijk is een aanzienlijke inspanning vereist om

alleen Z_{eff} te variëren. Wellicht daarom is het experiment nog nooit eerder verricht in andere opstellingen.

Een verandering van Z_{eff} betekent in plasmafysische termen dat de botsingsfrequentie van elektronen en ionen wordt veranderd, hetgeen belangrijke gevolgen kan hebben voor het transport. Er bleek echter geen afhankelijkheid te zijn van het warmtegeleidingsvermogen op Z_{eff} en de botsingsfrequentie. Wel kon een directe afhankelijkheid worden aangetoond van de warmtegeleiding op de genormeerde botsingsfrequentie: de botsingsgraad. Er werd een vergelijking gemaakt met de voorspelling van diverse transportmodellen, welke gebaseerd zijn op verschillende onderliggende mechanismen en, verrassend genoeg, verschillende afhankelijkheden hebben met Z_{eff} . Dit leidde tot de strategie om de experimenteel gevonden afhankelijkheid van Z_{eff} te vergelijken met voorspellingen van transportmodellen. Hierdoor zouden enkele van deze mogelijke mechanismen van anomaal transport kunnen worden uitgesloten. Voor sommige plasma condities werd een overeenstemming gevonden tussen model en experiment. Er was echter geen model dat een goede beschrijving gaf van alle metingen. De discrepantie tussen modellen en uitgebreide datasets is al vaker beschreven in de literatuur.

Een andere parameter die werd gevarieerd was de mate van plasmaverhitting (het vermogen). Onder bepaalde condities, waarbij microgolven werden gebruikt voor extra verhitting, werd een afname van transport gemeten. Deze afname werd meer gedetailleerd bestudeerd door het microgolfvermogen snel aan en uit te schakelen (modulatie), zodanig dat het plasma bijna geen verschil kon merken tussen gemoduleerde of continue verhitting. Door de modulatiefrequentie te variëren, kon worden bepaald dat elektronen met een energie die twee- tot driemaal hoger is dan de thermische energie van de bulk, betrokken zijn bij de afname van transport. Tevens werd gevonden dat de afname op een zeer korte tijdsschaal plaats vindt, en dat het effect zich uitstrekt tot buiten het gebied waar de hoog-energetische elektronen worden gecreëerd.

Een verandering in de positie waar microgolfvermogen wordt geabsorbeerd, gaf aanleiding tot een schijnbaar asymmetrische temperatuurverdeling. Deze metingen konden worden verklaard door de aanwezigheid van een band van hoog-energetische elektronen, die zijn gecreëerd door de microgolven. Deze asymmetriën zijn in tegenspraak met de aannames die ten grondslag liggen aan het evenwicht in een tokamak. Zij vormen een aanwijzing dat de magnetische topologie ingewikkelder is dan aanvankelijk werd aangenomen.

Dankwoord

“Rijnhuizen” is een geweldige plek om te werken. Niet alleen het park en de omgeving, maar vooral ook het team van mensen die maken dat Rijnhuizen méér is dan een saai onderzoeksinstituut. De dagelijkse propvolle kantine tijdens de koffiepauze, de OVR activiteiten, de Intercom, het Sinterklaascabaret en Rijnhuizen café: in de toekomst zal ik ze missen. Het verrichten van onderzoek aan een grote machine betekent dat samenwerking noodzakelijk is, en niet alleen van 9 tot 5. Mijn dank gaat uit naar iedereen die zijn bijdrage heeft geleverd aan de diverse “Koningsprogramma’s”. Ook de ondersteuning van het secretariaat en de tekenkamer waren van belang. Er zijn veel mensen die hebben bijgedragen tot het welslagen van mijn promotietijd. Een aantal wil ik met name noemen.

Niek (toch niet alwéér een blikje Sisi); Dick (jemig de pemig, als een speer aan het werk!); Machiel (ja, ik kom zo lunchen, even mijn 32 fotorolletjes volschieten); Michiel (Unigrap is tòch mooier); Atila (waar is het dichtsbijzijnde postkantoor?); Boudewijn (voor het terugvinden van artikelen op je eigen buro); Roger (voor je MVC voetbal verhalen); Akko (ik bel je nog); Noud (voor de puntjes en de komma,s); Silvester (omdat je me niet ontslagen hebt tijdens de management cursus); Jeroen (mijn planning is in orde, ik mag alvast naar huis); Folbert (T_EX-hacker); Hans (zo simpel en toch onbegrepen); [1]; Marc (h7-h5 is toch niet zo goed); Harald (voor het beantwoorden van al mijn mail); Henk (voor het beschermen van mijn VAX account); André (zoveel gedaan, en toch geen Glenn Livet); Cor en Paul (krullebol!); Ogé, Simon en Waldo (en de goede administratie); Ellen (deze deadline ben ik niet vergeten); The Gang (wij hebben wel gestaan voor hetere vuren); Arthur (het is weer een Pia week); Peter (binnenkort spreken we ècht iets af); Christian (voor de tosti’s); Frits (voor de anti-vloer-piep campagne); Aad (voor het kopiëren kopiëren); André (taart!); Walter (voor de ondersteunende biertjes); José (voor de faxen om 8 uur ’s morgens); Arno (waar blijft die Japanner toch?); en tenslotte René (voor veel meer dan de kaft alleen).

[1]: HAJNAL (1990-1994) voor de vele artikelen en referenties.

Curriculum Vitae

Ik ben geboren op 7 oktober 1960 te Hilversum. Na het VWO examen (1980, Elshofcollege Nijmegen) ben ik natuurkunde gaan studeren (1980, Katholieke Universiteit Nijmegen). Ik ben afgestudeerd in de Experimentele Fysica (1986, vakgroep Molecuul- en Laserfysica). Het afstudeerwerk betrof moleculaire spectroscopie d.m.v. laser geïnduceerde fluorescentie aan benzeenachtige moleculen, en is verder verwerkt tot een publicatie (1986, Theoretische Chemie, KUN). Vervolgens ben ik in Maastricht gaan werken bij de vakgroep Biofysica (1987, Rijksuniversiteit Limburg) alwaar ik onderzoek verrichtte naar bewegingsdetectie in sequentiële videobeelden. Mijn promotieonderzoek heb ik verricht bij het FOM-instituut voor Plasmafysica "Rijnhuizen" (1990-1994) binnen de Transportfysica groep. De resultaten van dit onderzoek staan beschreven in dit proefschrift.